



Macrae, Roddy (2018) Polarisation observables in  $\pi^0$  photoproduction at MAMI. PhD thesis.

<https://theses.gla.ac.uk/9068/>

Copyright and moral rights for this work are retained by the author

A copy can be downloaded for personal non-commercial research or study, without prior permission or charge

This work cannot be reproduced or quoted extensively from without first obtaining permission in writing from the author

The content must not be changed in any way or sold commercially in any format or medium without the formal permission of the author

When referring to this work, full bibliographic details including the author, title, awarding institution and date of the thesis must be given

Enlighten: Theses

<https://theses.gla.ac.uk/>  
[research-enlighten@glasgow.ac.uk](mailto:research-enlighten@glasgow.ac.uk)

# Polarisation Observables in $\pi^0$ Photoproduction at MAMI

Roddy Macrae

A thesis presented for the degree of  
Doctor of Philosophy



Nuclear Physics Group  
School of Physics and Astronomy  
University of Glasgow

September 2017

# Polarisation Observables in $\pi^0$ Photoproduction at MAMI

Roddy Macrae

Submitted for the degree of Doctor of Philosophy  
September 2017

## Abstract

This thesis presents measurements of polarisation observables in neutral pion photoproduction conducted at the Mainzer Microtron (MAMI) in Mainz using the Crystal Ball detector. The double polarisation observable  $G$  and the polarisation observable  $\Sigma$  have been measured on a frozen spin butanol target in the  $\gamma p \rightarrow p\pi^0$  reaction between the  $\Delta(1232)$  and second resonance regions. The measurements have been made using a linearly polarised photon beam in the energy range  $370 < E_\gamma < 770$  MeV.

This work is part of a world wide program aimed at obtaining information on the nucleon excitation spectrum to better understand the internal dynamics and structure by measuring polarisation observables. Measurement of the  $G$  observable in the energy region of this work will help determine the  $M_{1-}$  partial wave. The  $M_{1-}$  partial wave is highly sensitive to the  $N(1440)\frac{1}{2}^+$  Roper resonance which is the first radial excitation of the proton. The properties of the Roper resonance are poorly understood and the mass, which is predicted to be higher than the negative parity resonance  $N(1535)\frac{1}{2}^-$ , cannot currently be reconciled by quark models based on  $SU(6)$  symmetry.

The  $s\mathcal{P}$ Plot technique was used to extract the polarisation observables in this work. The results are compared with the MAID, SAID and Bonn-Gatchina partial wave analysis curves.

These measurements will contribute to the world dataset of polarisation observables and provide information on the excitation spectrum of the nucleon towards an unambiguous, model independent, solution to partial wave analyses.

# Declaration

The work in this thesis is based on research carried out at the Nuclear Physics Group, School of Physics & Astronomy, University of Glasgow, UK. No part of this thesis has been submitted elsewhere for any other degree or qualification and it is all my own work unless referenced to the contrary in the text.

© Roddy Macrae 2017.

# Contents

<b>Abstract</b>	<b>ii</b>
<b>Declaration</b>	<b>iv</b>
<b>List of Figures</b>	<b>xi</b>
<b>List of Tables</b>	<b>xii</b>
<b>1 Introduction</b>	<b>1</b>
1.1 Motivation . . . . .	1
<b>2 Background</b>	<b>7</b>
2.1 Meson photoproduction . . . . .	7
2.2 Theory . . . . .	17
<b>3 Previous Work</b>	<b>19</b>
3.1 Previous measurements . . . . .	19
3.2 Partial Wave Analysis . . . . .	35
3.3 Other observables . . . . .	36
<b>4 Experiment</b>	<b>40</b>
4.1 MAMI . . . . .	41
4.2 Bremsstrahlung . . . . .	44
4.3 Coherent Bremsstrahlung . . . . .	46
4.4 Goniometer . . . . .	47
4.5 Collimator . . . . .	49

---

4.6	Glasgow Tagged Photon Spectrometer . . . . .	49
4.7	Detector Setup . . . . .	51
4.8	Trigger . . . . .	61
4.9	Simulation . . . . .	62
<b>5</b>	<b>Calibration</b>	<b>63</b>
5.1	Energy calibration . . . . .	63
5.2	Time calibration . . . . .	70
5.3	Linear Polarisation of the Photon Beam . . . . .	77
<b>6</b>	<b>Signal Selection</b>	<b>81</b>
6.1	Software . . . . .	81
6.2	Event Selection . . . . .	82
6.3	Background subtraction . . . . .	85
6.4	<i>sPlot</i> method . . . . .	86
<b>7</b>	<b>Observable Extraction</b>	<b>94</b>
7.1	Asymmetries . . . . .	94
<b>8</b>	<b>Results</b>	<b>106</b>
8.1	$\Sigma$ Results . . . . .	106
8.2	$\Sigma$ Results Discussion . . . . .	110
8.3	G Results . . . . .	112
8.4	Correction Factor . . . . .	117
8.5	Systematic Uncertainty . . . . .	121
8.6	G Results Discussion . . . . .	134
8.7	Conclusions . . . . .	135
<b>A</b>	<b>Tabulated Results</b>	<b>138</b>
A.1	$\Sigma$ Results . . . . .	138
A.2	Tabulated G Results . . . . .	143

# List of Figures

1.1	Left: Baryon octet. Right: Baryon decuplet. . . . .	3
1.2	Left: pseudoscalar meson nonet. Right: vector meson nonet . . . . .	3
1.3	$N^*$ and $\Delta$ resonance ratings and predicted values . . . . .	5
1.4	The mass position of resonance states as predicted by quark model . . . . .	6
2.1	Wave representation of a photoproduction experiment. . . . .	8
2.2	Cross section of photoproduction off of the proton. . . . .	9
2.3	A general overview of a two body reaction. . . . .	10
2.4	The different interactions between two initial state particles $k$ and $p_i$ . . . . .	11
2.5	The Feynman diagrams of first order Born terms in single meson photoproduction . . . . .	13
2.6	Four different helicity spin flip interactions in $\pi^0$ photoproduction . . . . .	13
2.7	Reaction frame of the single $\pi^0$ photoproduction experiment . . . . .	18
3.1	Schematic of the LEGS detector. Taken from [58]. . . . .	20
3.2	Schematic of the Yerevan set-up. . . . .	21
3.3	Yerevan $\Sigma$ results from the $\gamma p \rightarrow \pi^0 p$ reaction. . . . .	22
3.4	Schematic of the GRAAL set-up. Taken from [60]. . . . .	24
3.5	GRAAL angular results of beam asymmetry $\Sigma$ from the reaction $\gamma p$ $\rightarrow \pi^0 p$ . . . . .	25
3.6	Schematic of the CBELSA detector. Taken from [33]. . . . .	26
3.7	The central DAPHNE detector. Taken from [64]. . . . .	27
3.8	Previous configuration where the TAPS configuration differs from cur- rent set up . . . . .	28
3.9	TAPS/DAPHNE $\Sigma$ results from the $\gamma p \rightarrow \pi^0 p$ reaction . . . . .	29

3.10	Beam asymmetry $\Sigma$ dependence on $\cos\theta_{CM}$ from Gardner et al. [70]	31
3.11	First results of the beam-target polarisation observable G at Daresbury	32
3.12	Beam-target polarisation observable G measured with DAPHNE . . .	33
3.13	Double polarisation observable G in $\pi^0$ photoproduction with CBELSA.	34
3.14	T and F observables in the $\gamma p \rightarrow \pi^0 p$ reaction . . . . .	37
3.15	MAMI detector set up with additional graphite polarimeter . . . . .	38
3.16	The beam-recoil polarisation observable $C_x$ in the reaction $\gamma p \rightarrow \pi^0 p$	39
4.1	Overview of the entire MAMI facility. . . . .	41
4.2	Schematic of a race-track microtron. . . . .	42
4.3	Schematic of a harmonic double-sided microtron. . . . .	43
4.4	Bremsstrahlung distributions from different radiators and enhance- ment spectrum . . . . .	45
4.5	View of the Goniometer through the camera mounted inside it. The centre slot is the diamond radiator. . . . .	47
4.6	Radial distributions of goniometer scans in Stonehenge technique. . .	48
4.7	Schematic of the Photon Tagger. Taken from [89]. . . . .	50
4.8	Overview of the TAPS-CB set up [90]. . . . .	51
4.9	Schematic of the Crystal Ball showing target position. . . . .	53
4.10	Schematic of one of the 672 NaI crystals which form the crystal ball [90]. . . . .	54
4.11	PID detector with 24 plastic scintillators in a cylindrical configuration.	55
4.12	TAPS schematic as seen from the target. . . . .	56
4.13	Solenoid coil used for longitudinal polarisation of the butanol target. .	57
4.14	Typical target temperature stability over a single day. . . . .	58
4.15	$^3\text{He}/^4\text{He}$ dilution refrigerator schematic. . . . .	60
5.1	Energy spectrum from one NaI(Tl) crystal using an $^{241}\text{Am}^9\text{Be}$ source.	65
5.2	Two photon invariant mass for the CB showing the peak of the $\pi^0$ . .	67
5.3	PID energy calibration. . . . .	68
5.4	TAPS low energy calibration. . . . .	69
5.5	TAPS high energy calibration. . . . .	70

5.6	Tagger timing calibration. . . . .	72
5.7	Crystal Ball timing calibration. . . . .	73
5.8	Crystal ball time walk fit. . . . .	74
5.9	PID timing calibration. . . . .	75
5.10	PID angle calibration. . . . .	76
5.11	TAPS time calibration. . . . .	77
5.12	Enhancement plot with phenomenological fit (red) applied to enhancement data (black) . . . . .	78
5.13	Enhancement plot with phenomenological fit showing free parameters. . . . .	79
5.14	The degree of linear polarisation calculated from the phenomenological fit . . . . .	80
6.1	Missing mass distribution after $\pi^0$ candidate selection. Proton peak can be seen at 940 MeV on top of a large background. . . . .	84
6.2	Maximum likelihood fit to tagged timing spectrum . . . . .	88
6.3	Fit to the missing mass spectrum showing a peak around the proton mass. . . . .	90
6.4	Fit to opening angle between detected and reconstructed proton. . . . .	91
6.5	Fit to coplanarity between $\pi^0$ and detected proton. . . . .	92
6.6	Nuclear background subtracted distributions leaving signal events. . . . .	93
7.1	Toy detector acceptance applied to generated $\phi$ distributions. . . . .	97
7.2	Generated $\phi$ distributions with detector acceptances applied. Counts are shown on the y-axis with angle along the x-axis. . . . .	98
7.3	Fits to asymmetries using Equation 7.6 for positive and negative target polarisation settings separately. Top: Asymmetry of parallel and perpendicular $\phi$ distributions with a positive target polarisation. Bottom: Asymmetry of parallel and perpendicular $\phi$ distributions with a negative target polarisation. The y-axis shows the magnitude of the asymmetries. . . . .	99
7.4	Changes of extracted polarisation observable magnitudes by varying parameter $C_2$ . . . . .	100

7.5	Changes of extracted polarisation observable magnitudes by varying parameter $C_3$ . . . . .	101
7.6	Difference between extracted observables and input values used to generate toy azimuthal distributions. . . . .	103
7.7	Example fits to data asymmetries to extract $\Sigma$ and $G$ . . . . .	105
8.1	Positive target photon asymmetry $\Sigma$ results as a function of $\cos\theta$ . . .	107
8.2	Negative target photon asymmetry $\Sigma$ results as a function of $\cos\theta$ . . .	108
8.3	Averaged target photon asymmetry $\Sigma$ results for positive and negative target polarisations as a function of $\cos\theta$ . . . . .	109
8.4	Photon asymmetry $\Sigma$ results as a function of $\cos\theta$ . . . . .	110
8.5	Beam-target observable $G$ results as a function of $\cos\theta$ with positive target. . . . .	113
8.6	Beam-target observable $G$ results as a function of $\cos\theta$ with negative target. . . . .	114
8.7	Beam-target observable $G$ results as a function of $\cos\theta$ for averaged positive and negative target settings. . . . .	115
8.8	Beam-target observable $G$ results as a function of $\cos\theta$ . . . . .	116
8.9	Correction factor as a function of energy. . . . .	117
8.10	Beam-target observable $\Sigma$ results as a function of $\cos\theta$ . . . . .	119
8.11	Beam-target observable $G$ results as a function of $\cos\theta$ . . . . .	120
8.12	Degree of linear polarisation systematic from normalisation baseline variation. . . . .	122
8.13	Degree of linear polarisation systematic from normalisation baseline variation. . . . .	124
8.14	Examples of phenomenological fits to enhancement data. . . . .	126
8.15	Systematic checks of linear polarisation degree performed by collaborators at Bonn. . . . .	127
8.16	$\Sigma$ pull distributions for two different target states. . . . .	129
8.17	$G$ pull distributions for two different target states. . . . .	130
8.18	$s\mathcal{P}$ lot opening angle subtraction method $\Sigma$ pull distribution. . . . .	131
8.19	$s\mathcal{P}$ lot coplanarity subtraction method $\Sigma$ pull distribution. . . . .	131

---

8.20 $s\mathcal{P}$ lot missing mass subtraction method $\Sigma$ pull distribution. . . . .	132
8.21 $s\mathcal{P}$ lot opening angle subtraction method G pull distribution. . . . .	132
8.22 $s\mathcal{P}$ lot coplanarity subtraction method G pull distribution. . . . .	133
8.23 $s\mathcal{P}$ lot missing mass subtraction method G pull distribution. . . . .	133

# List of Tables

1.1	Table outlining the properties of quarks including charge, baryon number, isospin, isospin projection and strangeness quantum numbers. . . . .	4
2.1	Single and double polarisation observables associated with pion photoproduction. . . . .	16
4.1	Table listing energies of electrons at each stage of the MAMI accelerator.	43
6.1	Table outlining the 4-vector components of each particle used in reconstructing the missing proton 4-vector. . . . .	84
6.2	Cuts applied based on expected reaction kinematics to aid event selection. . . . .	85
7.1	Table outlining the different combinations of incident photon beam and target polarisation settings. . . . .	96
8.1	Mean and sigma values of the $s\mathcal{P}$ lot pull distributions for $\Sigma$ measurements. . . . .	133
8.2	Mean and sigma values of the $s\mathcal{P}$ lot pull distributions for G measurements. . . . .	134

# Chapter 1

## Introduction

Measurements of the photon beam asymmetry  $\Sigma$  and beam-target polarisation observable  $G$  have been made with a polarised butanol target for the reaction channel  $\gamma p \rightarrow \pi^0 p$  and the Crystal Ball calorimeter at the Mainzer Microtron (MAMI) in Mainz. Precise measurement of the  $G$  observable will provide information on the  $M_{1-}$  partial wave and contribute to the effort towards an unambiguous, model independent solution to transversity amplitudes in pion photoproduction. It will aid in measuring the poorly understood properties of the Roper resonance which has particular sensitivity to the  $M_{1-}$  partial wave. This work is part of a world wide effort to better understand the nature of the nucleon by analysing data on its excitation spectrum.

### 1.1 Motivation

The properties of the atom can be described by the electromagnetic and strong forces. Quantum Electrodynamics provides an accurate quantitative picture of electromagnetism that has been validated by many experiments. However the situation with the strong force, which is responsible for binding the atomic nuclei as well as the protons and neutrons contained therein, is more complicated. New experimental data is required to aid the understanding of the strong force by constraining the

relevant degrees of freedom responsible for phenomena at nucleon mass scales.

Rutherford performed scattering experiments using alpha particles off a gold foil, which led him to postulate the existence of the atomic nucleus [1]. The neutron was discovered later by Chadwick in 1932 [2]. Protons and neutrons were originally treated as two states of the same particle by Heisenberg, with a small difference in their respective masses. He introduced the quantum number isospin ( $I$ ) in order to distinguish the two particles in the quantum mechanical framework. The third component of the isospin vector ( $I_3$ ) distinguished the proton ( $I_3 = \frac{1}{2}$ ) and neutron ( $I_3 = -\frac{1}{2}$ ) [3].

Isospin is one of several quantum numbers used to help distinguish characteristics describing hadrons. As scattering experiments improved, many more particles were discovered over the next few decades. The number of quantum numbers used to describe their properties grew, and a classification system was developed. Strangeness ( $S$ ) is the quantum number prescribed for particles with strangely long lifetimes [4, 5], baryon number ( $B$ ) separates baryons ( $B=1$ ) and mesons ( $B=0$ ). Hypercharge ( $Y$ ) was introduced in order to relate the electric charge ( $Q$ ) with isospin, baryon number and strangeness where  $Y = B + S$ .

$$Q = I_3 + \frac{1}{2}(Y) \quad (1.1)$$

With the additional degree of freedom allowed by the strangeness ( $S$ ) quantum number Gell-Mann and Ne'eman independently developed the classification system now known as the Eight-fold way [6, 7] illustrated in Figures 1.1 and 1.2. The baryons are arranged into a spin- $\frac{1}{2}$  and spin- $\frac{3}{2}$  octet and decuplet, while the mesons are arranged into a pseudoscalar ( $J^P = 0^-$ ) and vector meson ( $J^P = 1^-$ ) nonet.

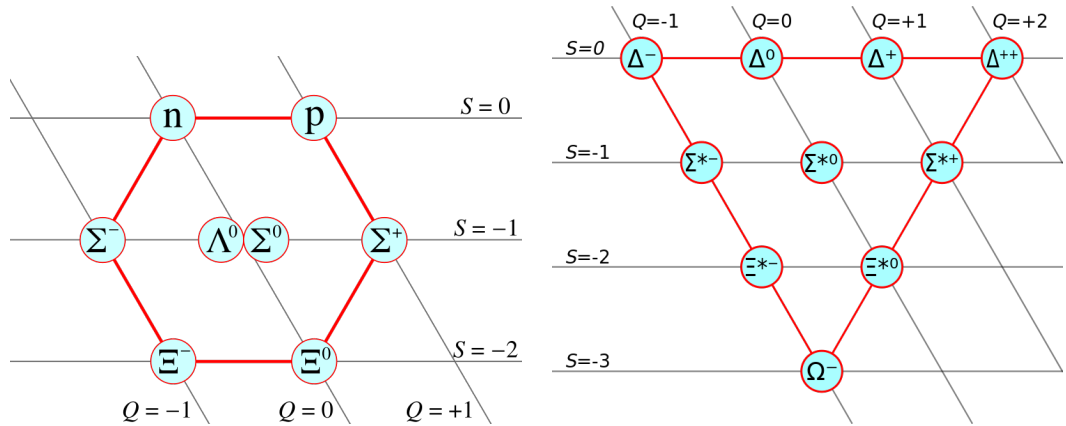


Figure 1.1: Left: Baryon octet. Right: Baryon decuplet.

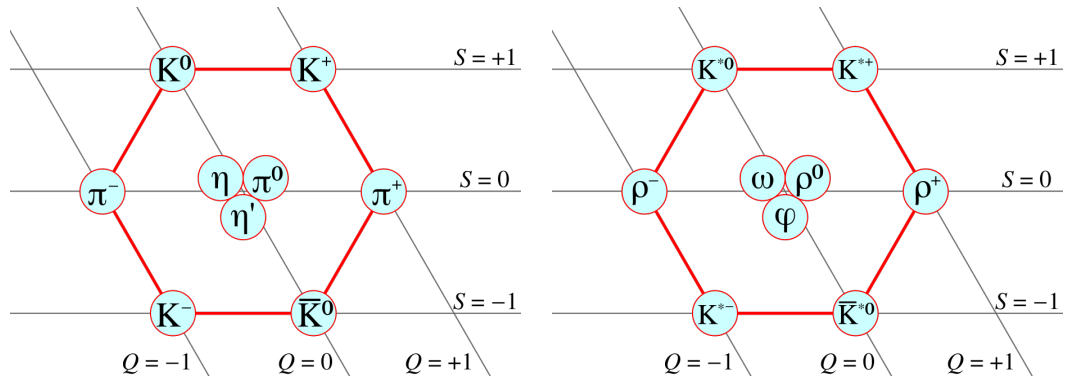


Figure 1.2: Left: pseudoscalar meson nonet. Right: vector meson nonet

The Eight-fold way description is based on the  $SU(3)$  flavour group implying that the baryons and mesons identified as part of it are not fundamental themselves [8]. Gell-Mann and Zweig postulated the existence of quarks from this interpretation independently of each other [6, 9]. Baryons are described as 3-quark bound states while mesons are 2-quark bound states (one quark and one anti-quark, or  $q\bar{q}$ ). The quarks were initially believed to come in three flavours now known as up (u), down (d) and strange (s) quarks (Table 1.1). The proton is a uud bound system while the neutron is a ddu system. The composition of quarks required to produce certain baryons at the time, such as the  $\Delta^{++}$ , violated the Fermi exclusion principle which states fermions, such as quarks, with identical quantum numbers could not occupy the same state. Greenberg proposed a solution to this problem by introducing a new quantum number now referred to as colour [10]. Colour charge comes in three states, red, green and blue. All hadrons are colour neutral, meaning there are anti-

colour and colour combinations in each hadron which result in a net zero colour charge.

Flavour	Q	I	$I_3$	B	S
u	$+\frac{2}{3}$	$\frac{1}{2}$	$+\frac{1}{2}$	$\frac{1}{3}$	0
d	$-\frac{1}{3}$	$\frac{1}{2}$	$-\frac{1}{2}$	$\frac{1}{3}$	0
s	$-\frac{1}{3}$	0	0	$\frac{1}{3}$	-1

Table 1.1: Table outlining the properties of quarks including charge, baryon number, isospin, isospin projection and strangeness quantum numbers.

Hadrons may be excited into higher energy states. Several models attempted to describe the excited behaviour of nucleons and predicted properties of these resonant states. The symmetric quark model gives equal degrees of freedom to all three valence quarks [11, 12]. The di-quark model is similar but models two quarks bound tightly together leaving the third free to oscillate. The bound quarks in this model reduces the total number of degrees of freedom allowed in the system [13, 14].

These models are in good agreement with experimental measurements at low invariant mass values. Both types of model describe many of the resonances but neither predict the full spectrum of masses and widths of excited states accurately [15, 16]. Many predicted resonances are not seen experimentally and are known as the “missing resonances” [17] (Figure 1.4).

Initial studies of excited states used pion beams in order to excite protons and study the properties of their resonant states. Pion beams may couple weakly to certain resonances leaving some states undiscovered. Photon beam experiments were proposed to overcome this as the couplings can be different. Development of continuous-wave electron beams allows the production of high intensity, high energy photon beams. These produce high statistics data sets to search for missing resonances and accurately determine the properties of known states.

$p$	1/2 <sup>+</sup> ****	$\Delta(1232)$	3/2 <sup>+</sup> ****	$\Sigma^+$	1/2 <sup>+</sup> ****	$\Xi^0$	1/2 <sup>+</sup> ****	$\Lambda_c^+$	1/2 <sup>+</sup> ****
$n$	1/2 <sup>+</sup> ****	$\Delta(1600)$	3/2 <sup>+</sup> ***	$\Sigma^0$	1/2 <sup>+</sup> ****	$\Xi^-$	1/2 <sup>+</sup> ****	$\Lambda_c(2595)^+$	1/2 <sup>-</sup> ***
$N(1440)$	1/2 <sup>+</sup> ****	$\Delta(1620)$	1/2 <sup>-</sup> ****	$\Sigma^-$	1/2 <sup>+</sup> ****	$\Xi(1530)$	3/2 <sup>+</sup> ****	$\Lambda_c(2625)^+$	3/2 <sup>-</sup> ***
$N(1520)$	3/2 <sup>-</sup> ****	$\Delta(1700)$	3/2 <sup>-</sup> ****	$\Sigma(1385)$	3/2 <sup>+</sup> ****	$\Xi(1620)$	*	$\Lambda_c(2765)^+$	*
$N(1535)$	1/2 <sup>-</sup> ****	$\Delta(1750)$	1/2 <sup>+</sup> *	$\Sigma(1480)$	*	$\Xi(1690)$	***	$\Lambda_c(2880)^+$	5/2 <sup>+</sup> ***
$N(1650)$	1/2 <sup>-</sup> ****	$\Delta(1900)$	1/2 <sup>-</sup> **	$\Sigma(1560)$	**	$\Xi(1820)$	3/2 <sup>-</sup> ***	$\Lambda_c(2940)^+$	***
$N(1675)$	5/2 <sup>-</sup> ****	$\Delta(1905)$	5/2 <sup>+</sup> ****	$\Sigma(1580)$	3/2 <sup>-</sup> *	$\Xi(1950)$	***	$\Sigma_c(2455)$	1/2 <sup>+</sup> ****
$N(1680)$	5/2 <sup>+</sup> ****	$\Delta(1910)$	1/2 <sup>+</sup> ****	$\Sigma(1620)$	1/2 <sup>-</sup> *	$\Xi(2030)$	$\geq \frac{5}{2}^?$ ***	$\Sigma_c(2520)$	3/2 <sup>+</sup> ***
$N(1700)$	3/2 <sup>-</sup> ***	$\Delta(1920)$	3/2 <sup>+</sup> ***	$\Sigma(1660)$	1/2 <sup>+</sup> ***	$\Xi(2120)$	*	$\Sigma_c(2800)$	***
$N(1710)$	1/2 <sup>+</sup> ****	$\Delta(1930)$	5/2 <sup>-</sup> ***	$\Sigma(1670)$	3/2 <sup>-</sup> ****	$\Xi(2250)$	**	$\Xi_c^+$	1/2 <sup>+</sup> ***
$N(1720)$	3/2 <sup>+</sup> ****	$\Delta(1940)$	3/2 <sup>-</sup> **	$\Sigma(1690)$	**	$\Xi(2370)$	**	$\Xi_c^0$	1/2 <sup>+</sup> ***
$N(1860)$	5/2 <sup>+</sup> **	$\Delta(1950)$	7/2 <sup>+</sup> ****	$\Sigma(1730)$	3/2 <sup>+</sup> *	$\Xi(2500)$	*	$\Xi_c^{'+}$	1/2 <sup>+</sup> ***
$N(1875)$	3/2 <sup>-</sup> ***	$\Delta(2000)$	5/2 <sup>+</sup> **	$\Sigma(1750)$	1/2 <sup>-</sup> ***			$\Xi_c^{'+0}$	1/2 <sup>+</sup> ***
$N(1880)$	1/2 <sup>+</sup> **	$\Delta(2150)$	1/2 <sup>-</sup> *	$\Sigma(1770)$	1/2 <sup>+</sup> *	$\Omega^-$	3/2 <sup>+</sup> ****	$\Xi_c^0$	1/2 <sup>+</sup> ***
$N(1895)$	1/2 <sup>-</sup> **	$\Delta(2200)$	7/2 <sup>-</sup> *	$\Sigma(1775)$	5/2 <sup>-</sup> ****	$\Omega(2250)^-$	***	$\Xi_c(2645)$	3/2 <sup>+</sup> ***
$N(1900)$	3/2 <sup>+</sup> ***	$\Delta(2300)$	9/2 <sup>+</sup> **	$\Sigma(1840)$	3/2 <sup>+</sup> *	$\Omega(2380)^-$	**	$\Xi_c(2790)$	1/2 <sup>-</sup> ***
$N(1990)$	7/2 <sup>+</sup> **	$\Delta(2350)$	5/2 <sup>-</sup> *	$\Sigma(1880)$	1/2 <sup>+</sup> **	$\Omega(2470)^-$	**	$\Xi_c(2815)$	3/2 <sup>-</sup> ***
$N(2000)$	5/2 <sup>+</sup> **	$\Delta(2390)$	7/2 <sup>+</sup> *	$\Sigma(1900)$	1/2 <sup>-</sup> *			$\Xi_c(2930)$	*
$N(2040)$	3/2 <sup>+</sup> *	$\Delta(2400)$	9/2 <sup>-</sup> **	$\Sigma(1915)$	5/2 <sup>+</sup> ****			$\Xi_c(2970)$	***
$N(2060)$	5/2 <sup>-</sup> **	$\Delta(2420)$	11/2 <sup>+</sup> ****	$\Sigma(1940)$	3/2 <sup>+</sup> *			$\Xi_c(3055)$	***
$N(2100)$	1/2 <sup>+</sup> *	$\Delta(2750)$	13/2 <sup>-</sup> **	$\Sigma(1940)$	3/2 <sup>-</sup> ***			$\Xi_c(3080)$	***
$N(2120)$	3/2 <sup>-</sup> **	$\Delta(2950)$	15/2 <sup>+</sup> **	$\Sigma(2000)$	1/2 <sup>-</sup> *			$\Xi_c(3123)$	*
$N(2190)$	7/2 <sup>-</sup> ****			$\Sigma(2030)$	7/2 <sup>+</sup> ****			$\Omega_c^0$	1/2 <sup>+</sup> ***
$N(2220)$	9/2 <sup>+</sup> ****	$\Lambda$	1/2 <sup>+</sup> ****	$\Sigma(2070)$	5/2 <sup>+</sup> *			$\Omega_c(2770)^0$	3/2 <sup>+</sup> ***
$N(2250)$	9/2 <sup>-</sup> ****	$\Lambda(1405)$	1/2 <sup>-</sup> ****	$\Sigma(2080)$	3/2 <sup>+</sup> **			$\Xi_{cc}^+$	*
$N(2300)$	1/2 <sup>+</sup> **	$\Lambda(1520)$	3/2 <sup>-</sup> ****	$\Sigma(2100)$	7/2 <sup>-</sup> *				
$N(2570)$	5/2 <sup>-</sup> **	$\Lambda(1600)$	1/2 <sup>+</sup> ***	$\Sigma(2250)$	***			$\Lambda_b^0$	1/2 <sup>+</sup> ***
$N(2600)$	11/2 <sup>-</sup> ***	$\Lambda(1670)$	1/2 <sup>-</sup> ****	$\Sigma(2455)$	**			$\Lambda_b(5912)^0$	1/2 <sup>-</sup> ***
$N(2700)$	13/2 <sup>+</sup> **	$\Lambda(1690)$	3/2 <sup>-</sup> ****	$\Sigma(2620)$	**			$\Lambda_b(5920)^0$	3/2 <sup>-</sup> ***
		$\Lambda(1710)$	1/2 <sup>+</sup> *	$\Sigma(3000)$	*			$\Sigma_b$	1/2 <sup>+</sup> ***
		$\Lambda(1800)$	1/2 <sup>-</sup> ***	$\Sigma(3170)$	*			$\Sigma_b^+$	3/2 <sup>+</sup> ***
		$\Lambda(1810)$	1/2 <sup>+</sup> ***					$\Xi_b^0, \Xi_b^-$	1/2 <sup>+</sup> ***
		$\Lambda(1820)$	5/2 <sup>+</sup> ****					$\Xi_b^+(5935)^-$	1/2 <sup>+</sup> ***
		$\Lambda(1830)$	5/2 <sup>-</sup> ****					$\Xi_b(5945)^0$	3/2 <sup>+</sup> ***
		$\Lambda(1890)$	3/2 <sup>+</sup> ****					$\Xi_b^+(5955)^-$	3/2 <sup>+</sup> ***
		$\Lambda(2000)$	*					$\Omega_b^-$	1/2 <sup>+</sup> ***
		$\Lambda(2020)$	7/2 <sup>+</sup> *						
		$\Lambda(2050)$	3/2 <sup>-</sup> *					$P_c(4380)^+$	*
		$\Lambda(2100)$	7/2 <sup>-</sup> ****					$P_c(4450)^+$	*
		$\Lambda(2110)$	5/2 <sup>+</sup> ***						
		$\Lambda(2325)$	3/2 <sup>-</sup> *						
		$\Lambda(2350)$	9/2 <sup>+</sup> ***						
		$\Lambda(2585)$	**						

Figure 1.3:  $N^*$  and  $\Delta$  resonance ratings and predicted values from various partial wave models. Taken from [17]. Resonances that are certain are given a 4 star rating. 3 stars denotes resonances with some less well defined properties but which are almost certain. 2 stars show a resonance with fair probability of existence and 1 star is a resonance with poor experimental evidence for existence.

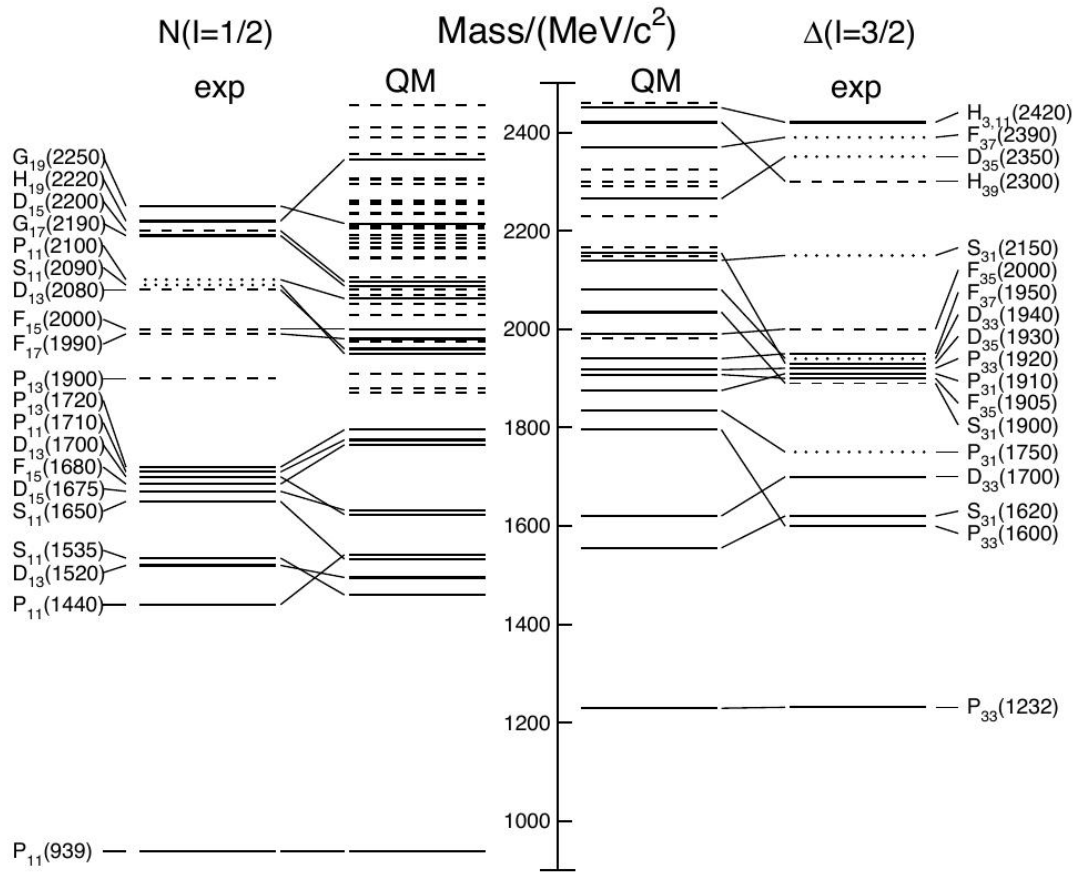


Figure 1.4: The mass position of resonance states as predicted by quark model are compared with experimental measurements, taken from [18]. Left shows the  $I = \frac{1}{2}N^*$  states, right shows the  $I = \frac{3}{2}\Delta$  states. Experimental data (under 'exp' column) shows three and four star states as solid lines, two star states as dashed lines and one star states as dotted lines. The QM column shows predicted states which have been observed in experiment, dashed lines are predicted states with no experimental observation.

# Chapter 2

## Background

### 2.1 Meson photoproduction

Modern meson photoproduction experiments are primarily performed using high energy real photon beams. Real photons offer a way to study the electric and magnetic couplings of resonant states. Previous work used pion scattering experiments to probe the resonant states of the nucleon [19, 20, 21, 22], primarily forming the states in the Particle Data Group review [17]. Experiments using real photons provide data which can offer insight into the resonant states of nucleons which may otherwise be inaccessible or weakly coupled to previous pion scattering measurements.

This chapter explores the properties of scattering experiments off the nucleon using real photons. The focus is on the polarisation observables that are accessible using a polarised photon beam and proton target.

#### 2.1.1 Particle Scattering Reactions

The scattering process in meson photoproduction experiments can be viewed in terms of scattering waves [23, 24]. The photon beam in this case is treated as a plane wave which scatters off target. The information of the scattered wave, target and initial plane wave can shed light on the intermediate state of the target.

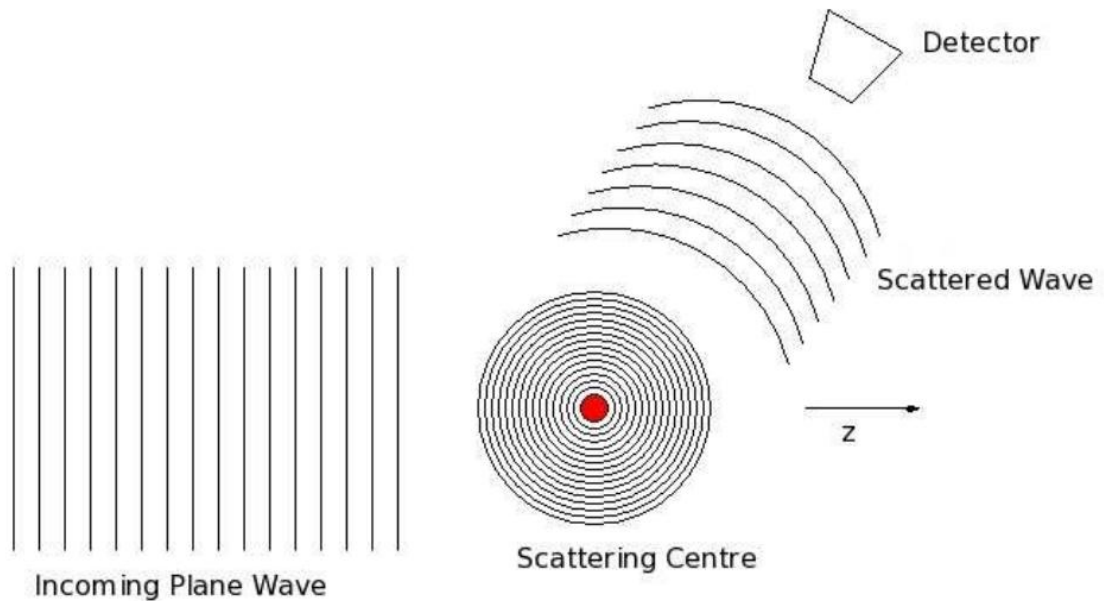


Figure 2.1: Wave representation of a photoproduction experiment. A plane wave scatters off of a target and produces a scattered wave. These scattered waves propagate from the target and are incident on a detector surrounding the target, offering kinematic information on the reaction products.

The reaction on the target is not a simple one and the scattered wave is influenced by many contributing reaction processes. There is a requirement to decompose these scattered waves further into their separate components in order to disentangle the contributions of different reaction mechanisms to the overall waves. This is done through partial wave analysis techniques.

### 2.1.2 Reaction channels

There are many different reaction channels contributing to photoproduction off the nucleon. The probability of a given final state occurring is characterised by the cross section  $\sigma$  of that final state which contributes to the overall cross section  $\sigma_{total}$ . Figure 2.2 shows the total cross section for photoproduction off the proton which has been extensively studied [25, 26, 27]. There is a significant amount of information contained already within the total cross section of a nucleon. Resonances often represent themselves as peaks in the cross section distribution, however many states are broad and overlap, making definitive statements about the presence of particular

states unreliable.

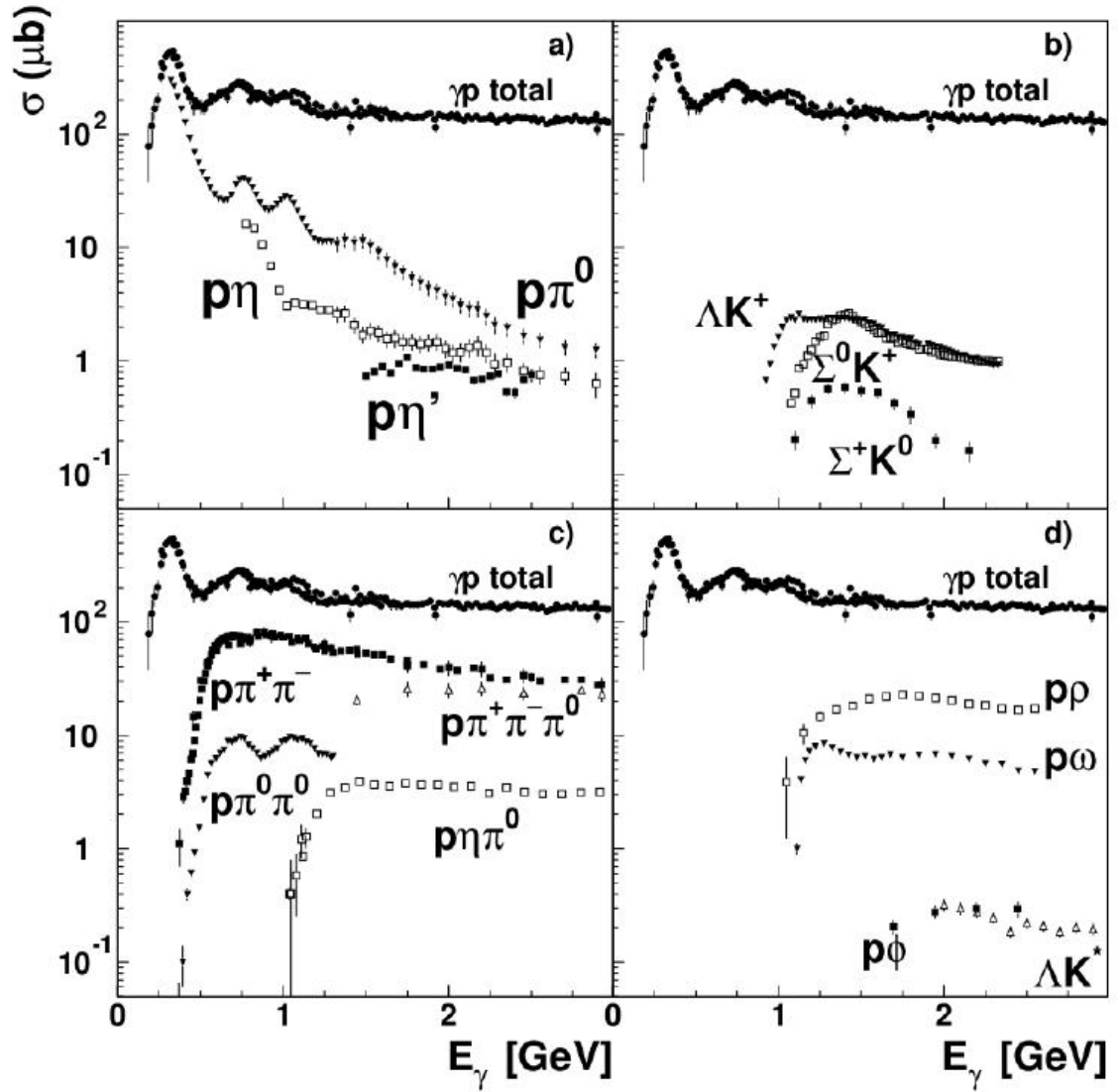


Figure 2.2: Cross section of photoproduction off of the proton. a) pseudoscalar final states [28, 29], b) cross section from strange final states [30, 31, 32], c) multiple meson final states [33, 34, 35, 36, 37], d) vector meson [38, 39, 40]. Distributions show broad overlapping contributions from many different final states resulting in a complicated interpretation.

It is apparent that the cross section alone is insufficient at locating and investigating resonances and their properties. At increasing energies more final state channels pass their threshold production energy and contribute to the overall cross section. Investigation of resonances can be achieved by studying different final states, which couple strongly to that particular resonance, separately.

### 2.1.3 Reaction kinematics

The kinematics of a photon-nucleon interaction are defined for the initial and final states of the reaction particles. Figure 2.3 shows a general interaction of a two body reaction between a photon and a nucleon.

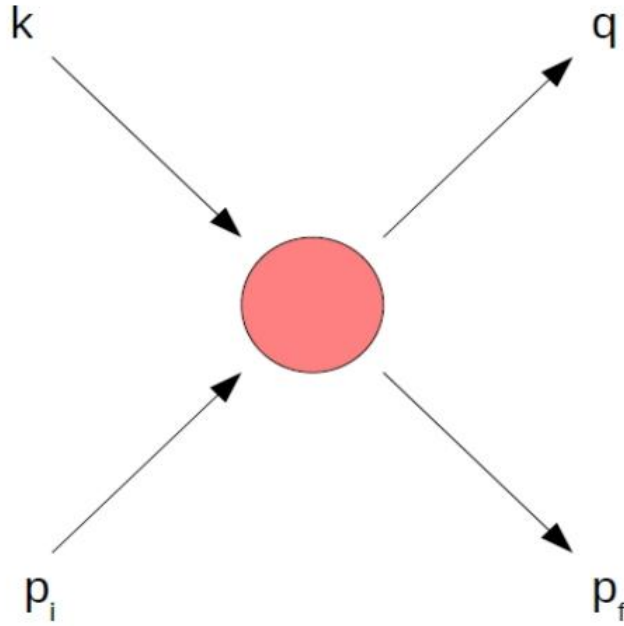


Figure 2.3: A general overview of a two body reaction. Two initial particles,  $k$  and  $p_i$ , interact (red circle) in some manner and produce the final state particles  $q$  and  $p_f$ . Taken from [41].

The four momenta of the incident photon, initial nucleon, recoiling meson and recoiling nucleon are  $k$ ,  $p_i$ ,  $q$ ,  $p_f$ , with energies  $E_k$ ,  $E_i$ ,  $E_q$ ,  $E_f$  respectively. Through the conservation of momentum it is clear that

$$k + p_i = q + p_f \quad (2.1)$$

where the 4-vectors  $k$ ,  $q$  and  $P = \frac{1}{2}(p_i + p_f)$  are independent.

Different reaction mechanisms can be represented as three basic Feynman diagrams. These representations are known as s-channel, t-channel and u-channel and represent interactions between the initial state particles where an intermediate particle is exchanged.

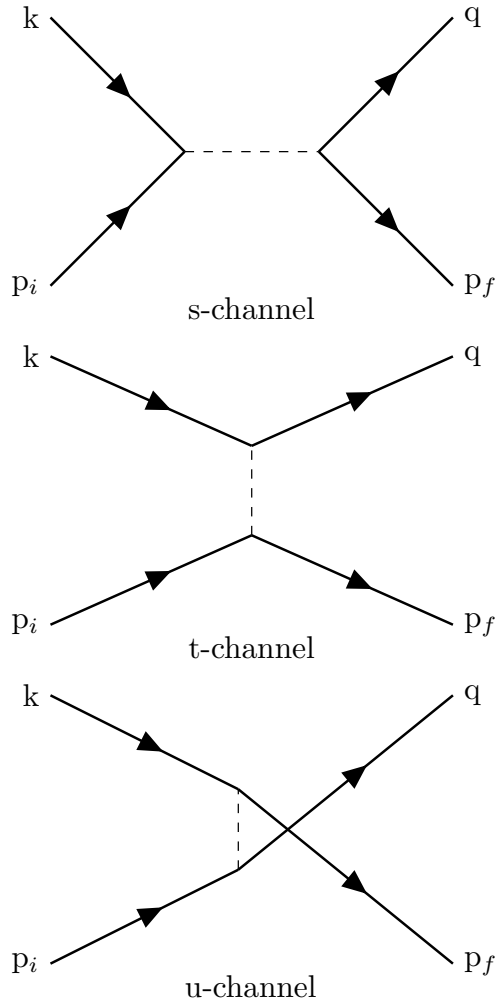


Figure 2.4: The different interactions between two initial state particles  $k$  and  $p_i$  where an intermediate particle is exchanged, resulting in the two final state particles  $q$  and  $p_f$ . The u-channel is the same as the t-channel with the roles of  $q$  and  $p_f$  interchanged.

We can write the kinematic relationships between the particles and channels as

$$\begin{aligned}
 s &= (k + p_i)^2 \\
 t &= (p_i - p_f)^2 \\
 u &= (p_i - q)^2
 \end{aligned}
 \tag{2.2}$$

where  $s$  is the centre of mass energy ( $W^2$ ) and  $t$  is the momentum transfer of the reaction. The set of Lorentz vectors  $s$ ,  $t$  and  $u$  relate to the sum of the masses of all

the reaction particles

$$s + t + u = \sum_{i=1}^4 m_i^2 \quad (2.3)$$

#### 2.1.4 Decay terms

The final states of photoproduction reactions can be produced by many distinct mechanisms deriving from the three diagrams in Figure 2.4. In order to study the resonance associated with an intermediate state the reaction must be separated into background and resonance terms. In the case of meson photoproduction it is s-channel resonance production which is regarded as the signal, with the other diagrams constituting “background” [42, 43].

Figure 2.5 shows the Feynman diagrams contributing to single meson final states off a free nucleon. The Born terms constitute diagrams where only the photon, pion and nucleon are involved. In the case of  $\pi^0$  meson photoproduction the bottom left term of Figure 2.5 does not contribute as the photon does not couple directly to the neutral pion.

Observable quantities in  $\pi^0$  photoproduction are related to the superposition of the different Born and resonance terms. The background Born terms have energy dependencies which are smooth and predictable [44]. Additional structure seen in observables can be characterised by resonance contributions.

The resonance contribution needs to be characterised in a meaningful way in order to better understand and relate observable quantities to it. The next section discusses how this is achieved.

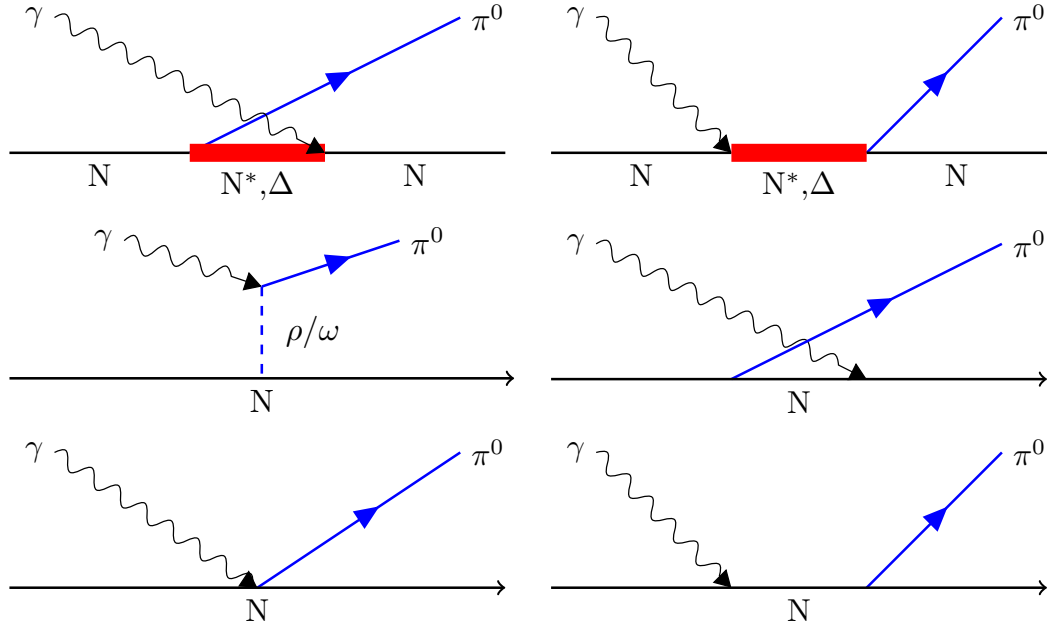


Figure 2.5: The Feynman diagrams of first order Born terms in single meson photoproduction off a free nucleon. Top left: U channel resonance, Top right: S channel resonance, Middle left: Born T vector exchange channel, Middle right: Born U channel, Bottom left: Born contact term, Bottom right: Born S channel.

### 2.1.5 Photoproduction Amplitudes

The electric and magnetic components of the photon couple to the nucleon which can have parallel or anti-parallel spin alignment. The couplings can be described as multipoles in relation to s-channel helicity spin transitions in a reaction, shown in Figure 2.6.

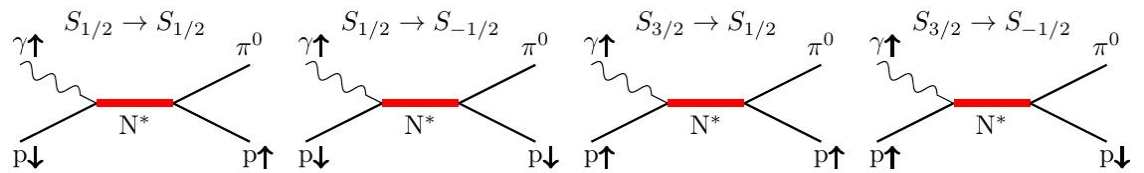


Figure 2.6: Four different helicity spin flip interactions in  $\pi^0$  photoproduction. From left to right the states are: Far left: N = no spin flip. Centre left:  $S_A$  = anti-parallel spin flip. Centre right:  $S_P$  = parallel spin flip. Far right: D = double spin flip.

In  $\pi^0$  photoproduction off the proton there are four helicity amplitudes which can

be expanded as linear combinations of photoproduction multipoles [45, 46] as

$$\begin{aligned}
N &= \frac{1}{\sqrt{2}} \cos\left(\frac{\theta}{2}\right) \sum_{\ell=0}^{\infty} [(\ell+2)E_{\ell+} + \ell M_{\ell+} + E_{(\ell+1)-} - (\ell+2)M_{(\ell+1)-}] (P'_{\ell} - P'_{\ell+1}) \\
S_A &= \frac{1}{\sqrt{2}} \sin\left(\frac{\theta}{2}\right) \sum_{\ell=0}^{\infty} [(\ell+2)E_{\ell+} + \ell M_{\ell+} - E_{(\ell+1)-} + (\ell+2)M_{(\ell+1)-}] (P'_{\ell} + P'_{\ell+1}) \\
S_P &= \frac{1}{\sqrt{2}} \cos\left(\frac{\theta}{2}\right) \sin\theta \sum_{\ell=1}^{\infty} [E_{\ell+} - M_{\ell+} - E_{(\ell+1)-} - M_{(\ell+1)-}] (P''_{\ell} - P''_{\ell+1}) \\
D &= \frac{1}{\sqrt{2}} \sin\left(\frac{\theta}{2}\right) \sin\theta \sum_{\ell=1}^{\infty} [E_{\ell+} - M_{\ell+} + E_{(\ell+1)-} + M_{(\ell+1)-}] (P''_{\ell} + P''_{\ell+1})
\end{aligned} \tag{2.4}$$

Where  $E_{\ell\pm}$  and  $M_{\ell\pm}$  are the electric and magnetic multipole amplitudes, with the +/- subscripts denoting the nucleon spin alignment as parallel/anti-parallel to the decay angular momentum respectively.  $P'$  and  $P''$  are the first and second order derivatives of the Legendre polynomials. The total cross section can be expressed as the sum of the of the squared helicity flip amplitudes, written as

$$\sigma = N^2 + S_A^2 + S_P^2 + D^2 \tag{2.5}$$

The helicity amplitudes can be combined to make four transversity amplitudes [47]. These are expressed as

$$\begin{aligned}
b_1 &= \frac{1}{2} [(S_P + S_A) + i(N - D)] \\
b_2 &= \frac{1}{2} [(S_P + S_A) - i(N - D)] \\
b_3 &= \frac{1}{2} [(S_P - S_A) - i(N + D)] \\
b_4 &= \frac{1}{2} [(S_P - S_A) + i(N + D)]
\end{aligned} \tag{2.6}$$

The transversity amplitudes are often used instead of the helicity amplitudes due to their connection to the spin observables accessible in experiments.

Bilinear combinations of the transversity amplitudes result in a total of 16 polarisation observables for pion photoproduction which are capable of being measured ex-

perimentally through different combinations of beam, target and recoil nucleon spin polarisation. The different observables are arranged into four groups of four, which outlines the different polarisation states required to access their measurement. The single type polarisation observables can be accessed by using no polarised states in the reaction or requiring just one of the three possible polarised states. The double type polarisation observables are accessed using combinations of two polarisation states. The double observables come in three sub-groups; the beam-target types require a polarised photon beam and a polarised nucleon target; the beam-recoil observables are accessed using a polarised photon beam in conjunction with measuring the degree of polarisation of the recoiling nucleon in the reaction; finally the target-recoil observables use a polarised target while measuring the polarisation of the recoiling nucleon. Table 2.1 outlines the 16 polarisation observables, their representation in the transversity amplitude notation, the combination of polarisations required to access them and which subgroup they fall into.

Observable	Transversity representation	Experiment (B/T/R)	Type
$\sigma_0$	$ b_1 ^2 +  b_2 ^2 +  b_3 ^2 +  b_4 ^2$	-/-/-	Single
$\Sigma$	$ b_1 ^2 +  b_2 ^2 -  b_3 ^2 -  b_4 ^2$	$P_L/-/-$	
T	$ b_1 ^2 -  b_2 ^2 -  b_3 ^2 +  b_4 ^2$	$-/P^y/-$	
P	$ b_1 ^2 -  b_2 ^2 +  b_3 ^2 -  b_4 ^2$	$-/-/y$	
G	$2Im(b_1b_3^* + b_2b_4^*)$	$P_L/P^z/-$	Beam-Target
H	$-2Re(b_1b_3^* - b_2b_4^*)$	$P_L/P^x/-$	
E	$-2Re(b_1b_3^* + b_2b_4^*)$	$P_{circ}/P^z/-$	
F	$2Im(b_1b_3^* - b_2b_4^*)$	$P_{circ}/P^x/-$	
$O_x$	$-2Re(b_1b_4^* - b_2b_3^*)$	$P_L/-/x'$	Beam-Recoil
$O_z$	$-2Im(b_1b_4^* + b_2b_3^*)$	$P_L/-/z'$	
$C_x$	$2Im(b_1b_4^* - b_2b_3^*)$	$P_{circ}/-/x'$	
$C_z$	$-2Re(b_1b_4^* + b_2b_3^*)$	$P_{circ}/-/z'$	
$T_x$	$2Re(b_1b_2^* - b_3b_4^*)$	$-/x/x'$	Target-Recoil
$T_z$	$2Im(b_1b_2^* - b_3b_4^*)$	$-/x/z'$	
$L_x$	$2Im(b_1b_2^* + b_3b_4^*)$	$-/z/x'$	
$L_z$	$2Re(b_1b_2^* + b_3b_4^*)$	$-/z/z'$	

Table 2.1: Single and double polarisation observables associated with pion photoproduction. The transversity amplitudes relating to each polarisation observable are shown. The polarisation states of the experiment required to access each observable are also shown in the format (Beam, Target, Recoil).

Relationships can be formed between the different polarisation observables which suggest an unambiguous solution to the transversity amplitudes can be formed without the need to measure all polarisation observables [48, 49]. A measurement of the four single polarisation observables  $\sigma_0$ ,  $\Sigma$ , T and P, as well as four appropriately chosen double polarisation observables can offer an unambiguous solution to the transversity amplitudes. There are several combinations of different polarisation observables offering unambiguous solutions to the four transversity amplitudes [50, 47, 51]. Despite the different possibilities for an unambiguous solution the uncertainties associated with the current data provide insufficient constraints to the observables and measurements of more than eight observables will be required [52].

## 2.2 Theory

The differential cross section gives a measure of the probability of observing the reaction's decay products in a particular kinematic region. This cross section can be sensitive to certain conditions of the experiment. In the case of this experiment the cross section is effected by the polarisation of the incident photon beam and the target. Using a polarised beam and target the differential cross section, expressed in terms of polarisation observables, can be written as

$$\begin{aligned} \frac{d\sigma}{d\Omega}(\theta, \phi) = & \frac{d\sigma_0}{d\Omega} \{1 - P_L \Sigma \cos(2\phi) \\ & + p^x (-P_L H \sin(2\phi) - P_{\odot} F) \\ & - p^y (-T + P_L P \cos(2\phi)) \\ & - p^z (-P_L G \sin(2\phi) + P_{\odot} E)\} \end{aligned} \quad (2.7)$$

where  $\frac{d\sigma}{d\Omega}(\theta, \phi)$  is the differential cross section,  $\frac{d\sigma_0}{d\Omega}$  is the unpolarised cross section,  $P_L$  and  $P_{\odot}$  are the degree of linear and circular polarisation of the photons respectively. The degrees of polarisation of the target are  $p^x$ ,  $p^y$ ,  $p^z$ , where z represents the direction along the beamline, x is the direction along the reaction plane and y is orthogonal to the reaction plane. The azimuthal angle of the  $\pi^0$  with respect to the photon linear polarisation plane is denoted  $\phi$ .  $\Sigma$ ,  $H$ ,  $F$ ,  $T$ ,  $P$ ,  $G$  and  $E$  are the polarisation observables accessible with different combinations of polarised beam and target.

Accessing the double polarisation observable  $G$  is achieved by using a linearly polarised photon beam and a longitudinally polarised target. A longitudinally polarised target has  $p_x = p_y = 0$  and  $P_{\odot} = 0$  for this experiment, which reduces the cross-section expression to

$$\frac{d\sigma}{d\Omega}(\theta, \phi) = \frac{d\sigma_0}{d\Omega} (1 + P_L \Sigma \cos(2\phi) + P_L P^z G \sin(2\phi)) \quad (2.8)$$

Only the  $\Sigma$  and  $G$  polarisation observables are accessible in this case, with the other

terms disappearing from the expression.

The center of mass frame in which the observables are extracted from the single  $\pi^0$  final state is given in Figure 2.7.

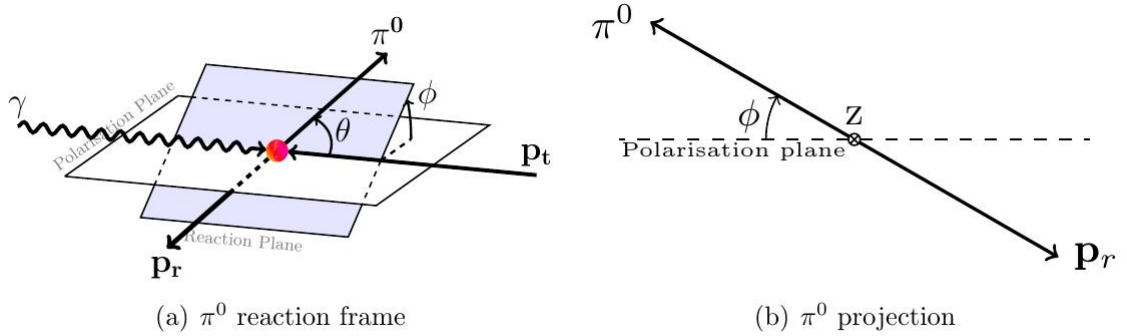


Figure 2.7: Reaction frame of the single  $\pi^0$  photoproduction experiment where  $\gamma$  is the incident photon,  $p_t$  is the target proton,  $p_r$  and  $\pi^0$  are the proton and photo-produced meson in the reaction respectively. Left: The reaction kinematics in the center of mass. Right: The reaction kinematics projected along the beam axis. The angle  $\phi$  is the azimuthal angle with respect to the reaction plane used in calculating the polarisation observables, and  $\theta$  is the polar angle with respect to the beam axis. Taken from [53]

The following chapter outlines previous work done at various facilities in order to measure the  $\Sigma$  and  $G$  polarisation observables. The experimental set-ups of each facility, the kinematics and the significance of their results are also discussed. Partial wave models are introduced and other recent measurements of observables are noted.

# Chapter 3

## Previous Work

This chapter presents previous measurements of the polarisation observables  $\Sigma$  and  $G$  which are the subject of this work, outlining the different facilities and conditions they were performed under (Section 3.1). The various theoretical models used to predict values of the polarisation observables are also discussed (Section 3.2). In addition, other recently measured polarisation observables are presented as they are required to achieve a model independent solution for the partial wave amplitudes (Section 3.3).

### 3.1 Previous measurements

Previous experimental work investigating  $\pi^0$  photoproduction began as far back as 1952 [54], with photon asymmetry ( $\Sigma$ ) measurements in 1964 [55]. The first beam-target polarisation observable ( $G$ ) measurements were made in 1979 [56].

#### 3.1.1 $\Sigma$ measurements

##### LEGS

The Laser Electron Gamma Source (LEGS) facility at Brookhaven National Laboratory extracted the beam asymmetry  $\Sigma$  and cross-section measurements for the

$p(\vec{\gamma}, \pi^0)$ ,  $p(\vec{\gamma}, \pi^+)$  and  $p(\vec{\gamma}, \gamma)$  in a single experiment [57].

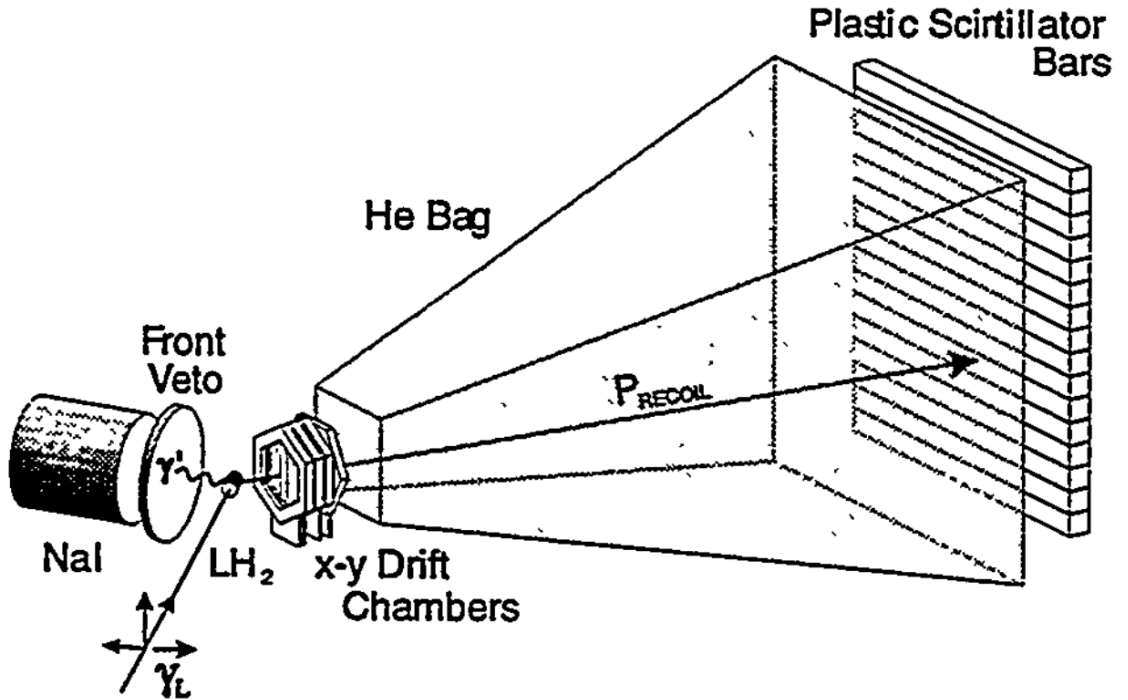


Figure 3.1: Schematic of the LEGS detector. Taken from [58].

The facility used laser backscattering to produce highly polarised photons from 2.6 GeV electrons at the National Synchrotron Light Source. The  $\gamma$ -ray beam produced photons with an energy range of  $E_\gamma = 200 - 300$  MeV, and with a degree of linear polarisation greater than 80% (known to  $\pm 1\%$ ). The orientations of the photons were flipped between parallel and perpendicular to the scattering plane at random intervals between 150 and 450 seconds. The decay photons from the  $\pi^0$  were detected in the NaI(Tl) detector. The recoil protons were tracked through wire chambers and plastic scintillators were used to measure their energies (time of flight measurements were also used).

The results from this measurement are shown with the MAMI results in Figure 3.9 as blue crosses in the first three panels at 280, 200 and 320 MeV.

## Yerevan

The Yerevan facility, shown in Figure 3.2, used an electron beam of 3 - 3.5 GeV to produce linearly polarised photons. The photon energy range covered in this work was  $E_\gamma = 0.5 - 1.1$  GeV with the angular coverage of  $\theta_{\pi^0} = 85^\circ - 125^\circ$ . The kinematic binning was energy steps of 25 MeV and angular steps of  $5^\circ$ . The angular range in the Yerevan facility is limited due to the two arm set up shown in Figure 3.2.

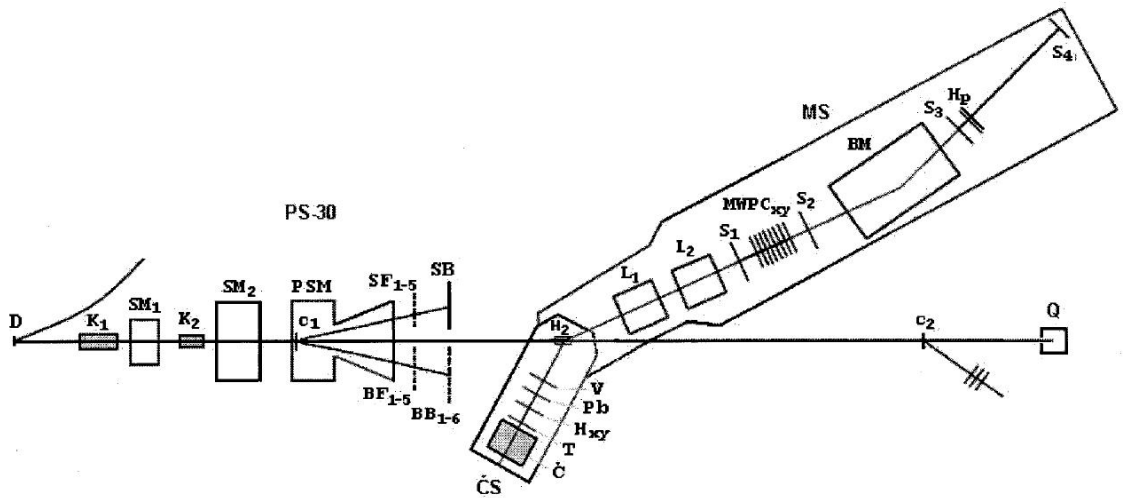


Figure 3.2: Schematic of the Yerevan set-up. The linearly polarised photons are produced at D (the diamond radiator), the recoil protons are detected in the MS arm of the set up and the  $\pi^0$  decay photons are detected in the Čerenkov detector ( $\check{C}S$ ). Taken from [59].

The  $\Sigma$  results from the  $\gamma p \rightarrow \pi^0 p$  reaction at Yerevan significantly increased the statistics on the measurement in the second and third resonance regions. The results agreed with existing experimental data, shown in Figure 3.3.

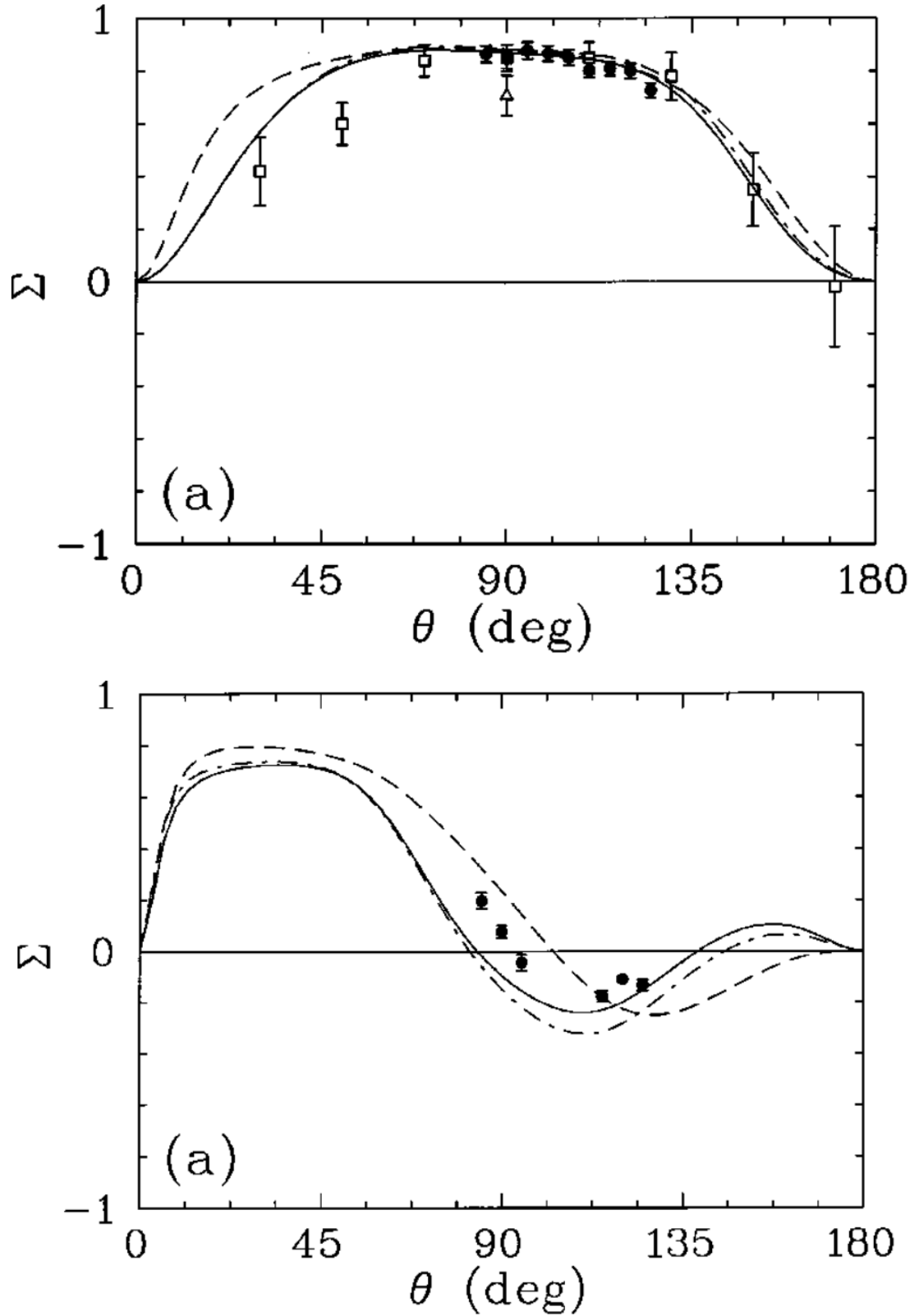


Figure 3.3:  $\Sigma$  results from the  $\gamma p \rightarrow \pi^0 p$  reaction. Top: angular dependence of  $\Sigma$  at incident photon energy  $E_\gamma = 700$  MeV. Bottom: angular dependence of  $\Sigma$  at incident photon energy  $E_\gamma = 950$  MeV. Results are plotted against the theoretical curves from WI00 (solid line), FA00 (dashed-dotted line) and MAID 2000 (dashed line). Taken from [59].

## GRAAL

The GRAAL (GRenoble Anneau Accélérateur Laser) facility, shown in Figure 3.4, used Compton back scattering of laser photons off electrons stored in the European Synchrotron Radiation Facility (ESRF), to produce highly linearly polarised photons. The photons were produced using a laser with two wavelengths, 351nm UV laser photons and 514nm visible line laser photons. The electrons used in the back scattering had an energy of 6.03 GeV. The degree of linear polarisation peaked at 98%.

The energy range covered by GRAAL was  $E_\gamma = 550 - 1500$  MeV, with a  $2\pi$  azimuthal angular coverage and a center of mass polar angle coverage of  $\theta_{CM} = 40^\circ - 170^\circ$ . The 1100-1500 MeV range for  $\Sigma$  was covered for the first time with this work. The results are shown in Figure 3.5.

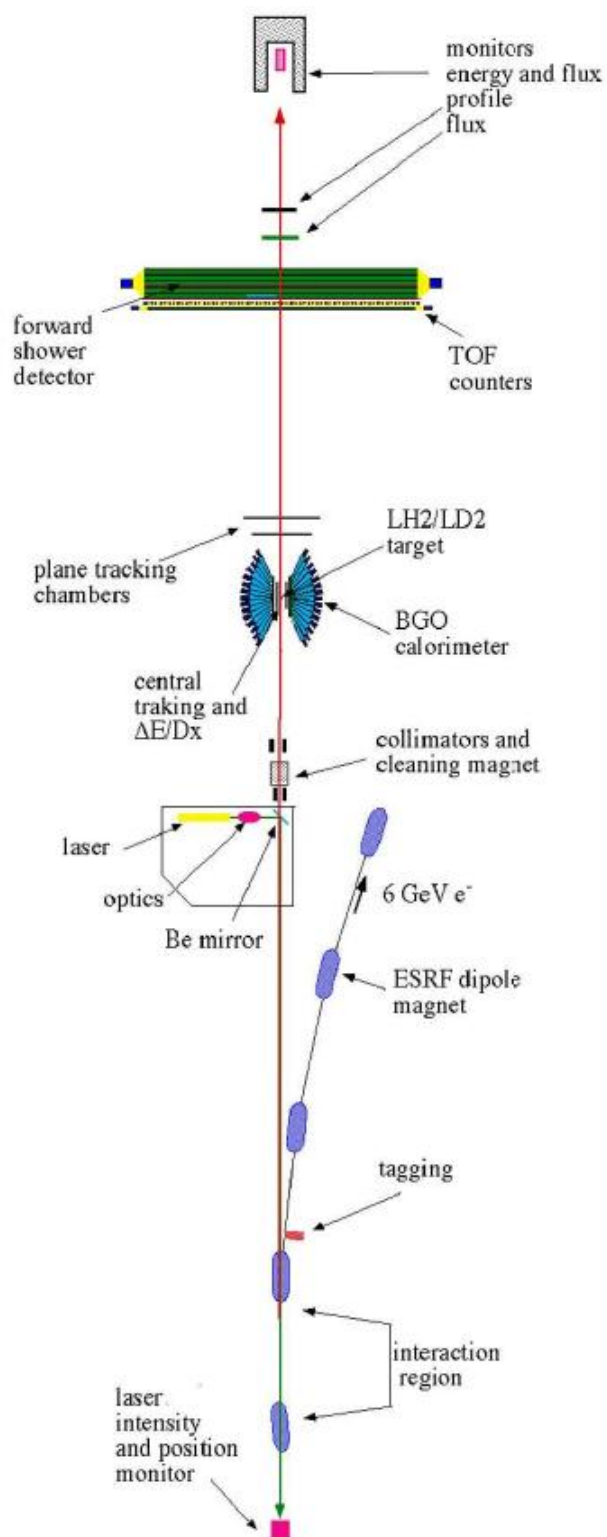


Figure 3.4: Schematic of the GRAAL set-up. Taken from [60].

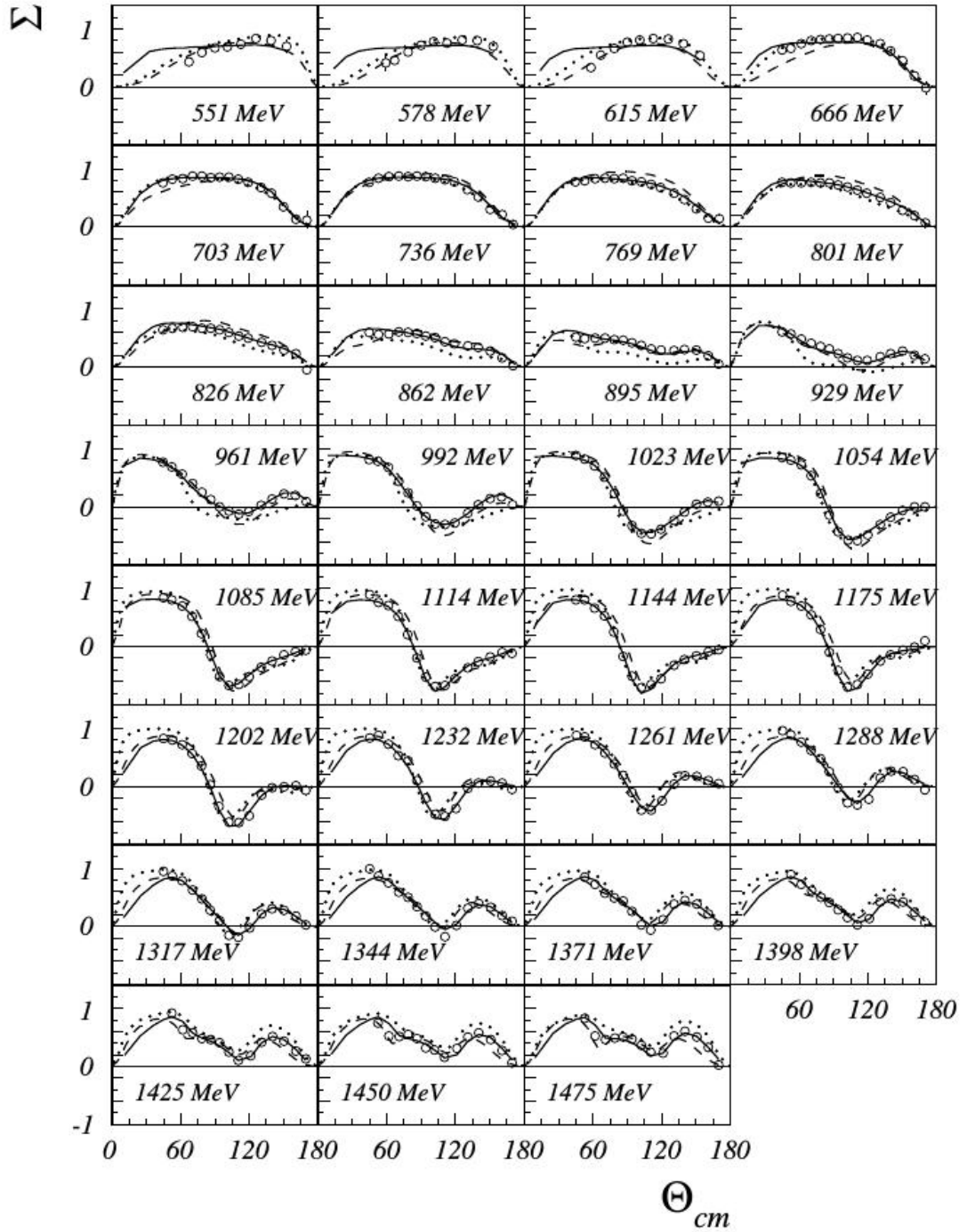


Figure 3.5: GRAAL angular results of beam asymmetry  $\Sigma$  from the reaction  $\gamma p \rightarrow \pi^0 p$  compared to theory predictions, SAID-FA04 (dashed line), MAID2005 (dotted line) and Bonn2005 (solid line). Taken from [60]

### CBELSA

The Crystal Barrel set up at ELSA in Bonn is shown in Figure 3.6. CBELSA is a coherent bremsstrahlung facility similar to A2-MAMI (Section 4.1). ELSA is the continuous wave electron accelerator which provided a 3.175 GeV beam. The crystal barrel consisted of 1290 CsI(Tl) crystals and the TAPS detector, covering the forward polar angles ( $5^\circ$  to  $30^\circ$ ), itself consisting of 528 hexagonal BaF<sub>2</sub> crystals.

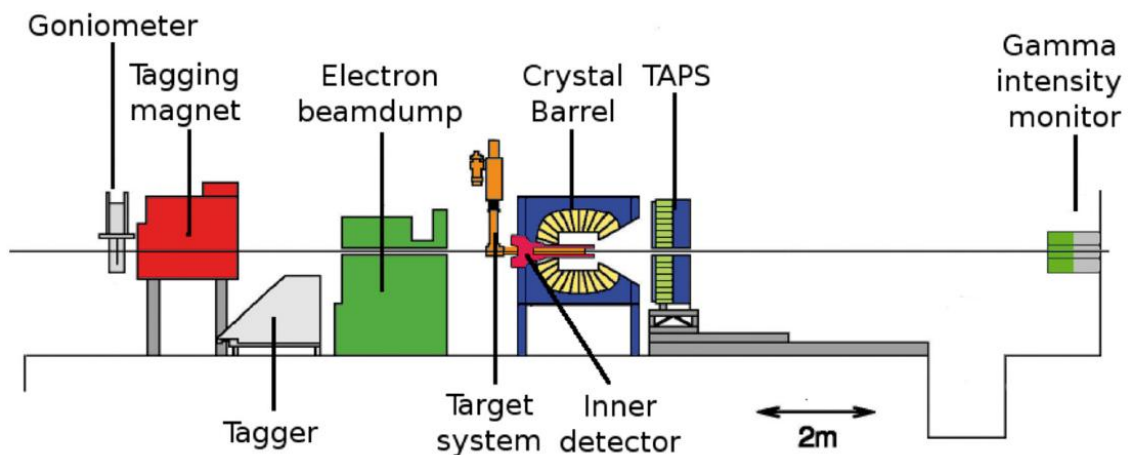


Figure 3.6: Schematic of the CBELSA detector. Taken from [33].

The results from the CBELSA measurements [61, 62] cover an energy range of  $767 < E_\gamma < 1680$  MeV, with an angular range of  $6^\circ < \theta < 168^\circ$ . The acceptance of the detector set up is 99% of  $4\pi$  sr. The degree of linear polarisation achieved was up to 49%. The majority of the results from these measurements cover an energy range higher than in this work.

### Mainz A2 Hall

The A2 hall at MAMI uses coherent bremsstrahlung to produce a linearly polarised photon beam off a diamond radiator using an electron beam. The current set up is described in detail in chapter 4. Several measurements of  $\Sigma$  in the  $\gamma p \rightarrow \pi^0 p$  reaction have been made previously at the A2 hall in Mainz. These measurements have used a different detector set up to the one used for the measurement presented in this thesis.

The previous work by Beck et al. [63] was performed before the MAMI upgrade (MAMI C) with the central detector DAPHNE (Detecteur à grande Acceptance pour la PHysique photoNucleaire Experimentale)[64, 65]. MAMI provided an electron beam up to 855MeV with the Glasgow tagger able to tag a photon beam up to 800MeV.

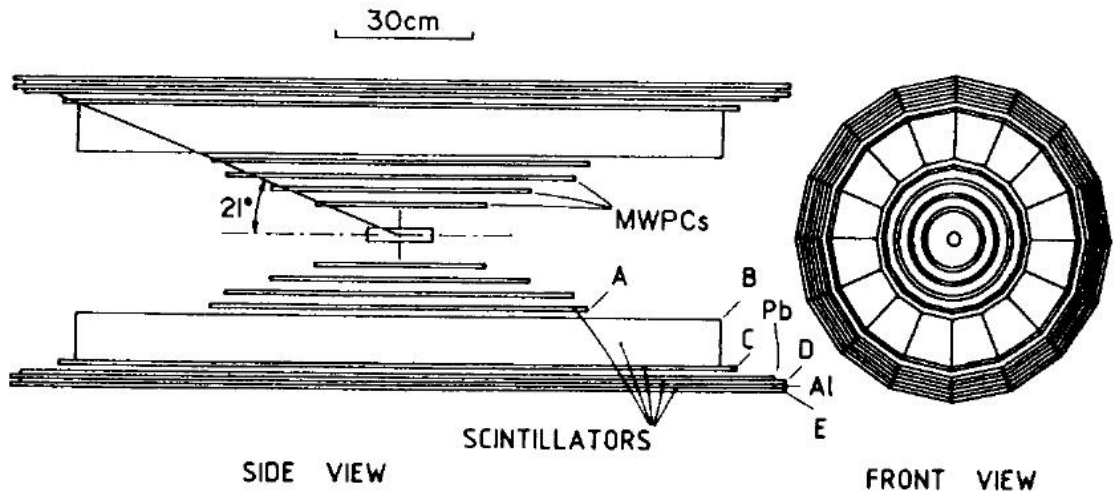


Figure 3.7: The central DAPHNE detector. Taken from [64].

The DAPHNE detector was a multi-layered, segmented central detector which provided a full  $2\pi$  azimuthal coverage and lab polar angles of  $21^\circ < \theta_{lab} < 159^\circ$ . The angular coverage was 94% of  $4\pi$  sr total angular acceptance. This work covered measurements of  $\Sigma$  between energies of  $270 < E_\gamma < 420$  MeV where sufficient polarisation was obtained through the coherent bremsstrahlung method.

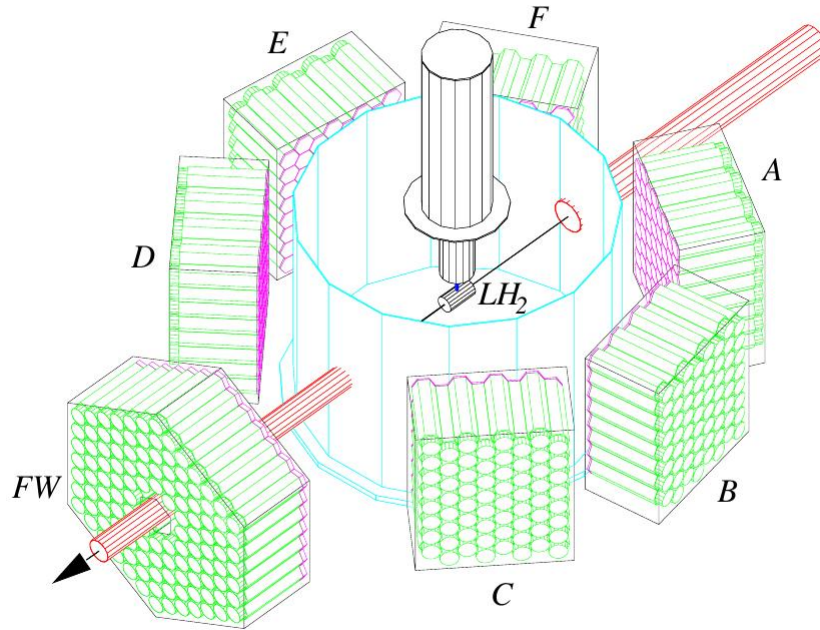


Figure 3.8: Previous configuration where the TAPS configuration differs from current set up, surrounding the target and acting as the main detector. Full  $2\pi$  azimuthal coverage is sacrificed in this set up to increase previous polar angle coverage. Taken from [66].

Further work by Beck et al. [67] was performed using the TAPS detector arranged as shown in Figure 3.8. This configuration allowed the polar angular acceptance to increase to  $12^\circ < \theta_{CM} < 170^\circ$ , however the full  $2\pi$  azimuthal acceptance was lost. The results covered an energy range of  $240 < E_\gamma < 440$  MeV.

The results from these two A2 measurements as well as LEGS are presented in Figure 3.9, where good agreement can be seen between the results.

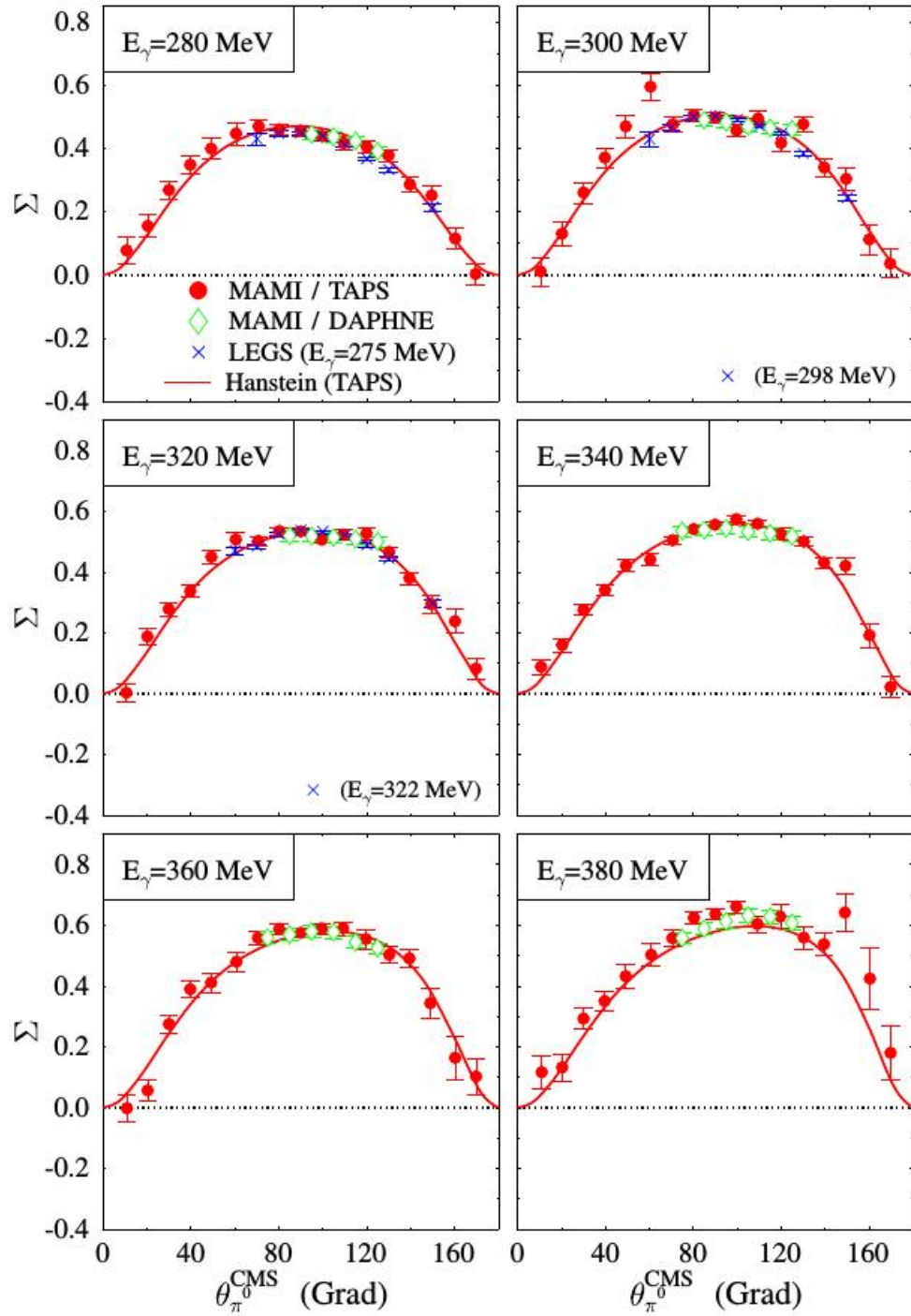


Figure 3.9:  $\Sigma$  results from the  $\gamma p \rightarrow \pi^0 p$  reaction at the TAPS/DAPHNE experiments performed at the A2 hall in Mainz. Red circles from the TAPS set up, green diamonds from the DAPHNE set up [63], blue cross from LEGS [57]. Data is plotted against theoretical analysis by Hanstein [68]. Taken from [67].

Separate measurements by Hornidge et al. [69] and Gardner et al. [70] were performed after the MAMI upgrade, increasing the available incident electron beam

energy, using the same detector configuration as this measurement (see Chapter 4). The measurement by Hornidge et al. focused on the energy range close to the  $\pi^0$  threshold, using a MAMI B electron beam energy of 855 MeV to achieve this. The results from this measurement covered an incident photon energy range between  $145 < E_\gamma < 180$  MeV and  $-1 < \cos\theta < 1$ . In the region measured, the degree of linear polarisation of the bremsstrahlung photons was 50% - 70%.

The most recently published results by Gardner et al. closed a gap in the global data set for measurements of  $\Sigma$ . The incident electron beam had an energy of 1508 MeV coming from MAMI C with measurements made for incident photon energies between  $320 < E_\gamma < 650$  MeV. A 97%  $4\pi$  sr acceptance was achieved using the current detector set up, with the TAPS detector configured as in Section 4.7.3. The degree of polarisation in this measurement ranged from 4% at  $E_\gamma = 320$  MeV, up to a maximum of 53% at  $E_\gamma = 632$  MeV.

The work greatly increased the kinematic range and precision of the beam asymmetry previously measured. A momentum analysis was able to be performed due to the high statistics in combination with previous measurements of cross-sections. Comparison with the Bonn-Gatchina model calculations suggested a small interference between F-waves and the  $N(1440)\frac{1}{2}^+$ ,  $N(1535)\frac{1}{2}^-$  and  $N(1520)\frac{3}{2}^-$  resonances, and constrained higher partial waves further.

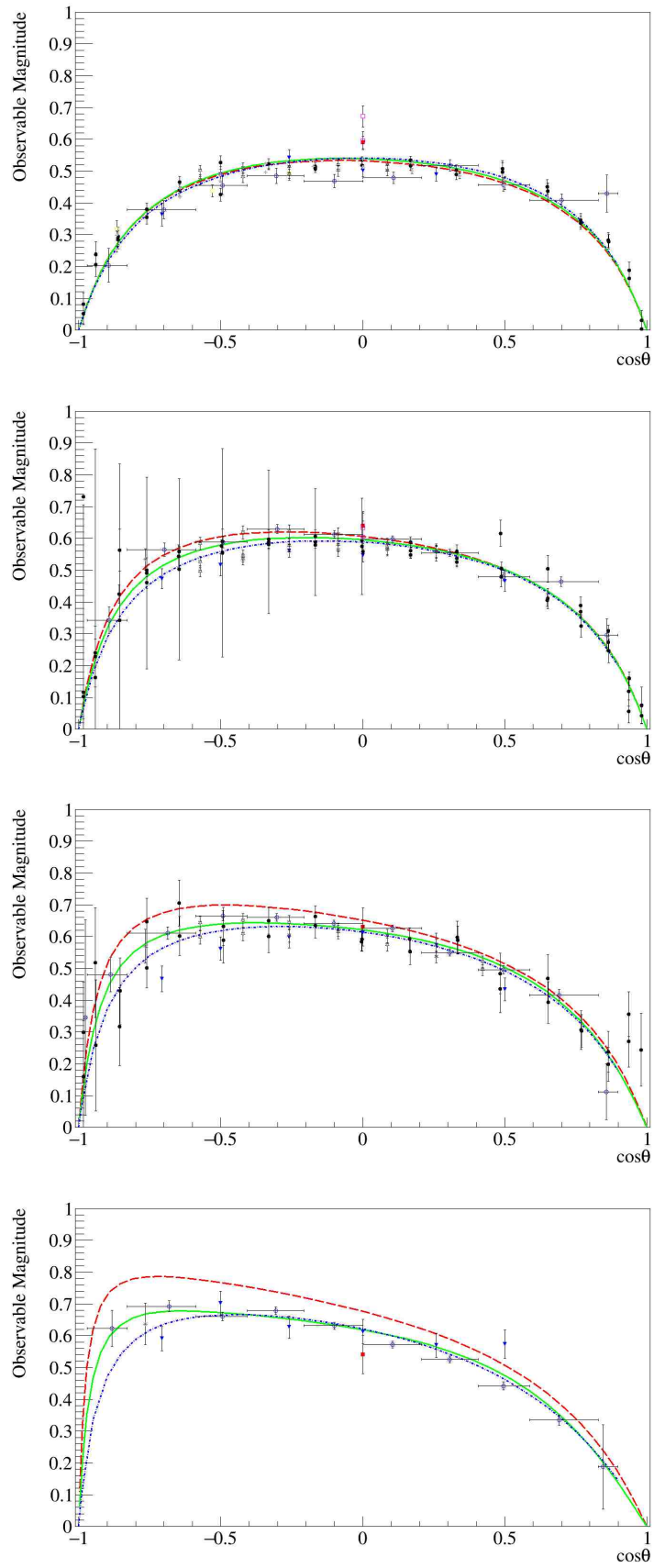


Figure 3.10: Beam asymmetry  $\Sigma$  dependence on  $\cos\theta_{CM}$  from the reaction  $\gamma p \rightarrow \pi^0 p$ . Data from Gardner et al. [70] (Blue open circles). The PWA predictions are shown as coloured lines: MAID [71] (red), SAID [72] (green) and Bonn-Gatchina [73] (blue).

### 3.1.2 G measurements

There are significantly fewer previous measurements of the beam-target polarisation observable  $G$  in the  $\gamma p \rightarrow \pi^0 p$  reaction channel, with only 3 datasets currently being included in the world data set used with the PWA solutions. The measurements include work by Ahrens et al. [74] and Bussey et al. [56]. The most recent work on  $G$  was published in January 2017 by Thiel et al. [75]. This work greatly increases the kinematic region not previously measured.

#### Daresbury Laboratory

The first measurement of the beam-target polarisation observable  $G$  was done by Bussey et al. at Daresbury Laboratory in the UK in 1979 [56]. The measurements were done for an incident photon energy  $1300 < E_\gamma < 2300$  MeV and a  $\pi^0$  center of mass polar angles  $50^\circ < \theta < 80^\circ$ . Although the angular regions covered were small, it offered the first measurements of the  $G$  observable to constrain theoretical models and is included in the current world dataset.

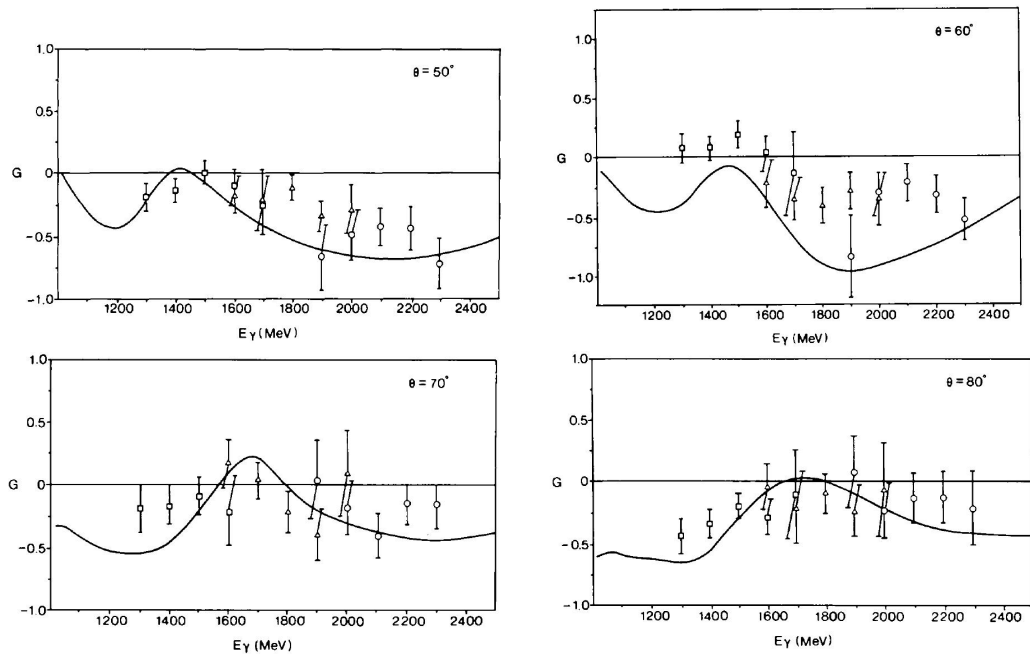


Figure 3.11: First results of the beam-target polarisation observable  $G$  from the reaction  $\gamma p \rightarrow \pi^0 p$ . Taken from [56]

## MAMI

The previous measurement of  $G$  at MAMI in Mainz was performed using the DAPHNE set up described in Subsection 3.1.1[74]. Data was taken using an linearly polarised photon beam with incident energy  $E_\gamma = 340$  MeV for  $\theta_{lab} = 70^\circ, 90^\circ$  and  $110^\circ$ . Only three data points were extracted for  $G$  in the  $\pi^0$  final state and six for the  $\pi^+$  final state (Figure 3.12). The data taken provided constraints for partial wave solutions in the  $\Delta$  resonance region.

There is a necessity for further measurements due to the coarse, imprecise data on the double polarisation observable  $G$  in the  $\gamma p \rightarrow \pi^0 p$  reaction. Further, more precise measurements such as those presented in this thesis allow a larger kinematic region to be covered which aids the partial wave analysis predictions of different models towards a model independent solution.

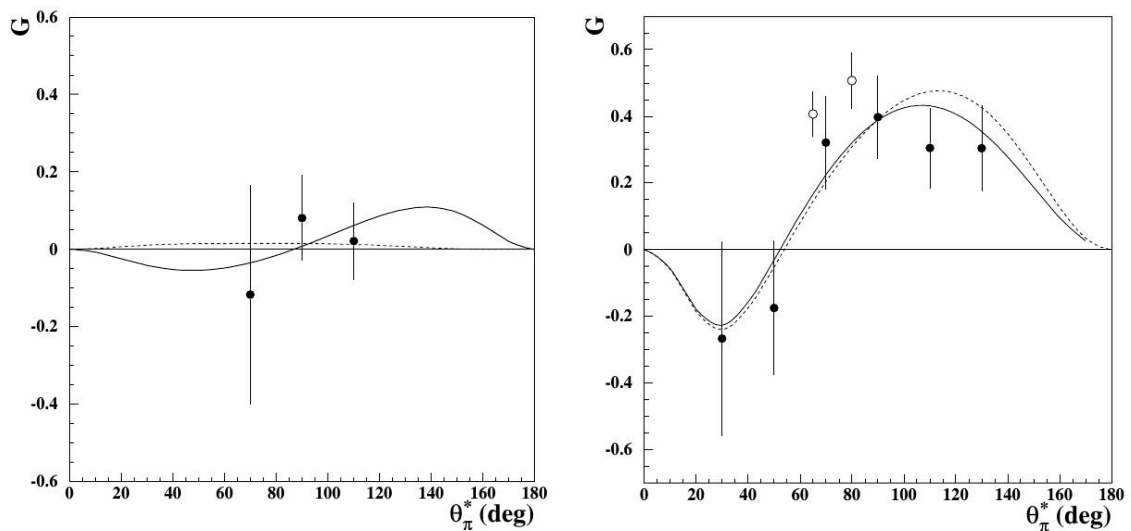


Figure 3.12: Beam-target polarisation observable  $G$  measured for the  $\pi^0$  (left) and  $\pi^+$  (right) final states. The measurements are plotted alongside the solid (dashed) lines representing the MAID2003 (SAID- FA04K) multipole analyses solutions. Taken from [74].

## CBELSA

The  $G$  results from CBELSA in Bonn [75], shown in Figure 3.13, were obtained using an incident electron beam of  $E_\gamma = 3.2$  GeV to produce linearly polarised photons

through coherent bremsstrahlung, with a maximum degree of polarisation of 65% at 950 MeV. The polarised photons were incident on a longitudinally polarised frozen spin Butanol target with a typical polarisation degree of 80%. The energy range measured was  $617 < E_\gamma < 1325$  MeV with the detector set up covering the full azimuthal range and polar angular range of  $1^\circ < \theta_{lab} < 156^\circ$ . The data taken covers a significant kinematic region not previously measured (318 new data points), and offers constraints on the multipole solutions from different analyses, with an overlap with data measured in this analysis.

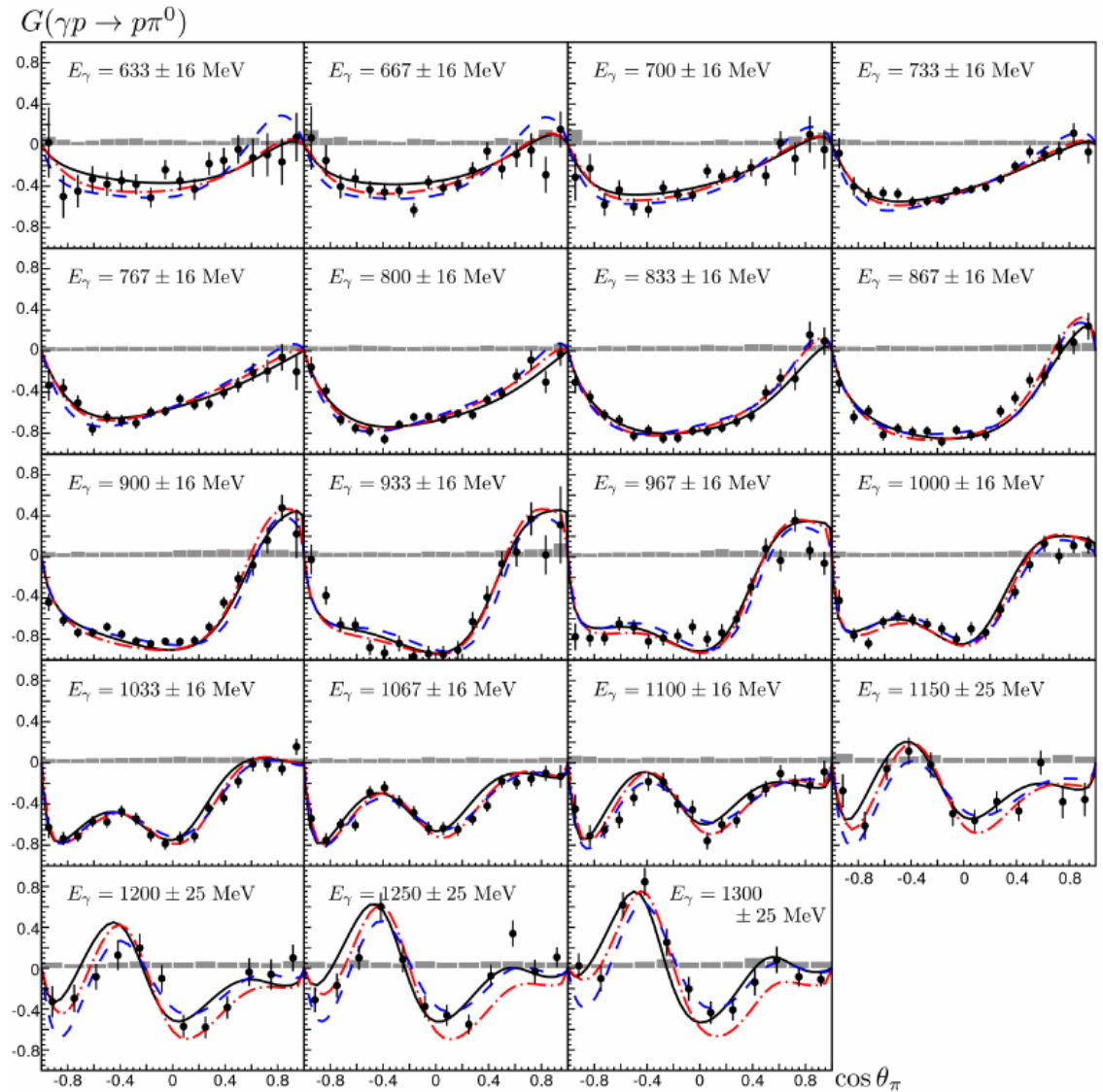


Figure 3.13: Double polarisation observable  $G$  in  $\pi^0$  photoproduction off the proton using the CBELSA/TAPS experiment at ELSA accelerator in Bonn. The MAID 2007, SAID CB12, Jülich-Bonn 2013-01 and Bonn-Gatchina 2011-02 partial wave curves are compared against the data, shown by the green (dotted), red (dashed-dotted), blue (dashed) and black (solid) lines respectively.

## 3.2 Partial Wave Analysis

Information regarding multipole decomposition of reaction amplitudes on the excitation spectrum of the nucleon is inferred using partial wave analyses. Various models perform fits to world data sets of cross-section, photo- and electro-production data, with the purpose of determining properties of baryon resonances. The main models used are described briefly in this section.

### 3.2.1 MAID

MAID is a unitary isobar model [76, 77] which approximates the resonant spectrum of the nucleon. MAID selects the four star  $N^*/\Delta$  resonances from the PDG database [17] below 2 GeV and fits Breit-Wigner dependent partial waves to these data. As such it does not identify new resonances but extracts the properties of those already known.

The model predicts values for both polarisation observables and differential cross-sections in  $\pi^0$  photoproduction experiments. The different resonance contributions can be selected to present unique solutions to the different polarisation observables, showing relative sensitivity to different resonances. The latest update of the MAID model was done in 2007 and values of observable approximations can be accessed online.

### 3.2.2 SAID

The SAID model [78, 79] is a model independent partial wave analysis. It uses the world dataset of  $\pi N$  scattering to constrain fit parameters. It is similar to the MAID model but makes no assumptions of the resonances included in the fit. The various resonances present themselves as peaks in the partial wave distributions.

The SAID model (SAID PR15 [80]) is more recently updated than the MAID model with measurements from older  $\pi N$  scattering, and newer pion photoproduction mea-

surements, included in the latest fit.

### 3.2.3 Bonn-Gatchina

The Bonn-Gatchina (BnGa) is a multi-channel partial wave model similar to the SAID model, making no assumptions of the resonances included in the fit solutions. The BnGa model also uses the world dataset of  $\pi N$  scattering but includes additional information from meson photoproduction and other reaction processes [81, 73]. The model provides predictions for  $\pi^0$  photo-production experiments, with the latest fits presented in reference [33].

## 3.3 Other observables

In order to obtain model independent solutions in extracting partial wave amplitudes a comprehensive study on several polarisation observables needs to be done to sufficiently large kinematic ranges. With enough polarisation observables measured to constrain different models the solutions should converge on a single model independent solution. A few notable recent studies on polarisation observables are mentioned in this section to outline other work aimed at achieving this end goal.

### 3.3.1 T and F beam-target observables

Previous work by Annand et al. [82] measured the target asymmetry and beam helicity asymmetries T and F. The detector configuration used the current A2 set up at MAMI (see Chapter 4). With an incident electron energy of 1557 MeV the measurements were made for a photon energy range  $425 < E_\gamma < 1450$  MeV. Circularly polarised photons were incident on a frozen spin transversely polarised butanol target. The degree of circular polarisation ranged from 35% at 425 MeV to 78% at 1450 MeV and the average target polarisation was 70%. The results from this measurement supported observations that the partial wave solutions of extracted

resonance amplitudes from different models begin to converge on model independent values.

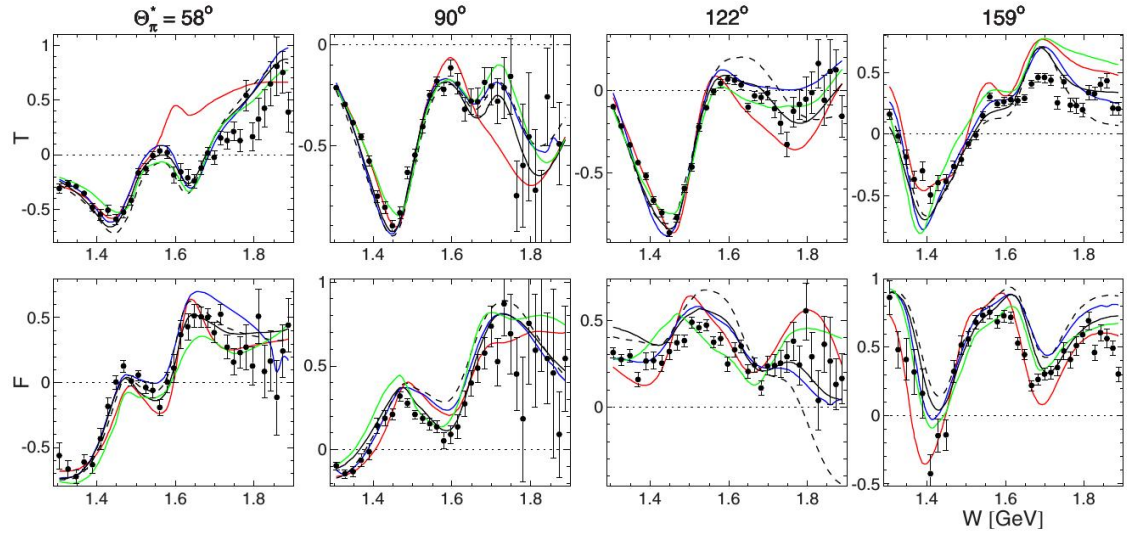


Figure 3.14: T and F observables in the  $\gamma p \rightarrow \pi^0 p$  reaction as a function of center-of-momentum energy  $W$  for a range of polar angular bins (Shown above plots). Data (black circles) compared to the different theoretical models MAID 2007 (red), SAID PR15 (blue) and Bonn-Gatchina (solid black). Taken from [82].

### 3.3.2 $C_x$ beam-recoil observable

As well as single and beam-target polarisation observables there are beam-recoil polarisation observables. Previous work by Sikora et al. [83] measured the beam-recoil polarisation observable  $C_x$ . The measurement was done at the A2 hall at MAMI using a slightly different set up to the current detector set up.

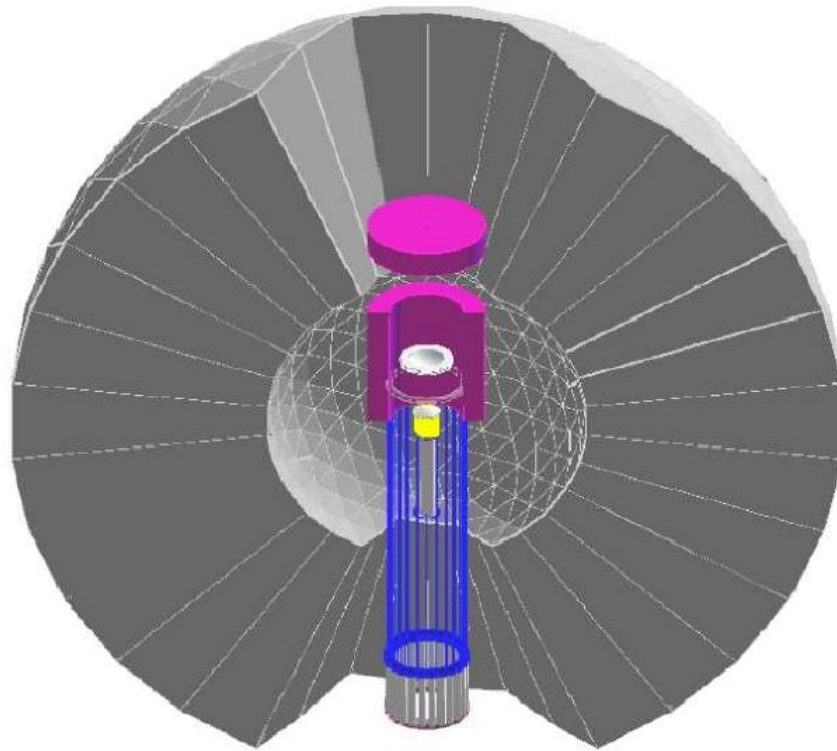


Figure 3.15: The purple volumes show the additional graphite polarimeter material added to the standard CB setup. Taken from [83].

There was the addition of a graphite polarimeter within the CB detector which gave access to spin transfer observables, Figure 3.15. It presented a new technique to measure the spin of the recoiling nucleon in nuclear and hadronic reactions.

The measurement used a circularly polarised photon beam with an energy range of  $E_\gamma = 400 - 1400$  MeV, and a liquid hydrogen target. The degree of circular polarisation ranged from 30% - 80% over the incident photon energy range. The results showed better agreement with the latest (at the time) SAID Chew-Mandelstam parameterisation giving the best  $\chi^2/N$  value of 1.7. It was concluded the results presented strong evidence for using the Chew-Mandelstam formalism in reliable extraction of information on the nucleon excitation spectrum.

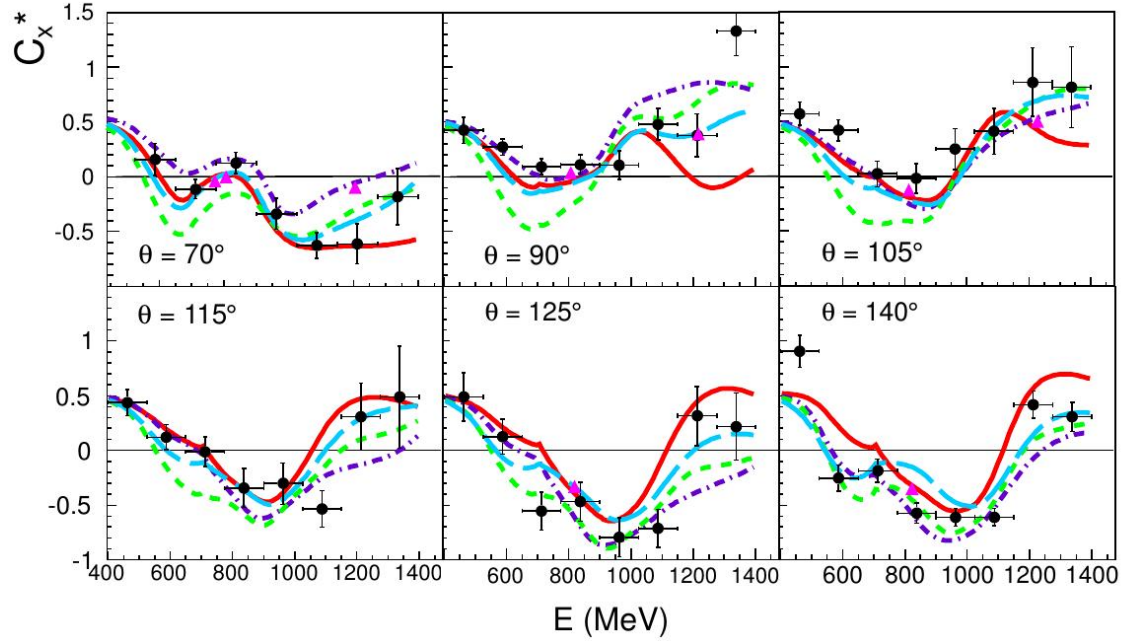


Figure 3.16: The beam-recoil polarisation observable  $C_x$  in the reaction  $\gamma p \rightarrow \pi^0 p$  off a liquid hydrogen target for fixed pion  $\theta_{CM}$  angles. The results (black points) are presented alongside theoretical models MAID 07 (violet dashed-dotted line), SAID CM12 (cyan dashed line), SAID SN11 (green dashed line) and BnGa2011-2 (red line). Taken from [83].

Many polarisation observables have become accessible in recent years thanks to the advances made in polarised beams and targets at facilities such as MAMI, Jefferson Lab and CBELSA. The developments at these facilities have increased the kinematic range measured for several observables and offered access to beam-target polarisation observables like  $G$ ,  $H$ ,  $E$  and  $F$ . Further developments in recoil polarisation have also allowed access to beam-recoil and target-recoil polarisation observables. Ongoing efforts will provide further measurements which will act as constraints to partial wave analyses over a sufficiently large kinematic range and converge towards a model independent solution in extraction of excited nucleon resonance amplitudes.

# Chapter 4

## Experiment

The data-taking for this experiment took place from November 2013 to September 2015. As described in the previous chapter the aim was to measure the beam-target polarisation observable  $G$  as well as the beam asymmetry  $\Sigma$ . It used a high duty factor electron beam at 1557 MeV incident energy. A diamond radiator was used to produce a highly linearly polarised photon beam through coherent bremsstrahlung. Two orthogonal settings of the polarisation plane were used ( $\pm 45^\circ$  relative to the detector's equatorial plane) and the observables were extracted by making asymmetries of the two datasets, minimising systematic errors related to detector acceptance. A longitudinally polarised frozen-spin butanol target was used as a proton target. In addition data were taken with a carbon target and used to account for the background from the oxygen and carbon in the butanol target.

## 4.1 MAMI

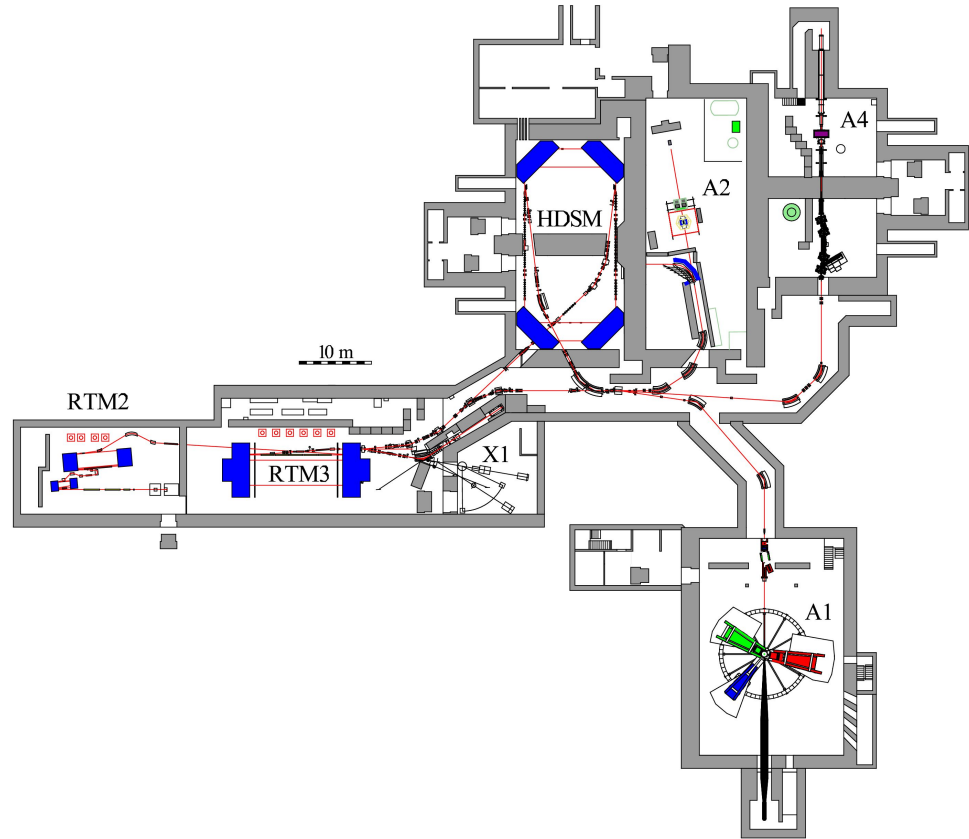


Figure 4.1: Overview of the entire MAMI facility. Three racetrack microtrons and a Harmonic Double-Sided Microtron provide an electron beam of up to 1.6 GeV. The electron beam can be fed into four experimental halls which are also shown (A1, A2, A4 and X1).

The MAInzer MIcrotron (MAMI), located at Institut für Kernphysik at Johannes Gutenberg University Mainz, provides a continuous-wave electron beam to three separate experimental halls, X1, A1 and A2 (Figure 4.1). The electrons are accelerated through a linear accelerator (LINAC) injector magnet, a series of three race-track microtrons (RTMs) and finally a harmonic double-sided microtron (HDSM). The linear accelerator injects the electrons with an energy of 4.1 MeV into the RTMs.

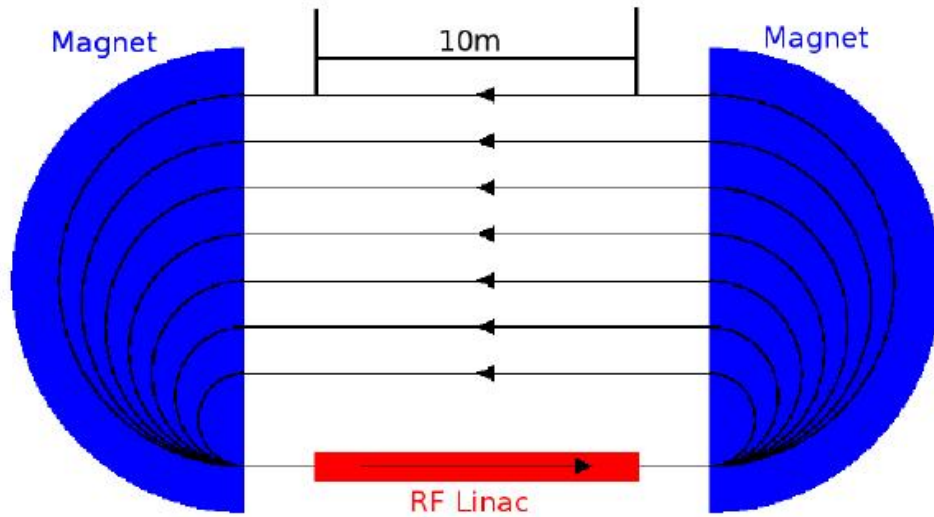


Figure 4.2: Schematic of a race-track microtron.

Each RTM consists of a LINAC and two dipole magnets, as illustrated in Figure 4.2. The LINAC accelerates the electrons along the initial stage of a series of recirculation tracks. The dipole magnet bends the electron round  $180^\circ$  where it is passed through a focusing device. A second dipole magnet bends the electron back through  $180^\circ$  into the LINAC once again. Each subsequent pass of the LINAC accelerates the electrons further and increases the momentum which results in a larger radius of curvature in the bending magnets. The electrons are ejected from each RTM with endpoint energies of 15.3 MeV, 185.9 MeV, and 883.1 MeV respectively.

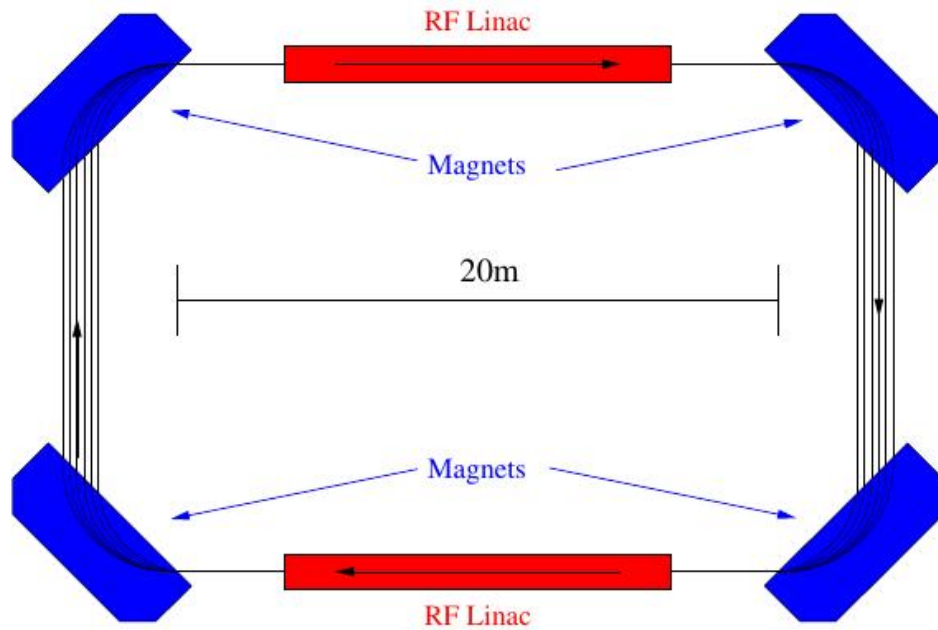


Figure 4.3: Schematic of a harmonic double-sided microtron.

The final ejection from the RTMs is passed onto the harmonic double-sided microtron. The HDSM consists of two LINACS and four dipole bending magnets, shown in Figure 4.3. This design is due to the fact that in order to accelerate the electrons beyond 883 MeV (up to 1.6 GeV) an RTM design is not practical within the space available at MAMI and would require bending magnets weighing over 2000 tonnes each. The bending magnets of the HDSM are only required to bend the electrons by  $90^\circ$  and as such the respective size of each magnet is reduced. The ejection energy of the HDSM can be provided up to almost 1.6 GeV and is detailed in Table 4.1.

Stage	Input Energy (MeV)	Output Energy (MeV)	Number of turns
Injector		4.1	
RTM1	4.1	15.3	18
RTM2	15.3	185.9	51
RTM3	185.9	883.1	90
HDSM	883.1	1557	43

Table 4.1: Table listing energies of electrons at each stage of the MAMI accelerator.

## 4.2 Bremsstrahlung

The A2 hall uses the bremsstrahlung process to produce high energy real photons. Bremsstrahlung occurs when an incoming high energy electron is decelerated in the electromagnetic field of an atomic nucleus. The electrons are incident on a radiator held in the goniometer (see Section 4.4). The lost energy, in a single interaction, due to the acceleration is emitted as a photon with energy equal to the difference in incoming and outgoing electron (Equation 4.1).

$$E_\gamma = E_0 - E_F \quad (4.1)$$

The characteristic shape of a bremsstrahlung spectrum binned in photon energy is proportional to  $1/E_\gamma$  relationship, due to the interaction strength between the electron and nuclei being inversely proportional with the distance between them. This can be seen in Figure 4.4. The higher tagger channels correspond to a lower bremsstrahlung photon energy. The efficiency of the different tagger channels is not 100%, which can be seen as fluctuations in the distribution. See Section 4.6 for details of the bremsstrahlung photon energy measurement.

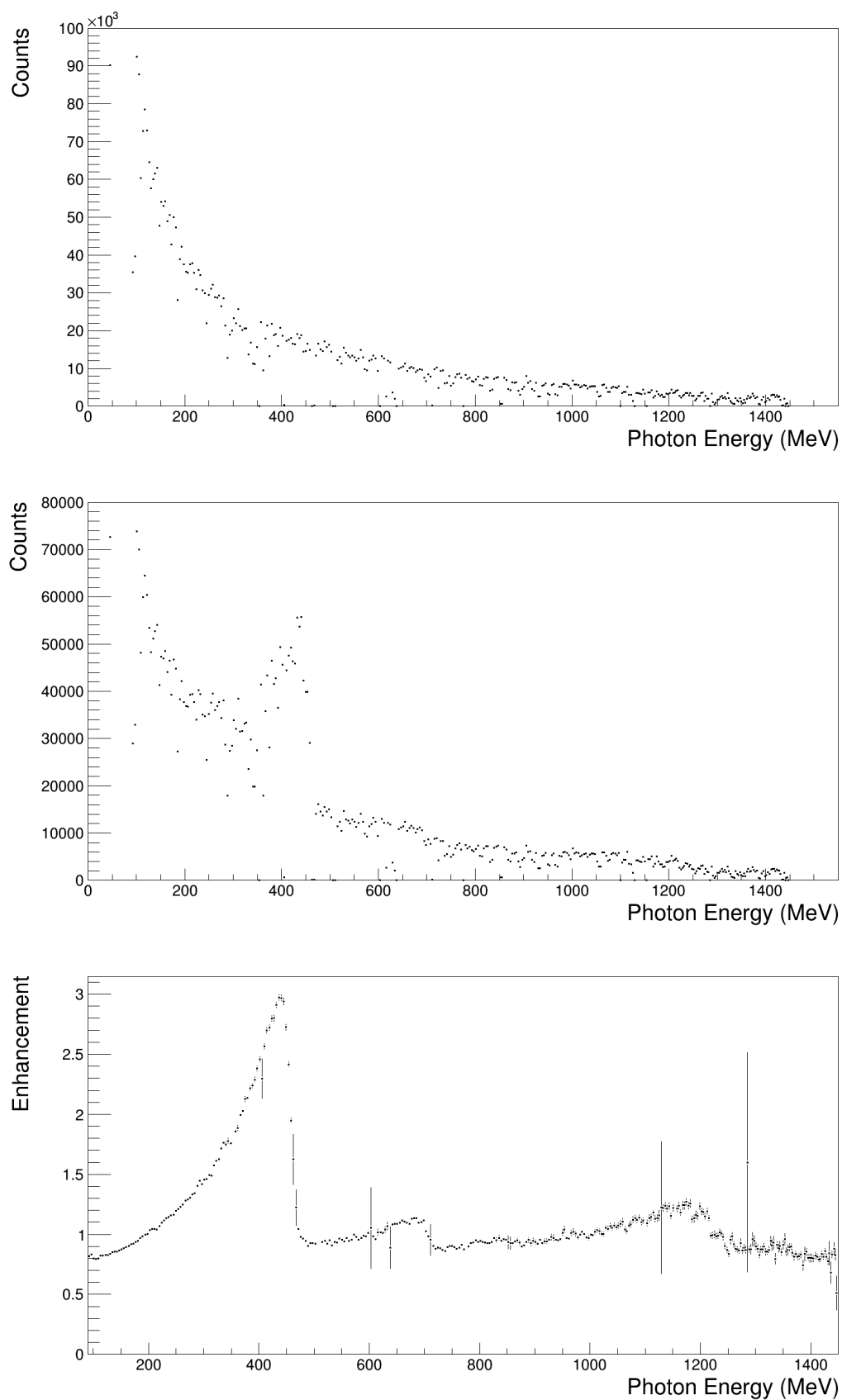


Figure 4.4: The top plot shows the measured energy distribution of the tagged photons using an amorphous radiator. The middle plot shows the same with an aligned diamond radiator. The bottom plot shows the ratio of these, "enhancing" the coherent structures resulting from the diamond lattice vectors.

## 4.3 Coherent Bremsstrahlung

An important feature of the MAMI facility is the ability to produce linearly polarised photons through coherent bremsstrahlung. Using a diamond radiator gives rise to preferential planes of momentum transfer. This gives the electrons a higher probability of interacting with the regular lattice planes of the diamond [84, 85] which shows as an enhancement in the cross section of the amorphous spectrum, an example is shown in Figure 4.4 (middle). The cross section of a coherent bremsstrahlung spectrum can be expressed as

$$\sigma_{diamond} = \sigma_{in} + \sigma_{co} \quad (4.2)$$

where  $\sigma_{in}$  and  $\sigma_{co}$  are the incoherent (unpolarised) and coherent (polarised) contributions respectively. An enhancement in the cross section from the coherent bremsstrahlung can be defined as

$$Enh = \frac{\sigma_{diamond}}{\sigma_{in}} \quad (4.3)$$

The coherent bremsstrahlung spectrum from the diamond radiator is divided by the incoherent spectrum to subtract unpolarised contributions. The resulting plot is termed an enhancement plot. A plot such as this is fit in order to extract the degree of linear polarisation, further discussion on this can be found in Section 5.3.

The photons in the coherent part of the bremsstrahlung spectrum have a high degree of linear polarisation. The high degree of polarisation is due to the momentum transfer with the directional field of the lattice planes. The electric vectors of the nuclei in the diamond radiator sum to a direction perpendicular to the lattice planes.

Diamond is used as the radiator to produce coherent bremsstrahlung due to its rigid lattice structure. Compared to other potential materials, it has a high Debye-Waller factor. Consequently, there is little influence of thermal fluctuations on the produced coherent bremsstrahlung photons [86].

The diamond orientation can be fine tuned using the goniometer in order to change the energy at which the main coherent peak presents itself. The azimuthal orientation of the diamond sets the angle of the polarisation plane and the angle between the diamond and beam (1 - 5 mrad) sets the position of the coherent peak in the photon energy. A precision goniometer is essential to achieve the level of tolerance required.

## 4.4 Goniometer

The goniometer (Figure 4.5) houses the radiator wheel in an evacuated chamber. The goniometer is situated at the start of the beam line in the A2 hall and includes the diamond radiator and copper radiator which produce a linearly polarised amorphous photon beam respectively.



Figure 4.5: View of the Goniometer through the camera mounted inside it. The centre slot is the diamond radiator.

The goniometer has five axes which can move in order to change the radiator in the beam line. The precise angle of the radiator with respect to the beam line can also be remotely altered in order to change the alignment of the diamond.

### 4.4.1 Stonehenge Technique

To accurately adjust the linear polarisation orientation the goniometer must be calibrated to determine the relationship between the crystal lattice, the lab frame

and the relative frame of the goniometer wheel. The Stonehenge technique [87] was developed in order to accurately determine these relationships and has been successfully used in several facilities including MAMI in Mainz, CLAS at Jefferson Laboratory, MAXLab in Lund and CB-ELSA in Bonn.

The Stonehenge technique is used to align a diamond radiator with respect to an incident electron beam, in order to produce the linearly polarised photon beam through coherent bremsstrahlung. It builds upon the work of Lohman [84]. The technique, outlined by Lohman et al., requires an initial alignment of the crystal lattice to the electron beam and the crystal to the lab frame to less than  $1^\circ$  for energies up to 1557 MeV. It requires many iterative scans before a suitable level of accuracy is achieved.

The Stonehenge technique only requires the tagged photon spectrometer (Section 4.6) when performing a scan and is significantly faster than the method used by Lohman et al. The scan is done by adjusting the goniometer about a cone. The plot obtained from this scan is a radial distribution of the coherent enhancement spectrum. The center of the cone is adjusted with each iteration until the Stonehenge distribution obtained is symmetrical as shown in Figure 4.6 (Right).

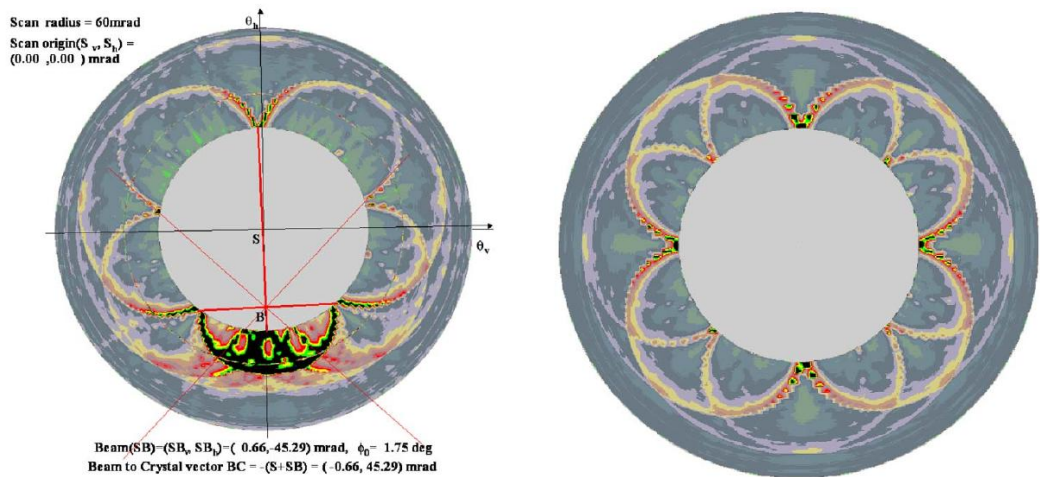


Figure 4.6: Radial distributions of goniometer scans. Left: Stonehenge distribution prior to alignment adjustments. Right: Stonehenge distribution after alignment. Polarisation planes at  $\pm 45^\circ$ . Taken from reference [87]

The energy of the linearly polarised photons can be controlled with orientation of

the crystal lattice with respect to the incident electron beam. The coherent peak is the main peak observed in the coherent bremsstrahlung enhancement spectrum and contains photons with the highest degree of polarisation. It is produced by scattering electrons from  $[0,2,2]$  and  $[0,2,\bar{2}]$  planes of the crystal which can be separated from contributions from higher order lattice planes. Bremsstrahlung produced from interaction with these reciprocal lattice planes produces linearly polarised photons, with linear polarisation orientated perpendicular to the lattice plane. The orientation of the linear polarisation of the photons can be controlled accurately with azimuthal rotation about the centre of the cone once calibrated.

## 4.5 Collimator

Collimation of the photons (Section 4.5) is used to increase the coherent contribution relative to incoherent measured in the bremsstrahlung spectrum. The increase occurs due to the difference in the angular distributions of incoherent and coherent bremsstrahlung. Coherent bremsstrahlung produces photons with a higher degree of polarisation at forward angles, where incoherent bremsstrahlung has a wider angular distribution. Reducing the collimation diameter increases the ratio of coherent to incoherent photons but at the cost of the flux incident on the target. A compromise is therefore required in order to reach an optimum balance between coherent contributions and flux on the target. A 2 mm diameter collimator was used during the experiment positioned 2.5 m downstream of the radiator.

## 4.6 Glasgow Tagged Photon Spectrometer

The Glasgow tagged-photon spectrometer (Figure 4.7) was used to measure the energy of photons by detecting electrons, that have undergone bremsstrahlung, in coincidence with a signal in the Crystal Ball detector systems.

The Glasgow tagged-photon spectrometer consists of a focal plane detector (FPD), and a large dipole magnet. The FPD covers a range of 5 - 95% of the initial electron beam energy provided by MAMI with the resolution of the focal plane varying between 2 - 3 MeV [88]. The FPD itself consists of 353 EJ-204 plastic scintillators, overlapping by half their length, allowing an event to be defined as a coincident hit between two adjacent scintillators. The overlapping scintillators give 352 separate coincidence tagger channels.

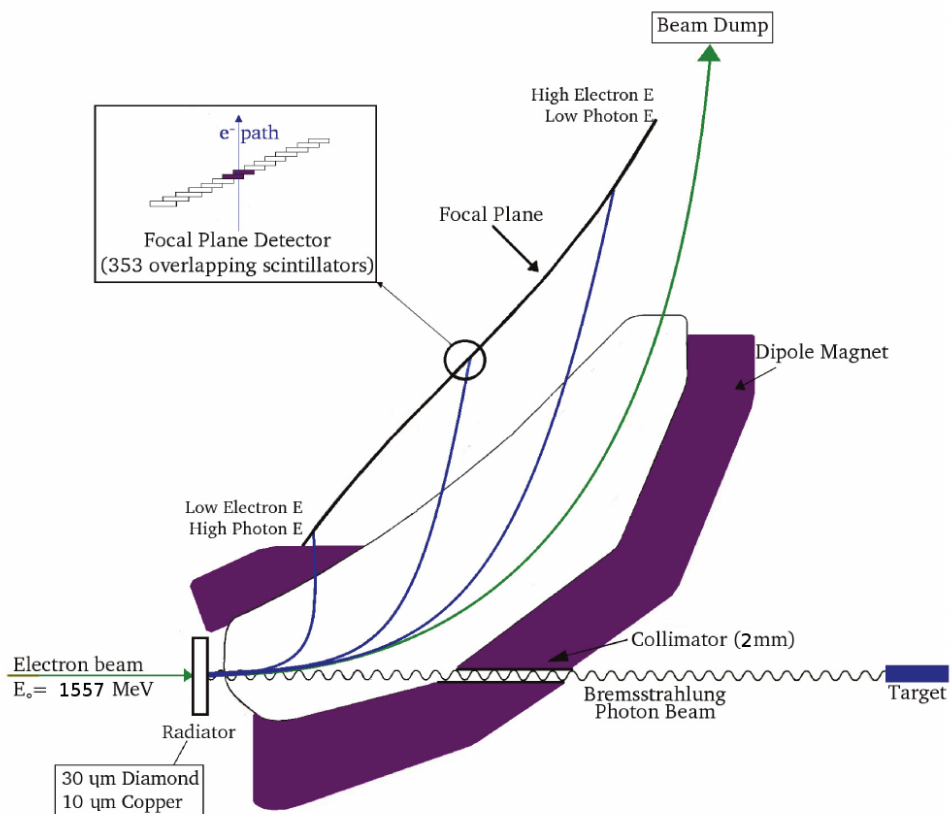


Figure 4.7: Schematic of the Photon Tagger. Taken from [89].

The bremsstrahlung photons have energy equal to the difference in energy between the incoming ( $E_0$ ) and outgoing ( $E_F$ ) electrons, given by Equation 4.1.

The electrons, having passed through the radiator, are bent away from the initial beam trajectory by a large dipole magnet. Electrons with the maximum beam energy ( $E_0$ ) will be deposited in the beam dump having been bent by the dipole magnet. Electrons that undergo bremsstrahlung in the radiator will be bent further, on to the focal plane, due to their lower momentum. The position of the incident

electron along the focal plane gives a measure of the energy of the bremsstrahlung photons through Equation 4.1. The position of the focal plane scintillator defines the energy assigned to the electron for the event. This was determined through calculations based on the field map and dedicated calibration beamtimes (Section `subsec:photon_tagger_calib`).

## 4.7 Detector Setup

The detector set up, shown in Figure 4.8, consists of the Crystal Ball (CB) detector (Section 4.7.1), the Particle Identification Detector (PID) (Section 4.7.2), the Frozen Spin Target (Section 4.7.4) and the TAPS detector (Section 4.7.3).

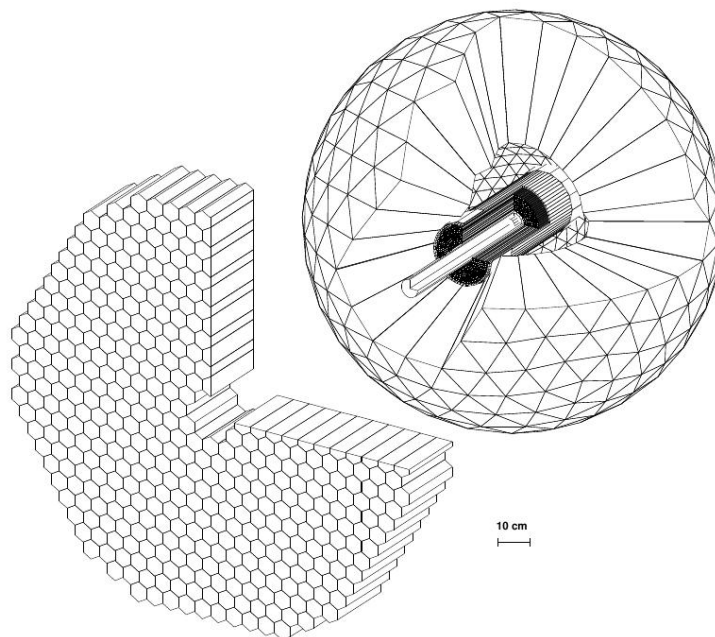


Figure 4.8: Overview of the TAPS-CB set up [90]. The Frozen Spin Target is surrounded by the PID which sits centrally in the Crystal Ball detector. The TAPS detector covers the forward angles and increases the angular coverage from around 93% to 97%.

### 4.7.1 Crystal Ball

The Crystal Ball was built at Stanford Linear ACcelerator (SLAC) and used in  $J/\Psi$  measurements before moving to DESY where it was used in b-quark physics. The CB [91, 92, 90, 93] (Figure 4.9) is currently the central detector of A2 and surrounds the target, particle identification detector (PID) [92] and wire chambers [90]. The CB is a spherical shell of 672 thallium doped sodium iodide (NaI(Tl)) crystals configured in an icosahedral shape, shown in Figure 4.10. Each of these faces is divided into four minor triangles consisting of nine NaI(Tl) crystals (Figure 4.10).

The detector has an opening at either end, to allow the photon beam to enter and leave. Forward angles are covered by the TAPS forward wall, Figure 4.8 (see Section 4.7.3 for TAPS). The CB has a large angular acceptance of around 93% of  $4\pi$ , covering the full  $2\pi$  azimuthal range and polar angles  $20^\circ < \theta < 160^\circ$ . The acceptance increases to 97% when including the TAPS forward wall. The CB is used to reconstruct the kinematics of the reaction products using the NaI(Tl) hit (cluster) information in coincidence with the Tagger and other detectors.

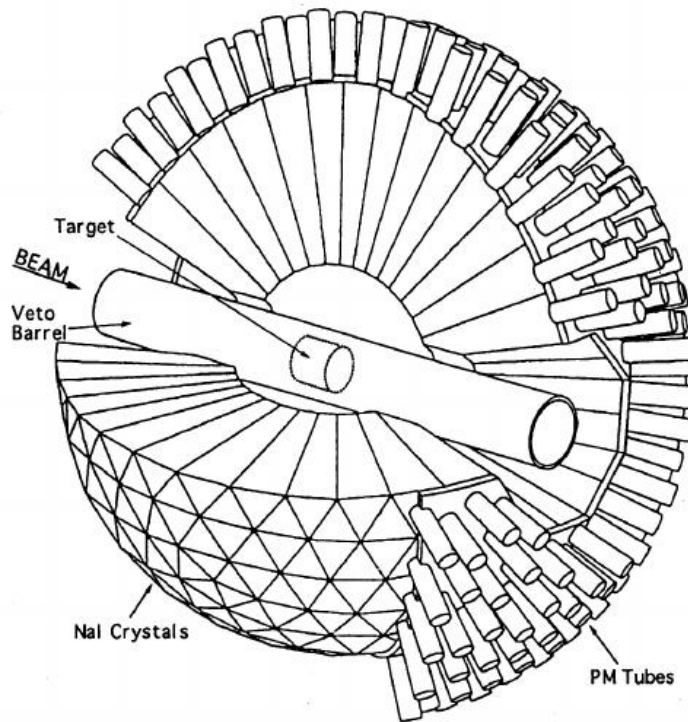


Figure 4.9: Schematic of the Crystal Ball showing target position in the center and the surrounding NaI(Tl) and photomultiplier tube (PMT) pairs. The Veto Barrel was originally in the SLAC experiment but is no longer a part of the set up. [90].

The NaI(Tl) are coupled with PMTs and separated by an air gap and glass sheet totalling 5 mm. The PMTs detect photons from the scintillation processes which occur in the NaI(Tl) elements. When a charged particle interacts with a NaI crystal it causes valence electrons to become excited. These excited electrons decay to their ground state, releasing a low energy photon, which may be detected in the PMT.

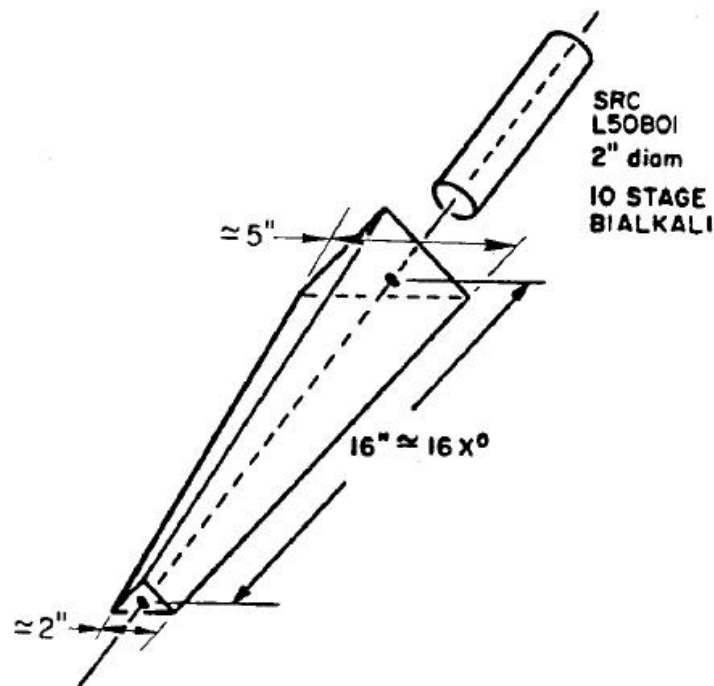


Figure 4.10: Schematic of one of the 672 NaI crystals which form the crystal ball [90].

The scintillation process happens via charged particles in both cases. In the case of the photon it first converts into an  $e^+e^-$  pair (i.e. charged particles) when a photon is incident on the NaI(Tl), the density of the crystal causes the photon to convert into an electron-positron pair. This pair can undergo bremsstrahlung, emitting further photons, causing an electromagnetic shower. In general the shower can spread to many crystals causing a cluster of hits. The energy distribution in the cluster allows determination of the initial photon kinematics.

### 4.7.2 PID

The Particle Identification Detector (PID) consists of 24 thin plastic scintillator strips in a cylindrical configuration and surrounds the target within the CB. The signals in the PID are read out via PMTs attached to the downstream end of the scintillator. When a charged particle passes through one of these strips it deposits a small amount of energy ( $\Delta E$ ), before depositing the rest ( $E$ ) in the CB or TAPS

detectors.

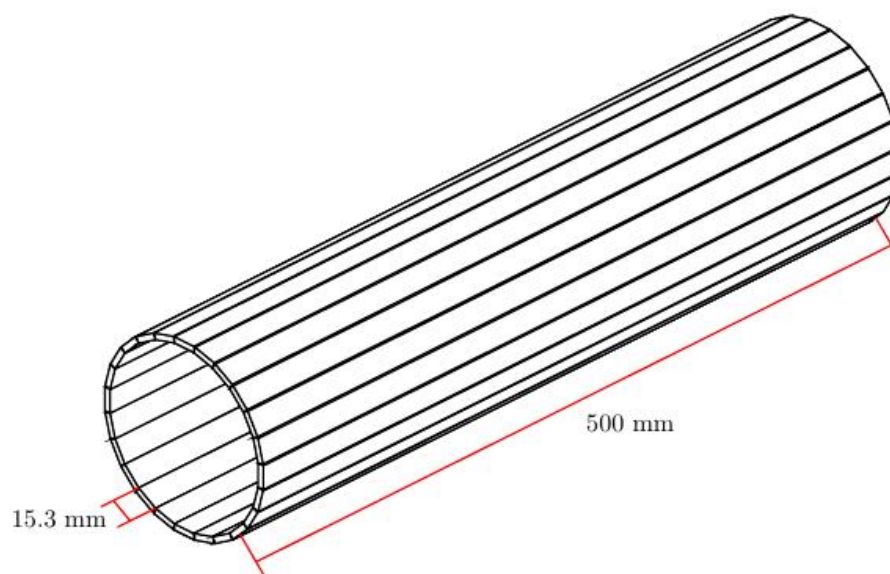


Figure 4.11: PID detector with 24 plastic scintillators in a cylindrical configuration. The PID sits in the centre of the CB detector and surrounds the target, providing energy and angular information on charged particles.

The amount of energy deposited is related to the mass of the particle. The PID, along with the CB and TAPS, can be used to better identify and differentiate particles through  $E\Delta E$  plots. In this analysis it was decided to omit the PID information as sufficient reaction identification was provided through kinematic constraints, while the PID operation was erratic during the beamtime.

### 4.7.3 TAPS

The CB has no acceptance at forward angles for  $\theta < 20$ , however this was recovered by use of the Two Arm Photon Spectrometer (TAPS). TAPS was positioned 1.75 m down the beamline from the target center. It consists of 384 individual hexagonal  $\text{BaF}_2$  crystals which are 22.5 cm in length and 5.9 cm in diameter. The TAPS detector has an angular resolution of around  $0.7^\circ$  and a timing resolution of 0.5 ns.

72 smaller lead tungstate ( $\text{PbWO}_4$ ) crystals, 20 cm in length, were installed in the inner rings of the TAPS detector to withstand the higher rates from the photon beam at small forward angles. The configuration of the  $\text{PbWO}_4$  crystals is such that the combination of four gives the same geometry of a single  $\text{BaF}_2$  crystal.

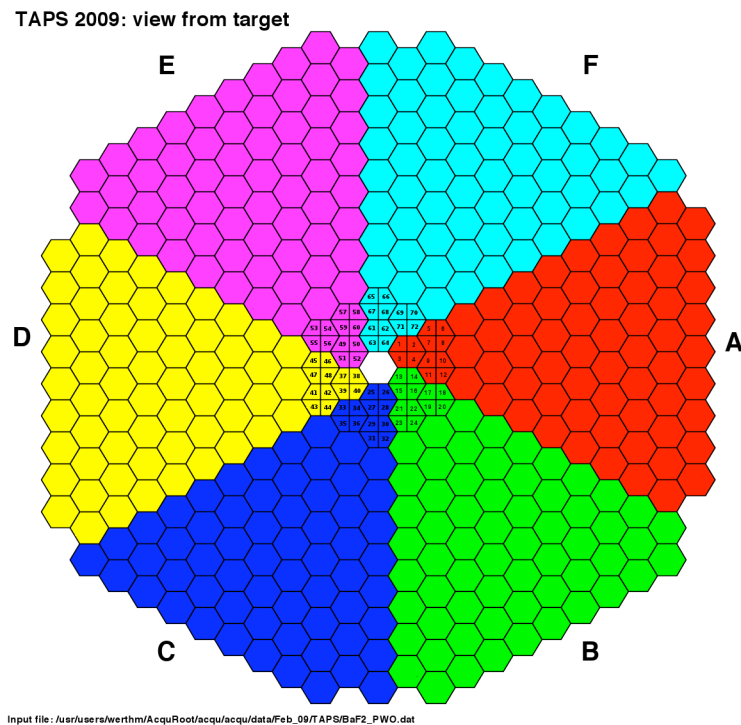


Figure 4.12: TAPS schematic as seen from the target.

With the addition of the veto elements, a 5mm thick plastic scintillator wall at the front of each individual detector, it is possible to identify particles similarly to the PID. If the particle is charged then it will deposit a small amount of energy in the veto element with the rest of the energy deposited in the corresponding  $\text{BaF}_2$  crystal.

The hits can be directly correlated due to the coupling of a PMT to the individual BaF<sub>2</sub> crystals.

#### 4.7.4 Frozen Spin Target

The frozen spin target [91, 94] was designed to retain the high angular acceptance of the detector systems. The main restriction in designing the structure to hold and cool the target was the inner diameter of the PID detector which measured 104 mm. The refrigeration system (Figure 4.15) was specially designed for this purpose and built in cooperation with the Joint Institute for Nuclear Research (JINR) in Dubna, Russia. The target material was butanol (C<sub>4</sub>H<sub>9</sub>OH) which was doped with paramagnetic radicals, which allowed for polarisation transfer to the free protons of the butanol. The frozen spin target is achieved using Dynamic Nuclear Polarisation (DNP), which consists of polarising a target at a cold temperature using microwave radiation. After, the polarisation is maintained using a holding magnetic field.



Figure 4.13: Solenoid coil used for longitudinal polarisation of the butanol target.

The DNP process is done in two steps. The initial process uses the <sup>3</sup>He/<sup>4</sup>He dilution refrigerator (Figure 4.15) to cool the target material to 25 mK in a highly uniform magnetic field of 2.5 T using a solenoidal coil surrounding the target (Figure 4.13). Once cooled, the material was irradiated with 70 GHz microwaves, close to the

electron spin frequency, which resulted in polarisations of the protons parallel to the magnetic field. Using the solenoidal coil produces a longitudinal polarisation of the target (either  $\pm z$  along the photon beam direction). This provided a longitudinal polarisation degree of up to 85%, but also increased the target temperature from 25 mK to 0.2 K.

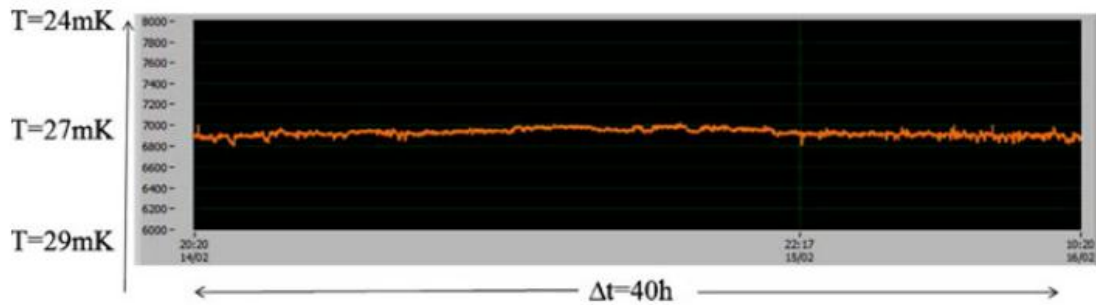


Figure 4.14: Typical target temperature stability over a single day. Stability of the target temperature is shown to be  $\pm 0.2$  mK.

Once the target was polarised the microwaves were switched off and the temperature decreased to the original 25 mK. The decrease in temperature increases the relaxation time of the polarisation. The stability of the temperature during operation is important to manage the degree of polarisation and systematics. The stability of the temperature was measured and shown to be very stable over a single day with a fluctuation of  $\pm 0.2$  mK as shown in Figure 4.14. The butanol target had a relaxation time of around 1500 hours. The polarisation of the target is maintained by a holding field coil which provides a magnetic field of 0.45 T during operation. A Nucleon Magnetic Resonance (NMR) system was used to measure the degree of polarisation during operation which consists of a serial resonance circuit with a coil surrounding, or inside, the target. A change in the polarisation of the target induces a measurable change in voltage across the circuit.

A disadvantage of the system used is the necessity to move the detectors and the target structure in order to re-polarise the target material. This may create systematic effects between different run periods such as changes to the electromagnetic noise environment. Systematic effects are investigated in Section 8.5.

The target was positioned 8.25 m after collimation, sitting centrally within the CB

detector. The target cell was 2 cm in radius and 2 cm in length. The number of protons in butanol, for the target cell dimensions, is  $9.181 \times 10^{22} \text{ cm}^{-2}$  at a temperature of 25 mK and at a pressure of 1080 mbar [95]. Butanol contains both carbon and oxygen which contributes to background events due to quasi-free interactions with bound protons. The butanol target contains  $3.672 \times 10^{22} \text{ cm}^{-2}$  and  $9.181 \times 10^{21} \text{ cm}^{-2}$  for carbon and oxygen respectively. The number of free protons in the butanol target is  $8.62 \times 10^{22} \text{ cm}^{-2}$  [90]. Data was taken using a carbon target in order to account for these background contributions.

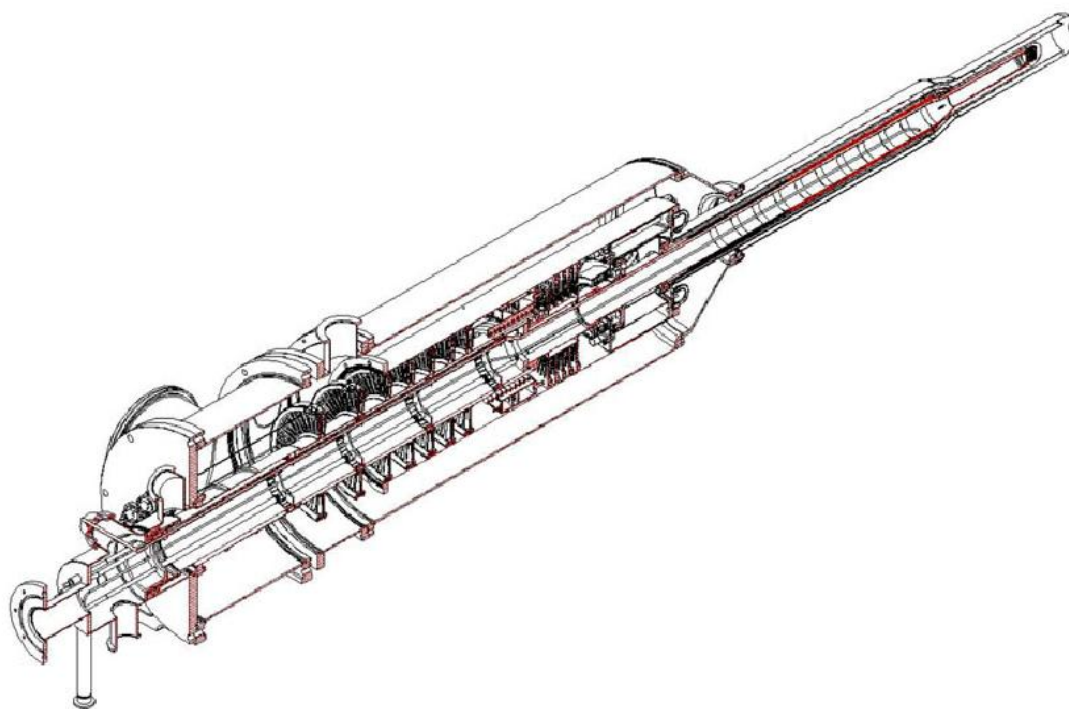


Figure 4.15: Top: Photo of the  $^3\text{He}/^4\text{He}$  dilution refrigerator for cooling and maintaining the polarisation of the butanol target. The solenoid coil can be seen at the end of the refrigerator arm on the left. Bottom: Schematic of the  $^3\text{He}/^4\text{He}$  dilution refrigerator 3D cross section [94].

## 4.8 Trigger

The trigger is a combination of two conditions which both need to be met simultaneously in order for an event to be accepted or rejected. The first condition takes the list of hits, with a threshold energy deposit over 2 MeV, and sorts them according to energy. The list is then used to search for clusters, marking the hit with the maximum energy as the logical center for the cluster, providing the time for that cluster. The neighbouring 16 hits are checked and are added to the cluster, and removed from the list of hits, if their energy meets the threshold condition. Only the neighbouring 16 elements are checked because almost all of the deposited energy of a photon is contained within these elements. Once all the neighbours have been checked, the cluster energy is calculated by taking the sum of all the individual hit energies that constitute that cluster.

The second condition is the sum of the energy detected from all cluster hits in the CB (and TAPS), known as the CB energy sum ( $E_{sum}$ ). The kinetic energy threshold was set to 80 MeV per cluster, meaning events where the  $E_{sum}$  was lower than this were rejected, reducing the background noise that would be included at lower thresholds. Setting these two trigger conditions is a compromise between the downtime in the data acquisition system (where the previous event is being processed) and high event rates.

A multiplicity trigger is also set which has the purpose of approximating the number of detected particles. This was set to M3- which means events with three or fewer hits were accepted, whereas events with hits greater than three did not meet the conditions of the trigger and were rejected. This condition was set to better select events from the  $\pi^0 \rightarrow \gamma\gamma$  decay.

## 4.9 Simulation

A Monte Carlo simulation of the A2 detector set up was used in this work [96]. It was modelled using Geant4 libraries [97, 98]. The simulation aims to model the set-up precisely and uses physics libraries to model the scintillation processes in the detectors.

The main components modelled in the simulation were the CB and TAPS detectors, shown in Figure 4.8. The target and PID were also included as part of the simulation. The model allows other detectors to be added to the simulation.

The simulation was given events from particular reaction channels using an external event generator AcquMC [99]. The events were recorded in the same way as real data. The  $\gamma p \rightarrow p\pi^0$  reaction channel was simulated in this work. This reaction channel was used to model the desired signal events included in the  $s\mathcal{P}$ lot method (Section 6.4). The shapes of the missing mass, coplanarity and opening angle of detector and reconstructed proton were used as a Probability Density Function (PDF) to fit experimental data.

# Chapter 5

## Calibration

In order to extract meaningful physics information from the data, the detectors were calibrated prior to using the data. The detectors provide position, timing and energy information through knowledge of the position of detector elements, and the TDC and ADC readouts (time- and analogue-to-digital converters). Once calibrated, the information from the various detector systems can be used to identify specific reaction channels and exclude background. The detectors discussed in this chapter, are the Photon Tagger, CB, PID, TAPS and TAPS Vetos.

### 5.1 Energy calibration

Energy calibrations were performed to correctly measure the energy deposits in the different detector elements. The energy was measured using analogue-to-digital converters, otherwise known as charge-to-digital converters (QDCs), which integrate the electrical signals. This section discusses the various methods used to perform energy calibrations on each of the detectors.

### 5.1.1 Photon Tagger

The tagger was used to measure the energy of bremsstrahlung photons that passed collimation as well as correlate hits with the other detectors. It inferred the energy of the electrons through the position of a hit along the focal plane detector, defined as a coincidence of two adjacent detector elements. The energy of the photons was then calculated using the difference in energy between the initial electron and the electron incident on the focal plane. The tagger dipole magnet was set up to direct the electrons with the full MAMI beam energy into a beam dump past the focal plane of the Tagger [100].

The position-to-energy calibration along the focal plane was performed in a dedicated beamtime by bending electrons of a known energy directly onto the tagger elements, using a low intensity electron beam. No radiator was in place so that the electrons incident on the focal plane had the initial measured energy provided by MAMI. Varying the magnetic field strength provides several measurements of hits along the focal plane for a particular MAMI beam energy. This calibration process allowed a relationship between the tagger channel and electron energies to be calculated and extrapolated along the entire range of the focal plane, assuming a uniform magnetic field.

### 5.1.2 Crystal Ball

The crystal ball required two forms of calibration, low and high energy calibrations. The low energy calibration was made to set the HV values prior to data taking. The high energy calibration aligned the calibration parameters of the individual crystals to improve the overall energy resolution.

#### Low energy calibration

An  $^{241}\text{Am}^9\text{Be}$  source was used to calibrate the individual detector elements, producing a monochromatic decay photon at 4.438 MeV. The gains of the photomultiplier

tubes (PMTs) were adjusted by altering the high voltage across the PMT until the signal peak from the  $^{241}\text{Am}^9\text{Be}$  source was positioned at the same ADC channel for all elements, as seen in Figure 5.1. The relationship between the ADC gains and the deposited energy can be expressed as

$$E_{dep} = \text{gain} \cdot (\text{ch} - \text{ped}) \quad (5.1)$$

where  $\text{ch}$  is the measured ADC digital channel and  $\text{ped}$  is the pedestal channel of the ADC which represents the base signal (channel of zero energy) from which the energy is integrated.

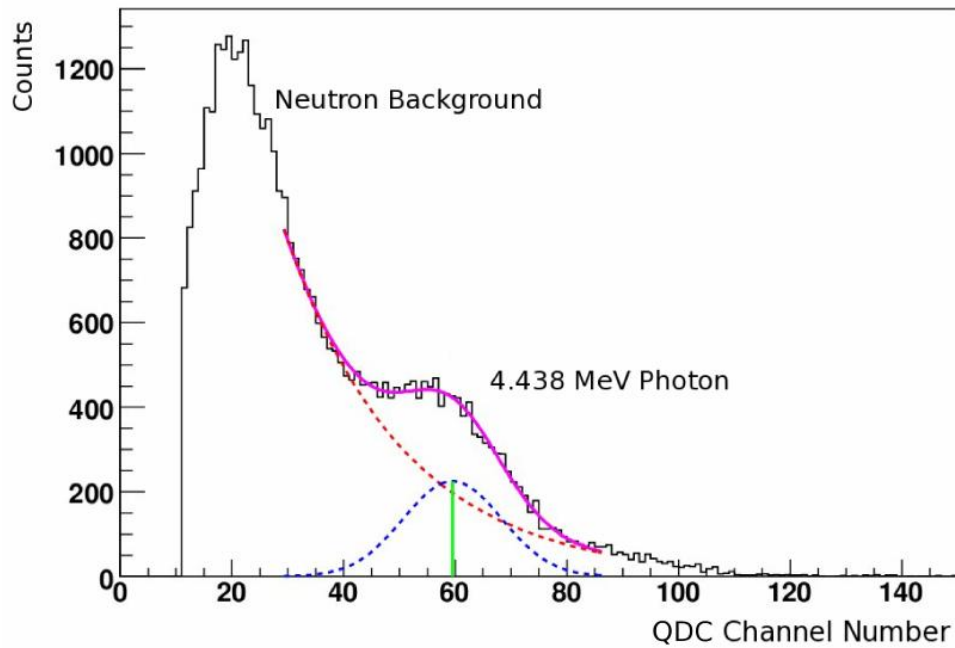


Figure 5.1: Energy spectrum from one NaI(Tl) crystal using an  $^{241}\text{Am}^9\text{Be}$  source. Purple line: total fit to the data. Dashed red line: polynomial to fit the background of the data. Dashed blue line: Gaussian curve used to fit the signal peak. Green line: mean position of the Gaussian fit. Taken from [101].

### High energy calibration

As the experiment ran with energies of up to two orders of magnitude higher than that seen in the low energy calibration, it was not sensible to extrapolate the low

energy results up to high energies. A high energy calibration was performed instead by adjusting the ADC gains while looking at the peak of the  $\pi^0$  in the invariant mass spectrum of two photons. The invariant mass of two photons is given by

$$m_{\gamma\gamma} = \sqrt{(E_{\gamma 1} + E_{\gamma 2})^2 - (\vec{p}_{\gamma 1} + \vec{p}_{\gamma 2})^2} \quad (5.2)$$

This can be expressed in terms of cluster elements to express the mean position of the  $\pi^0$  peak in the spectrum, expressed as

$$\langle m_{\pi^0, i} \rangle = \sqrt{2\langle E_{\pi^0, i} \rangle \langle E_{\pi^0, o} \rangle (1 - \cos \langle \psi_{\pi^0, io} \rangle)} \quad (5.3)$$

where  $\langle m_{\pi^0, i} \rangle$  is the mean position of the  $\pi^0$  peak with central element  $i$ ,  $\langle E_{\pi^0, i} \rangle$  and  $\langle E_{\pi^0, o} \rangle$  are the mean photon energies of element  $i$  and the other cluster respectively and  $\langle \psi_{\pi^0, io} \rangle$  is the mean opening angle between the photon detected in element  $i$  and the photons detected in the other cluster.

The aim is to adjust the conversion gains of the ADCs such that the mean invariant mass equals that of the  $\pi^0$  meson

$$\langle m_{\pi^0, i} \rangle = \sqrt{2\langle E_{\pi^0, i} \rangle \langle E_{\pi^0, o} \rangle (1 - \cos \langle \psi_{\pi^0, io} \rangle)} \equiv m_{\pi^0} \quad (5.4)$$

An expression for the new gain was expressed in terms of the old gain, given as

$$gain_{new} = gain_{old} \cdot \frac{m_{\pi^0}^2}{\langle m_{\pi^0, i}^2 \rangle} \quad (5.5)$$

The gains were adjusted iteratively due to  $\langle E_{\pi^0, i} \rangle$  containing contributions from surrounding elements, and due to the change of gain in one element effecting the calibration of another through  $\langle E_{\pi^0, o} \rangle$  and  $\langle \psi_{\pi^0, io} \rangle$ . A typical spectrum of all summed elements after a high energy calibration is performed is shown in Figure 5.2.

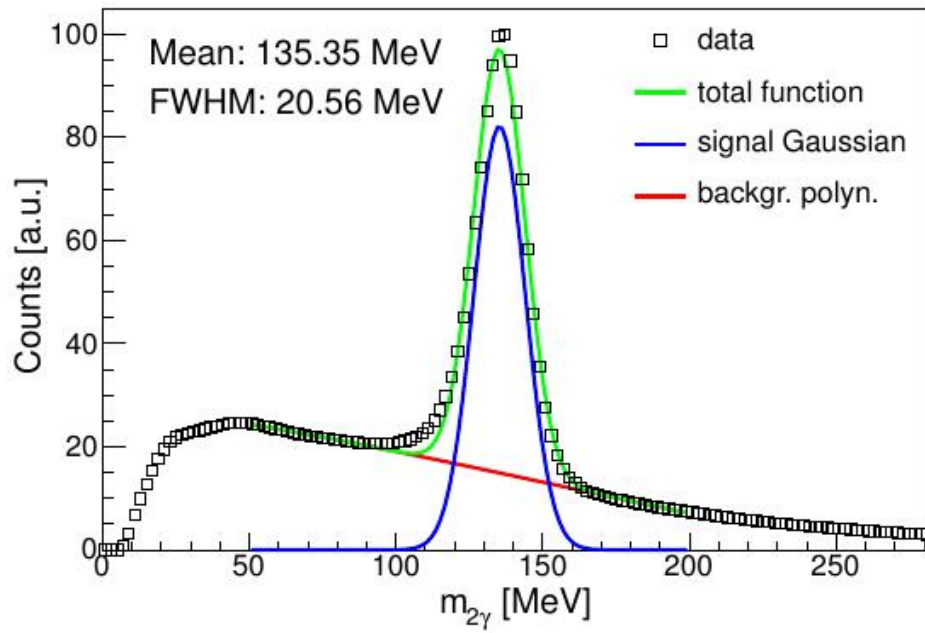


Figure 5.2: Two photon invariant mass for the CB showing the peak of the  $\pi^0$ . Black square: data from the sum of all CB elements. Green line: total fit to data. Blue line: Gaussian curve used for signal. Red line: background polynomial. Taken from [102].

### 5.1.3 PID

The PID elements are not particularly thick, which results in only a small amount of energy deposited from charged particles. Distributions of energy deposited in the PID against the energy deposited in the CB were made for data and simulation. Projecting these plots allowed the proton peak to be fitted using a Gaussian and the values obtained for simulation were plotted against the values obtained for data. The comparison of the Gaussian fit values was fitted with a linear function, from which the pedestal value and gain value could be calculated for each PID element (Figure 5.3).

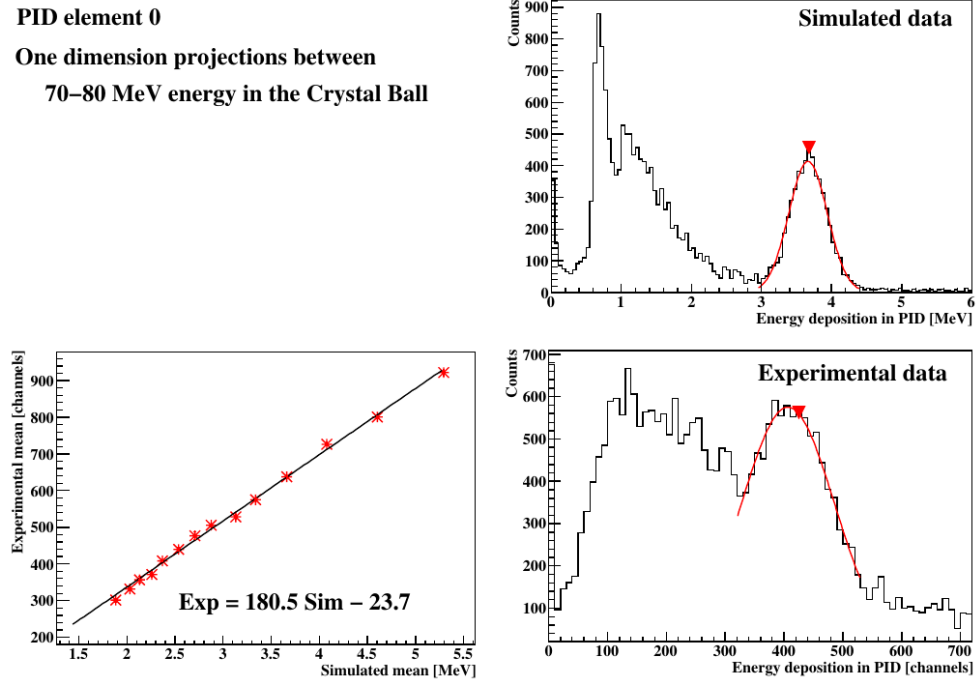


Figure 5.3: PID energy calibration. Top and bottom right: energy depositions in the PID for simulation and data respectively. The peak due to energy deposition from the proton was identified by a Gaussian function. Bottom left: mean value of simulated and data gaussian fits plotted against each other. A linear fit was used to calibrate the gains and pedestal value of the PID. Taken from [103].

### 5.1.4 TAPS

As for the CB two calibrations are applied to the TAPS detector, a low and a high energy calibration. The low energy calibration differs from the CB calibration and uses cosmic radiation instead of a source.

#### Low Energy Calibration

A low energy calibration was performed to normalise the individual elements to one another before running an experiment and to obtain a first rough calibration. The TAPS elements are positioned horizontally, unlike the CB, which has the benefit of being able to use cosmic radiation. The cosmic radiation used for this calibration was muon radiation with the same average path length for all TAPS elements. The

mean deposited energy was found to be around 38MeV [[102]].

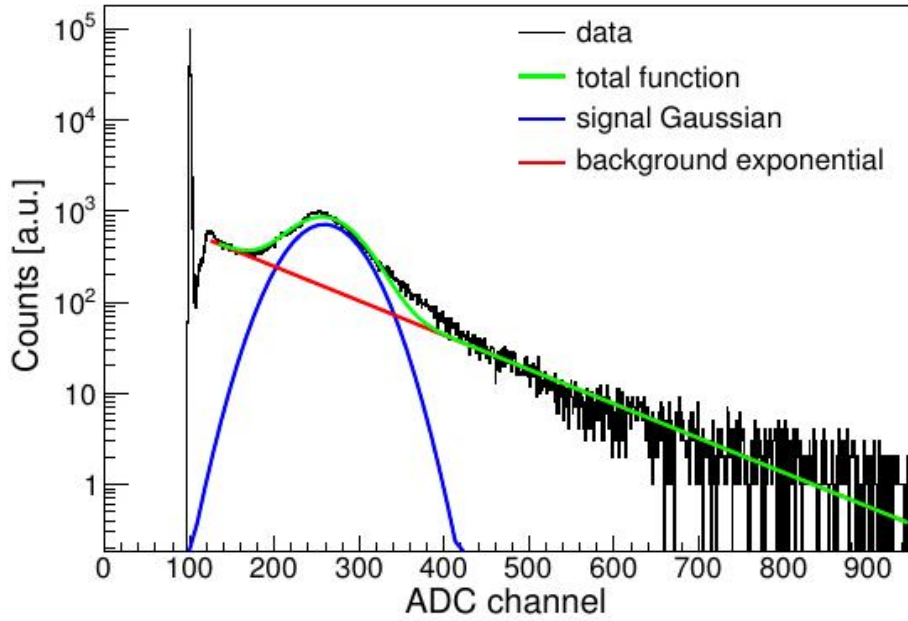


Figure 5.4: Typical ADC spectrum from cosmic radiation in single BaF<sub>2</sub> crystal. Taken from [102].

The gains can be calculated from knowledge of the pedestal position and the ADC channel corresponding to the mean deposited energy as described in Equation 5.1 (Figure 5.4).

### High Energy Calibration

The high energy calibration is similar to that of the CB in that the invariant mass of two photon pairs is measured and the gains are iteratively altered until the peak matches that of the accepted  $\pi^0$  mass (Figure 5.5). Either both photons are located in TAPS or at least one can be located in TAPS and the other in the CB.

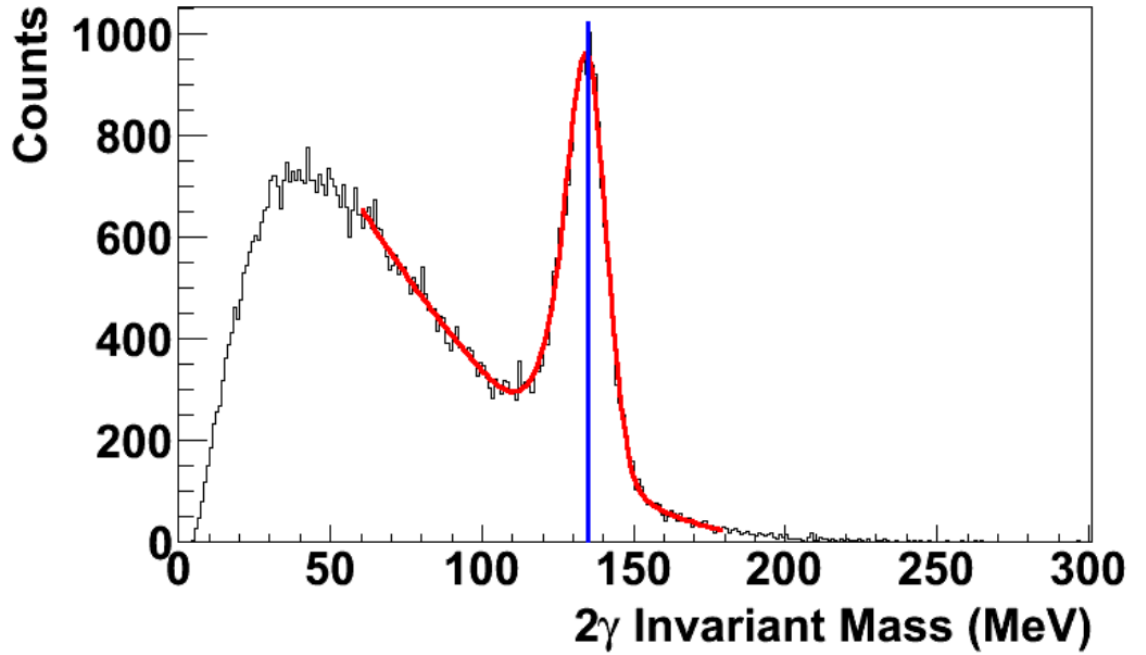


Figure 5.5: Two photon invariant mass of summed TAPS elements showing peak at the  $\pi^0$  meson mass. Taken from [104]

## 5.2 Time calibration

A precise timing calibration is needed to accurately measure coincident hits between detectors and to subtract background. Each detector element has an individual time recorded using their corresponding TDCs. The time calibration is performed to determine and align the coincidence peaks for each detector element. The relationship between the time, gain and TDC channels can be expressed as:

$$time = gain \cdot (ch - offset) \quad (5.6)$$

In the following section the PID azimuthal calibration and timing calibrations of the tagger, CB, PID, TAPS are discussed.

### 5.2.1 Tagger

To correlate hits from the tagger to events in the other detectors a coincidence time is required. The alignment of the timing coincidence between all tagger elements is essential. The data taken for the alignment of the tagger time was at a significantly lower rate than the experimental runs (around 10 kHz compared to GHz rates). A Pb glass scintillator, positioned at the end of the beamline past the TAPS detector, was used to make coincidence time peak clearer in these measurements.

The tagger time is measured using TDCs with an individual fixed gain of 0.117 ns/channel with no need for a gain calibration, only the timing offsets require calculation.

The offset is determined by plotting the TDC spectrum for each tagger channel and fitting a Gaussian to the peak to determine the mean TDC channel. A new offset is determined to align the relative timing of all the TDCs to an arbitrary position, usually zero, using Equation 5.6. Figure 5.6 shows the resulting coincidence time with the Pb glass detector versus focal plane element after the calibration.

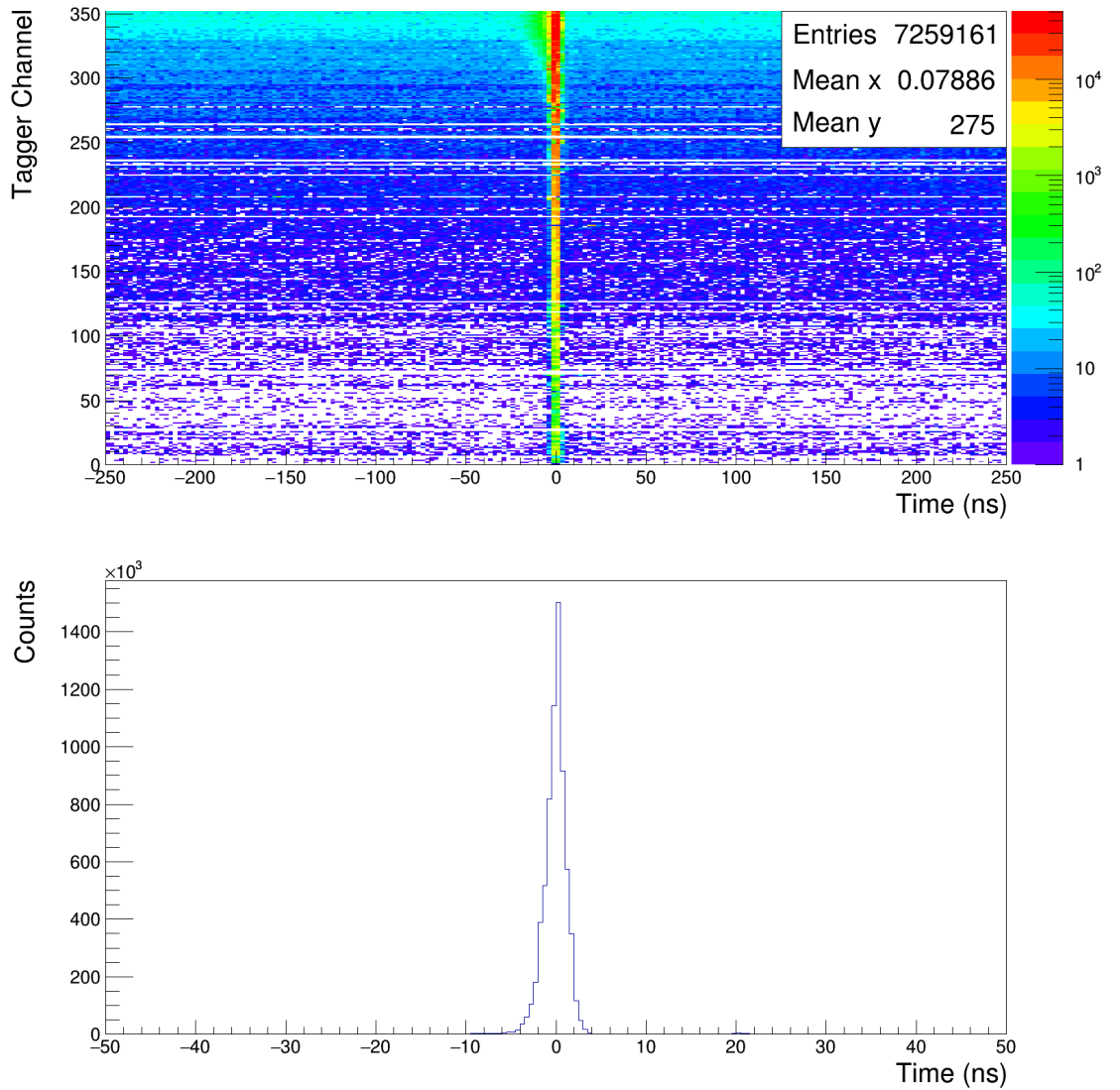


Figure 5.6: Top: Calibrated coincidence time plotted for all tagger channels. Bottom: Tagger coincidence time with Pb glass.

### 5.2.2 CB

The CB TDCs operate with a fixed gain of 0.117 ns/channel meaning only the timing offsets required calibration. The new offsets were determined by fitting Gaussians to the peak in the TDC time distribution for each element to get a mean value of the current position and by using

$$Offset_{new} = Offset_{old} \cdot \frac{Mean_{Guas}}{gain} \quad (5.7)$$

The new offset was applied to each detector element which aligned their relative times to an arbitrary value, usually zero.

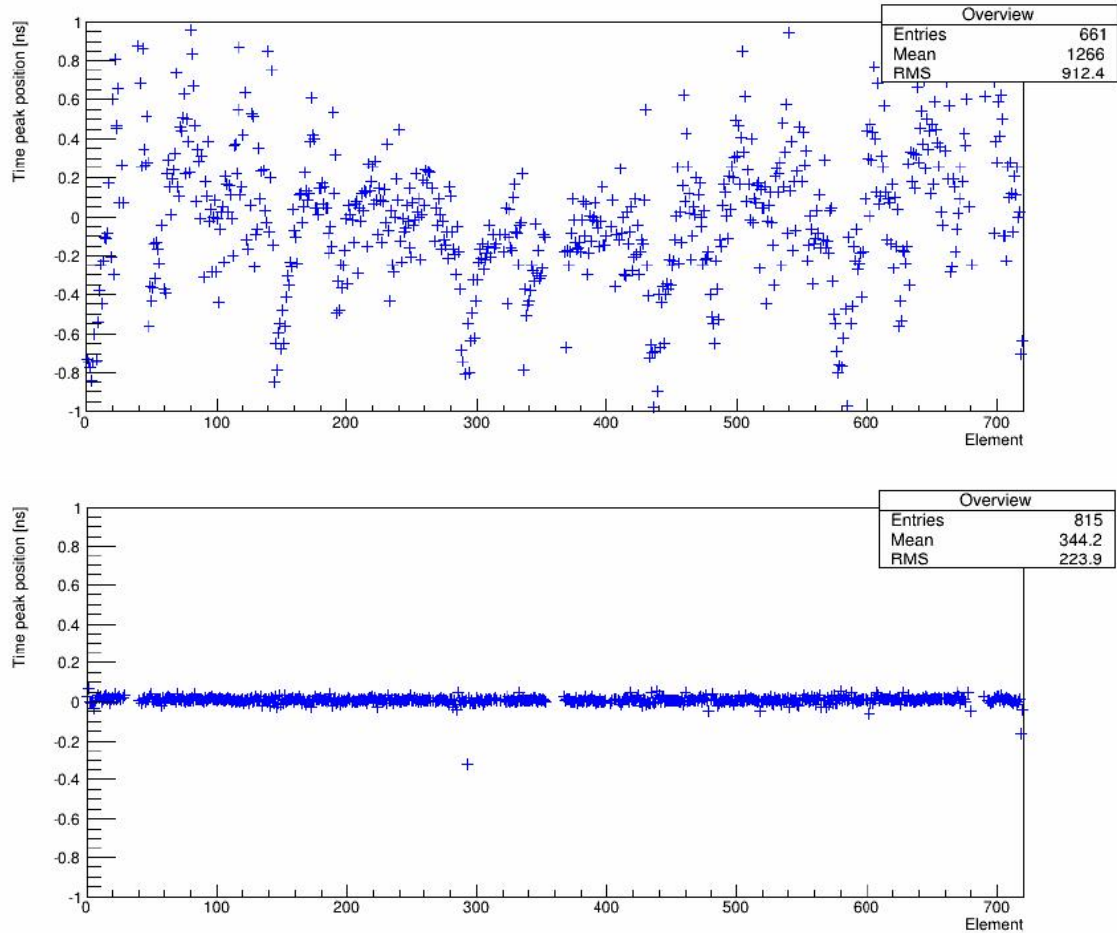


Figure 5.7: Top: Uncalibrated time offsets plotted for all CB elements. Bottom: Calibrated time offsets plotted for all CB elements. Provided by collaborators at Bonn, taken from [105]

### 5.2.3 CB Time Walk

The CB suffers from a slow rise time, resulting in an energy dependence on the time which needs to be accounted for using a time walk correction. The time walk correction was performed through a fit to the distribution of the time against energy for each detector element (Figure 5.8). The events from  $\pi^0$  photoproduction were used to suppress background contributions. These were selected using cuts on the two photon invariant mass and the  $\pi^0$  missing mass. The relative time between the

CB and the tagger was used to calculate the time for each detector element of the two photon clusters. The equation used to fit this distribution is given as

$$t(E) = a + \frac{b}{(E + c)^d} \quad (5.8)$$

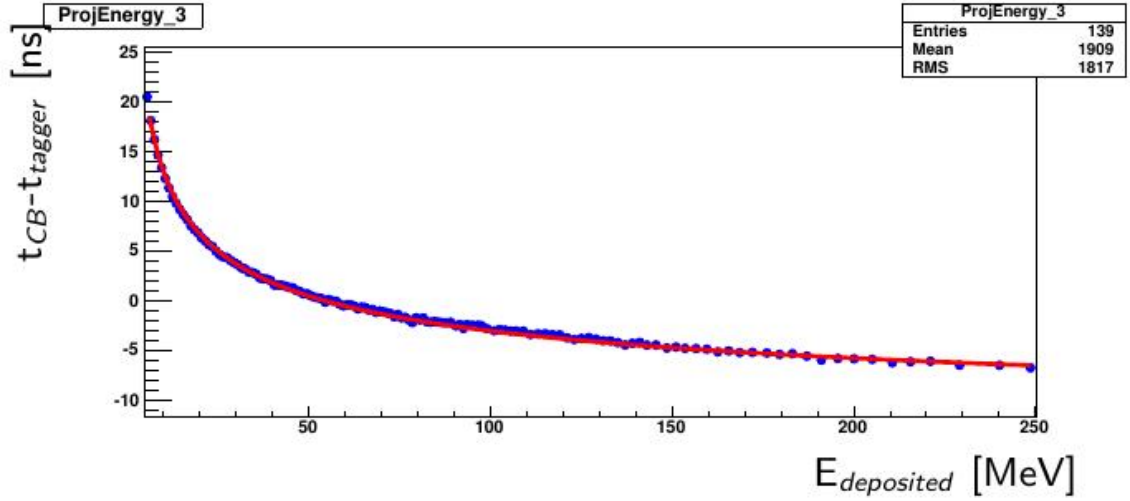


Figure 5.8: Fit to time walk of CB using Equation 5.8 to apply a correction to the original calibrated time values. Taken from [105].

The term used to fit this distribution was subtracted from the original energy dependent times to determine new (energy independent) times for each element.

$$t_{corrected} = t_{original} - \left( a + \frac{b}{(E + c)^d} \right) \quad (5.9)$$

#### 5.2.4 PID

The PID elements were time calibrated using Equation 5.7 to find the correct offsets to align the relative time of each element. This is shown before and after in Figure 5.11.

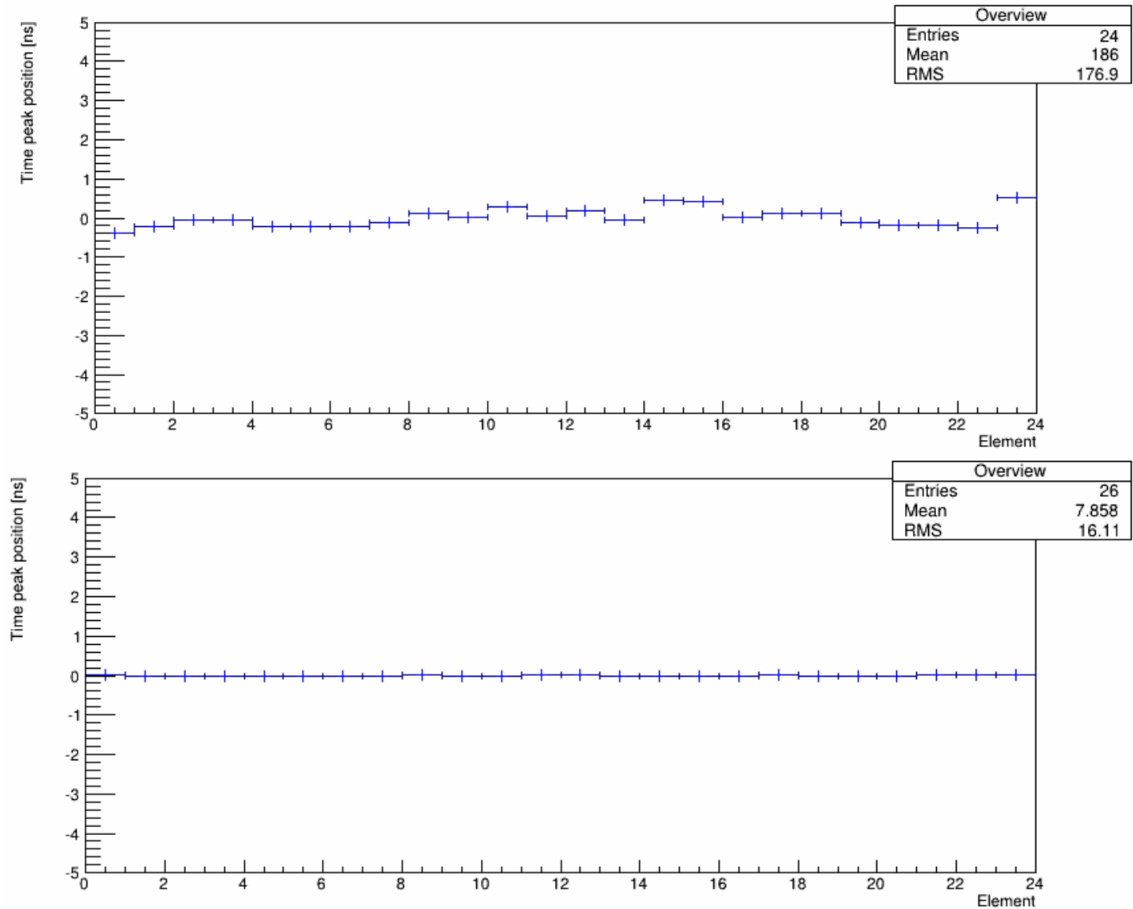


Figure 5.9: PID time calibration. Top: unaligned time offsets for each PID element. Bottom: Calibrated time offsets for each PID elements. Taken from [105]

### PID azimuthal alignment

The azimuthal alignment of the PID elements needed to be known for identification of charged particles where the  $\phi$  difference with the CB is used. Each time the target is re-polarised the alignment needed to be recalibrated due to moving the PID to remove the target from the central detector system. The calibration of the PID alignment was done by plotting the azimuthal angle of each element and fitting the signal peak with a Gaussian to determine the  $\phi$  angle of that element. Restricting the selection of events to one cluster in the CB and one hit in the PID provides a large signal to background ratio allowing for a cleaner fit. Plotting the azimuthal angle, determined from the Gaussian fit, against element number, the relative  $\phi$  angles of each PID element can be determined. Fitting a linear function to this allows the

relative  $\phi$  angles of the PID elements to be calibrated (Figure 5.10).

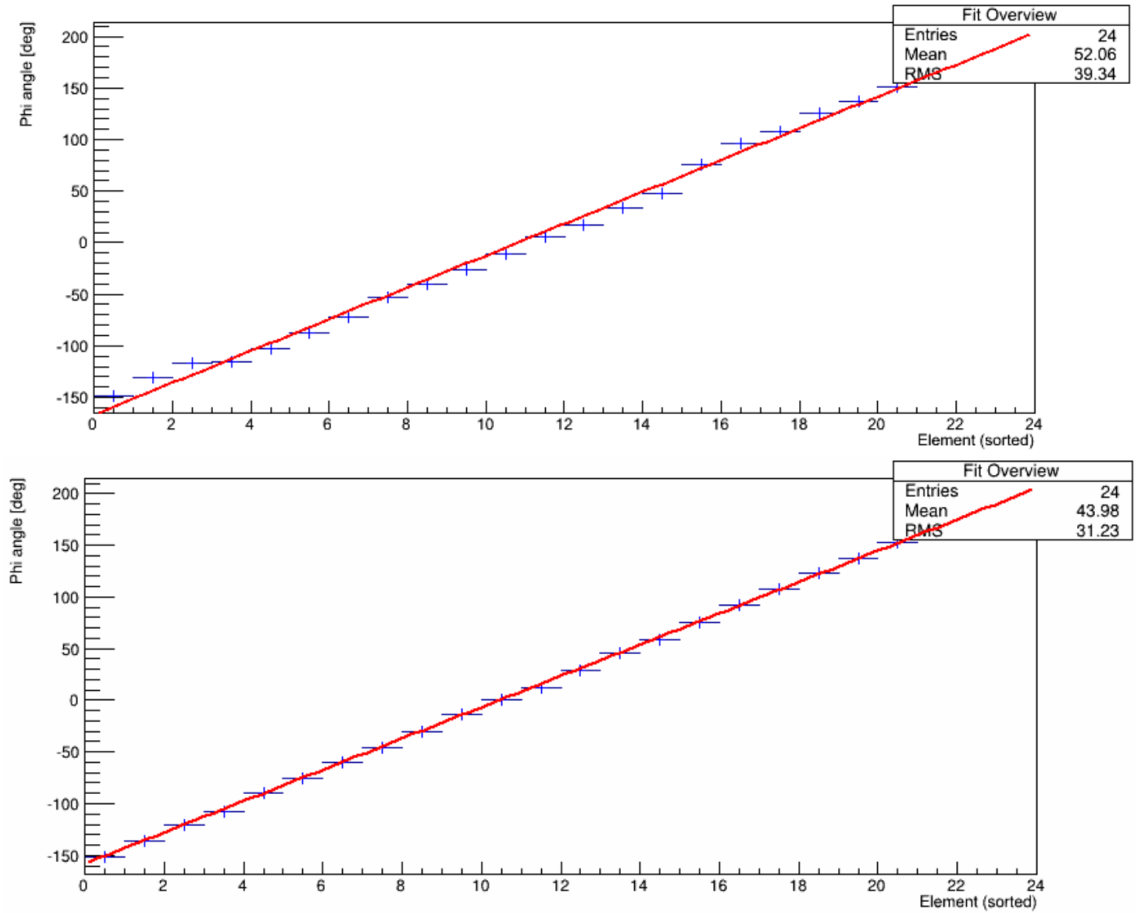


Figure 5.10: PID angle calibration. Top: uncalibrated  $\phi$  angles of each PID element. Bottom: calibrated  $\phi$  angle of each PID element. Taken from [105]

### 5.2.5 TAPS

TAPS uses Constant Fraction Discriminators (CFDs) to avoid the walk correction. The gain of each TDC was calibrated by adding delay cables in series, each with a 10ns delay time, increasing the common stop time. The change in position of the pulser signal time (from the original position) was plotted against the difference in the delay of the signal. Fitting this allowed a measure of the gain to be calculated.

Offline analysis was used to calibrate the TDC offset times after the experiment. Using Equation 5.7 new offset positions were calculated to align the relative time of the TAPS elements.

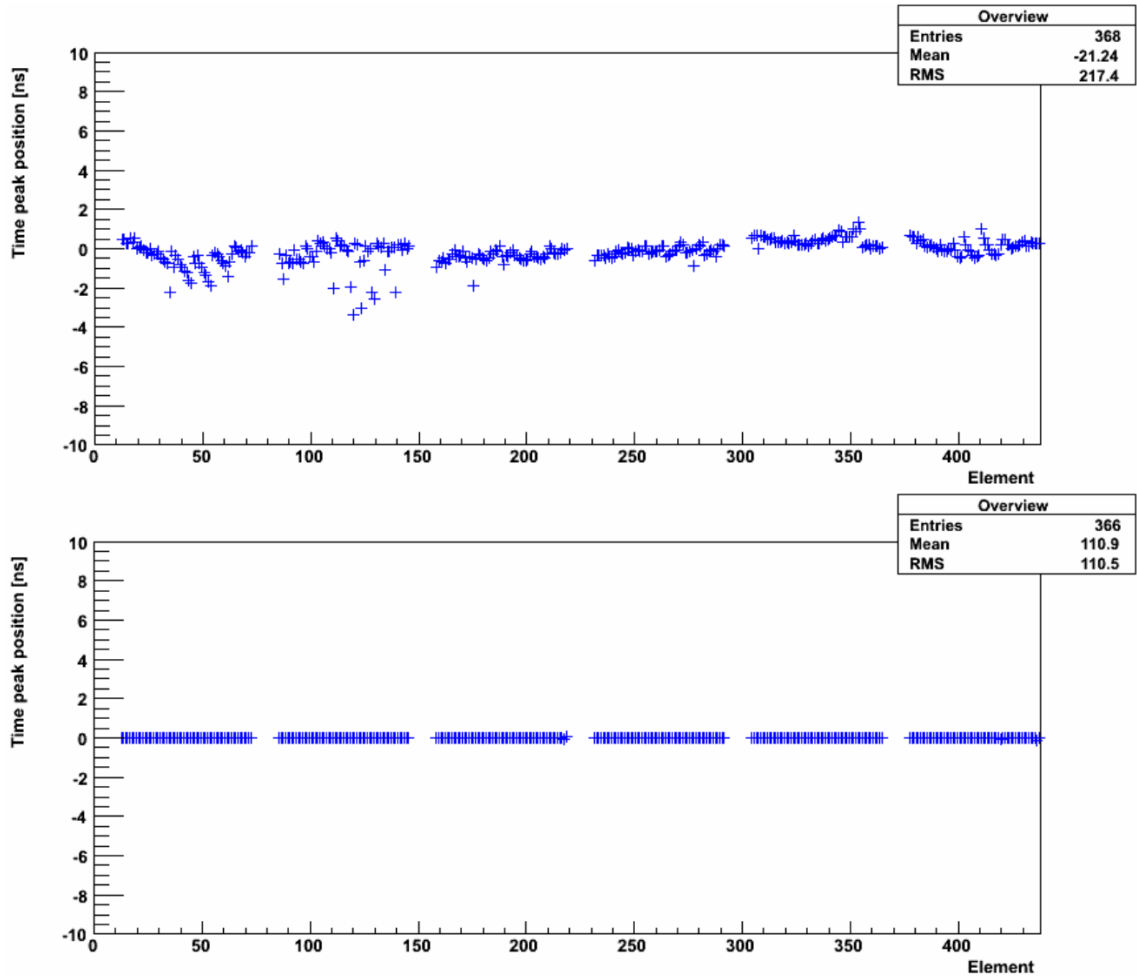


Figure 5.11: TAPS time calibration. Top: uncalibrated timing alignment of TAPS elements. Bottom: Time offset calibrated TAPS elements. Taken from [106]

## 5.3 Linear Polarisation of the Photon Beam

The degree of linear polarisation affects the values of the polarisation observables measured as part of this work. It is therefore important to measure this accurately for the entire photon energy range.

The degree of linear polarisation was extracted by fitting an enhancement (Section 4.3) with a phenomenological function. Including all possible lattice plane contributions in a phenomenological fit to an enhancement plot would be prohibitively difficult. Instead, only the strongest contributions to the enhancement, the 022, 044 and 066 lattice vectors were considered, shown in Figure 5.12. Contributions from

other lattice vectors were negligible in this region.

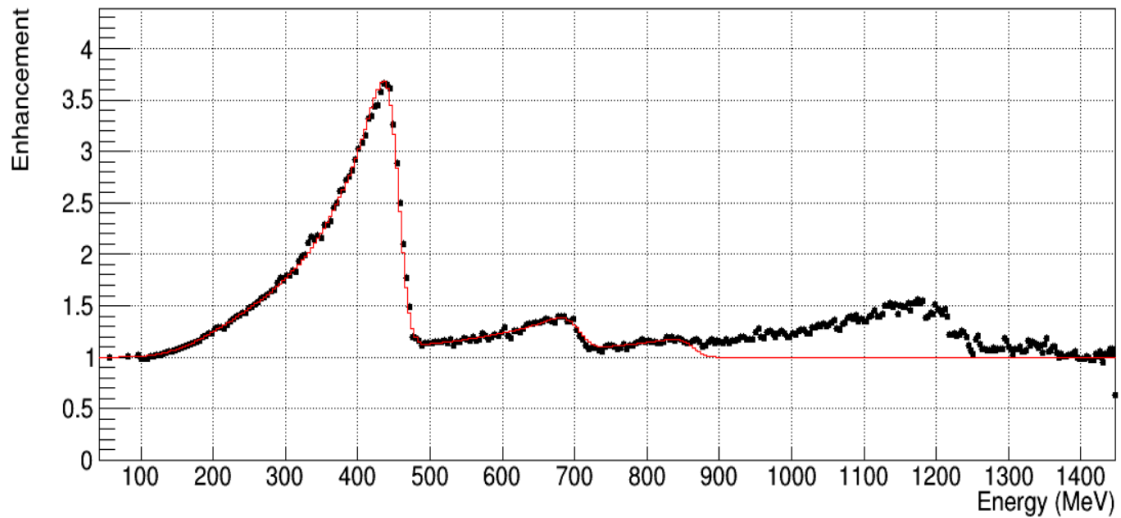


Figure 5.12: Enhancement plot with phenomenological fit (red) applied to enhancement data (black) to extract degree of linear polarisation.

The phenomenological fit [107] used had five free parameters per lattice vector. The free parameters, shown in blue in Figure 5.13, are:  $I$ , the peak amplitude of the enhancement;  $\theta$ , the half point along the drop of the 022 edge (associated with the relative angle of the beam and lattice);  $\phi$ , the width in the peak around  $\theta$ ;  $\theta_r$  and  $\phi_r$  are the opening angle of the collimator and the variation in this opening angle respectively. Each of the three peaks has their own set of free parameters associated with it.

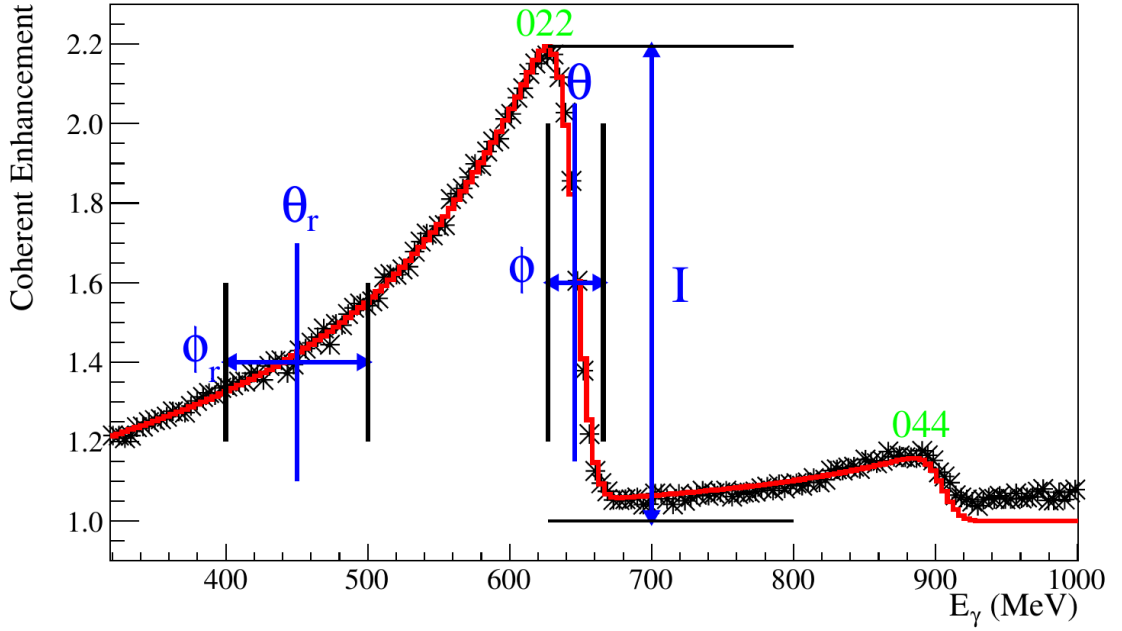


Figure 5.13: Enhancement plot with phenomenological fit (red)[107] applied to enhancement data (black) to extract degree of linear polarisation. Free parameters of the fit are shown in blue.

When fitting to the enhancements the distributions needed to be normalised. A mean of five bins in series was calculated across the entire range of the enhancement, and where this mean had its lowest value the distribution was renormalised to 1. An example fit is shown in Figure 5.12 for a main coherent peak around 450 MeV.

The resulting enhancement distribution was used to calculate the degree of linear polarisation as a function of energy for the photon beam, shown in Figure 5.14, using Equation 5.10 derived in [108].

$$P_{tot}^s(x, G, \theta, \sigma) = \frac{- \int_{\theta-3\sigma}^{\theta+3\sigma} \left\{ e^{\frac{(\theta'-\theta)^2}{2\sigma^2}} \times \phi_{tot}(x, G, \theta') \times I_{coh}(x, G, \theta') \right\} d\theta'}{\int_{\theta-3\sigma}^{\theta+3\sigma} \left\{ I_{total}(x, G, \theta') \times e^{\frac{(\theta'-\theta)^2}{2\sigma^2}} \right\} d\theta'} \quad (5.10)$$

where  $x$  is the photon energy,  $\sigma$  is the Gaussian smearing of  $\theta$  accounting for beam divergence and multiple scattering effects and  $G$  represents the lattice vector in question. The intensities of the coherent contribution and total distribution are represented by  $I_{coh}$  and  $I_{total}$  respectively. The parameters from the fit to the enhancement were then fed into the event stream once the photon energy was determined

for the event, assigning a degree of linear polarisation to that event.

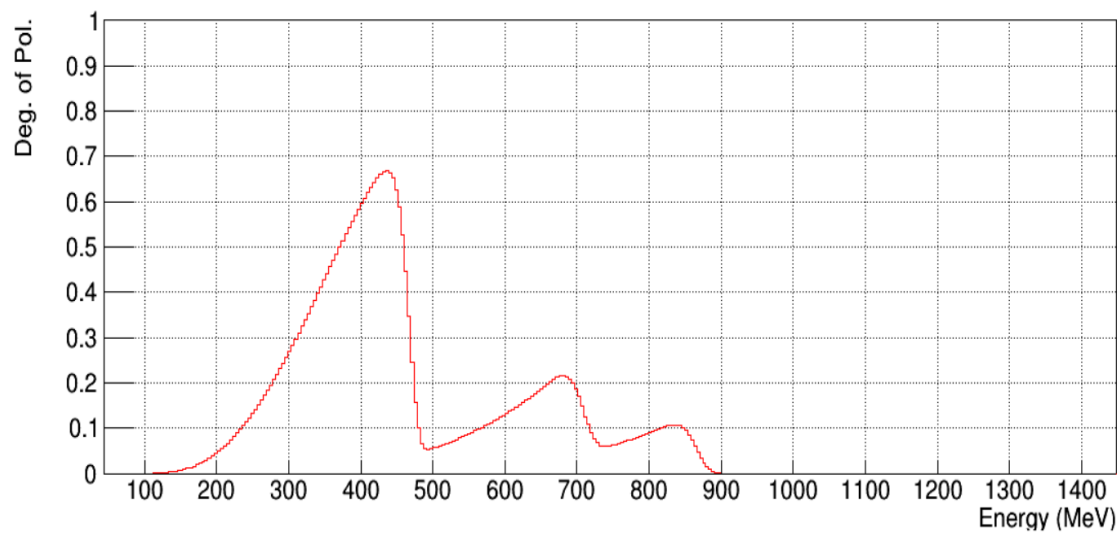


Figure 5.14: The degree of linear polarisation calculated from the phenomenological fit to the enhancements seen in Figure 5.12.

# Chapter 6

## Signal Selection

This section covers several aspects of the data analysis including the software (Section 6.1), the event selection process (Section 6.2) and background subtraction methods (Section 6.3).

### 6.1 Software

The software used to perform data analysis comprises of in-house packages AcqRoot and GoAT, built on the CERN ROOT data analysis framework. AcqRoot [99], written in C++ and based on the CERN ROOT libraries, focuses primarily on initial offline analysis including calibration (see Chapter 5) and particle reconstruction. AcqRoot reads the detector QDCs and ADCs and applies calibration parameters outlined in Chapter 5 to calculate energies and times. These variables are passed to higher level classes which reconstruct particle 4-vectors for further analysis. These 4-vectors along with beam and target polarisations, and coincidence time were then written out to ROOT tree data stores.

GoAT (Generation of Analysis Trees) was designed to provide a fast, tree-based analysis framework. It produced generic analysis trees from AcqRoot which were processed to sort data, reconstruct particle information and check data. A lot of the difficulties of working with trees from AcqRoot were side-stepped with the

GoAT software using a single configuration file to specify the sorting choices and reconstruction options for the user.

ROOT [109] is an analysing framework developed at CERN and used to handle the large amounts of data that comes from particle and nuclear experiments. ROOT has a large range of functionality allowing the user to create their own physics classes for event selection and analysis. The event selection process performed as part of this analysis is described below.

## 6.2 Event Selection

Event selection covered the correct selection of the reaction channel  $\gamma p \rightarrow \pi^0 p$ . This reaction channel has a three body final state as the  $\pi^0$  decays into two photons.

Due to the final state, a restriction on the number of cluster hits was used to identify the final state,  $\pi^0 p \rightarrow \gamma\gamma p$ , and as such was set to three. Each cluster was initially assumed to be a photon. This was assumed because of a lack of charge information, as the PID was not used in the data analysis due to difficulties experienced in calibration.

After the restriction on the number of clusters, the two photon combinations with invariant mass (IM) that best matched the  $\pi^0$  PDG invariant mass were selected as the  $\pi^0$  decay photons. The initial particles were reconstructed by summing the 4-vectors of their decay products, given by

$$P_{\text{Initial}} = \sum_{i=1}^n p_i \quad (6.1)$$

where  $P_{\text{Initial}}$  is the 4-momentum of the mother particle and  $p_i$  is the 4-momentum of each daughter particle. The invariant mass of a mother particle with only two daughter particles is given by

$$M_{\text{Inv}} = \sqrt{(\mathbf{p}_1 + \mathbf{p}_2)^2} = \sqrt{m_1^2 + m_2^2 + 2(E_1 E_2 - \vec{p}_1 \cdot \vec{p}_2)} \quad (6.2)$$

where  $M_{Inv}$  is the invariant mass of the mother particle and  $m_{1,2}$ ,  $E_{1,2}$  and  $\vec{p}_{1,2}$  are the mass, energies and 3-momenta of the daughter particles respectively. In the case of  $\pi^0$  decay the daughter particles are two photons with  $m_\gamma = 0$ , simplifying Equation 6.2 to

$$M_{\gamma\gamma} = \sqrt{2(E_{\gamma 1}E_{\gamma 2} - \vec{p}_{\gamma 1} \cdot \vec{p}_{\gamma 2})} \quad (6.3)$$

Identifying which pairs of 4-vectors originated from the mother particle was important for extracting polarisation observables. Where there are three detected particles, there are three combinations of photon pairings.

The best pairing for each event was determined as a minimum given by Equation 6.4

$$p_{\pi^0} = \left| \frac{M_{\gamma\gamma}}{M_{\pi^0}} - 1 \right|^2 \quad (6.4)$$

where  $M_{\pi^0}$  is the PDG mass of the  $\pi^0$ . The smallest value of  $p_{\pi^0}$  provided the best  $\pi^0$  candidate pairing. The  $\pi^0$  candidates were given the PDG invariant mass of the  $\pi^0$  while retaining their 3-vectors.

### Proton Reconstruction

Additional kinematic constraints were available due to the detection of the proton in the CB. This allowed a comparison between the proton reconstructed from the beam, target and  $\pi^0$  4-vectors, given by Equation 6.5, and the measured third cluster in the CB (Section 6.4.5).

$$P_{Missing} = \gamma_{tagged} + P_{Target} - P_{\pi^0} \quad (6.5)$$

Table 6.1 outlines the 4-vectors used to calculate the missing particle 4-vectors ( $P_{Missing}$ ). The distribution of missing mass is shown in Figure 6.1. A peak can be seen at the expected PDG mass of the proton, sitting on top of a large background.

The background largely contains tagged bremsstrahlung photons that are in random coincidence with the reaction event.

4-vector component	$P_x$	$P_y$	$P_z$	E
Target	0	0	0	$M_{proton}$
Beam	0	0	$E_{Beam}$	$E_{Beam}$
Decay $\gamma_1$	$P_x(\gamma_1)$	$P_y(\gamma_1)$	$P_z(\gamma_1)$	$E_{\gamma_1}$
Decay $\gamma_2$	$P_x(\gamma_2)$	$P_y(\gamma_2)$	$P_z(\gamma_2)$	$E_{\gamma_2}$

Table 6.1: Table outlining the 4-vector components of each particle used in reconstructing the missing proton 4-vector.

As the reaction target was a proton the energy component of the target 4-vector was given the proton mass and was at rest in the lab frame. The photon beam moved along the z direction in the lab frame which resulted in the z-component having the same value as the energy component. Decay  $\gamma_{1,2}$  are the decay photons of the best  $\pi^0$  candidates (Equation 6.4).

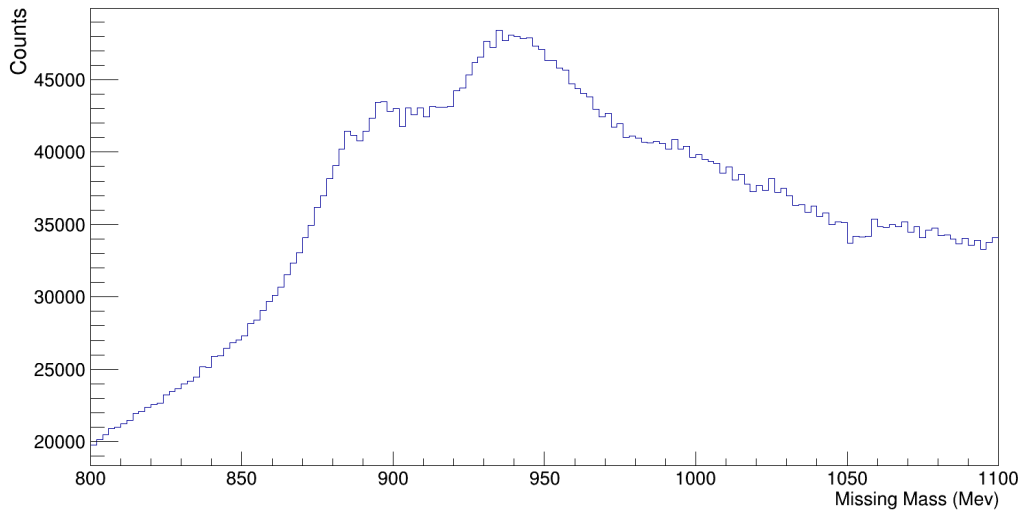


Figure 6.1: Missing mass distribution after  $\pi^0$  candidate selection. Proton peak can be seen at 940 MeV on top of a large background.

With the reaction particles identified the background events had to be accounted for so the events of interest could be separated. The  $s\mathcal{P}$ lot technique (Section 6.4) was used to separate signal from background events. The background due to random

coincidences with tagged bremsstrahlung photons, which cannot be uniquely singled out, was also accounted for using the  $s\mathcal{P}$ Plot technique (Section 6.4.2). The missing mass, third cluster hit, not identified as one of the  $\pi^0$  decay photons, and coplanarity were used to separate signal from nuclear background events in Sections 6.4.4, 6.4.5 and 6.4.6 respectively.

## 6.3 Background subtraction

A background subtraction was performed to identify the photon which triggered the event and to remove the events which originated from Carbon and Oxygen nuclei inside the butanol target (referred to from here-on as nuclear background) from those that originated from the polarised protons. Section 6.4 discusses the formalism and details of the  $s\mathcal{P}$ Plot weighting method which was used in this analysis. The  $s\mathcal{P}$ Plot method was used to remove photon candidates created from random tagger hits, as well as separate the signal events from nuclear background events.

The following table summarises the general cuts applied to the data throughout the analysis. The cuts were made in order to better select events originating from the  $\gamma p \rightarrow \pi^0 p$  reaction given the expected values of the final state.

Variable	Cut Range	Units
Tagged Time	$-20 < T_{Tagged} < 20$	ns
Missing Mass	$880 < M_{Miss} < 1000$	MeV
Coplanarity	$90 < \phi < 270$	$^\circ$ (degrees)
Proton Opening Angle	$0 < \theta_{open} < 25$	$^\circ$ (degrees)
2 photons	$120 < M_{Inv} < 150$	MeV

Table 6.2: Cuts applied based on expected reaction kinematics to aid event selection.

## 6.4 *sPlot* method

The *sPlot* technique provides event-by-event weights known as *sWeights* which can be used to disentangle different event species such as actual and random tagged photons. For this analysis sequential fits were performed to separate tagger random events from prompt signal events before being used again to separate nuclear background events. The initial separation was done using the *sWeights* obtained from a fit to the Tagger-CB coincidence time spectra. The second was done separately for fits to the missing mass, the coplanarity (angle between the  $\pi^0$  and proton), and the opening angle between the detected and reconstructed proton spectra. Using different variables to discriminate the nuclear background provided a useful comparison for assessing the effectiveness and consistency of the technique.

### 6.4.1 *sPlot* formalism

Events in a data set usually originate from more than one source. The aim of *sPlots* [110] is to separate these sources. The events are therefore categorised into two different variable types: discriminating variables, and control variables. Discriminating variables are variables for which a distribution is known for all sources and control variables are ones for which some sources are unknown. Using the *sPlots* technique it is possible to recreate the distributions of the control variables without any prior knowledge of their distributions. It is important to note that the control and discriminatory variables should be uncorrelated when performing the extended maximum likelihood fit. The formalism of *sWeights* starts with defining the log-Likelihood to describe an extended maximum likelihood fit to data

$$\mathcal{L} = \sum_{e=1}^N \ln \left\{ \sum_{i=1}^{N_s} N_i f_i(y_e) \right\} - \sum_{i=1}^{N_s} N_i \quad (6.6)$$

where  $N$  is the total number of events,  $N_s$  is the number of different types of events in the data (species),  $N_i$  is the number of events in the  $i^{th}$  species,  $y$  is the set of discriminating variables, and  $f_i(y_e)$  is the PDF value of the  $i^{th}$  species for variable

$y$  and event  $e$ . By maximizing Equation 6.6 it is possible to determine the value of the yields of the different species of events in the data while using a full list of discriminating PDFs. The only free parameters in the fit are the species yields  $N_i$ .

The covariance matrix from the maximum likelihood fit is given in Equation 6.7 and is central to the calculation of the weights used to reproduce the true distribution of a control variable. It is defined as

$$V_{nj}^{-1} = \frac{\partial^2(-\mathcal{L})}{\partial N_n \partial N_j} = \sum_{e=1}^N \frac{f_n(y_e) f_j(y_e)}{(\sum_{k=1}^{N_s} N_k f_k(y_e))^2} \quad (6.7)$$

Using the covariance matrix it is possible to obtain an expression for the weights (Equation 6.8) when the control and discriminatory variables are uncorrelated. The proof of this is given in [110].

$${}_s\mathcal{P}_n(y_e) = \frac{\sum_{j=1}^{N_s} V_{nj} f_j(y_e)}{\sum_{k=1}^{N_s} N_k f_k(y_e)} \quad (6.8)$$

With the above expression for the *sWeights* it is possible to accurately disentangle a dataset into the various components contributing to it and reproduce the true distributions of other variables for each component, provided those distributions are not correlated to the variable that was used in the fit.

*sPlots* has useful properties which are worth noting here.

$$\sum_{e=1}^N {}_s\mathcal{P}_n(y_e) = N_n \quad (6.9)$$

The yield of the species is equal to the sum of the weighted events of that species

$$\sum_{e=1}^N \mathcal{P}_l(y_e) = 1 \quad (6.10)$$

The sum of the weights from each species for a particular event, in each bin, is equal to one. These properties provide constraints in ensuring *sPlots* are used accurately.

### 6.4.2 Time separation

The tagger-CB coincidence time spectrum has a sharp peak on top of a flat background. The sharp peak is where the events of interest lie and there is a coincidence between the CB and Tagger. The flat background represents random coincidence photons. The fit to the timing spectrum was performed using two probability density functions (PDFs). A Gaussian was used to fit the sharp peak and a first order polynomial was used to fit the flat background.

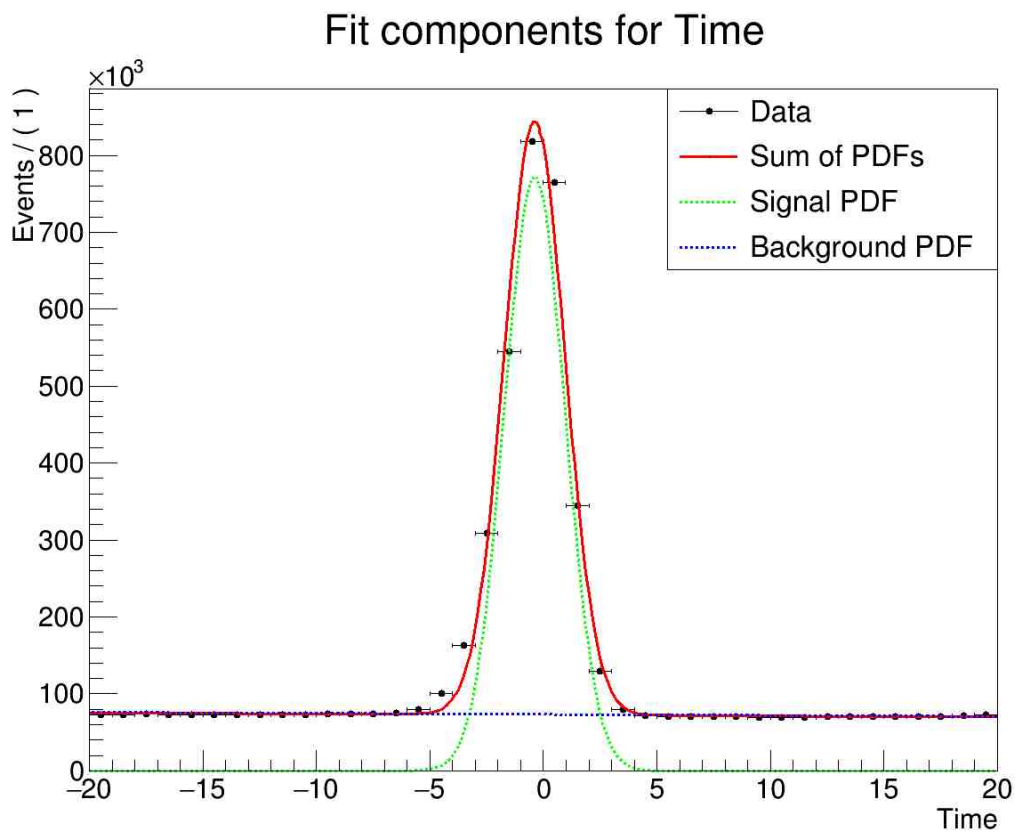


Figure 6.2: Maximum likelihood fit to tagged timing spectrum using a Gaussian and a first order polynomial to fit the peak and flat background respectively.

Figure 6.2 shows a maximum likelihood fit using the sum of the Gaussian and polynomial PDFs. After the fit a weight was calculated for each event using Equation 6.8. The signal weights were applied to the data to separate out the signal distribution for other variables. These weights therefore select out events with the correct photon in coincidence with the reaction products in the CB. Additional background

from sources such as the nuclei in the butanol or multi-pion production need to be disentangled with an additional *sPlot* fit.

### 6.4.3 Nuclear background separation

As all three particles are detected, there are multiple discriminatory variables available for separating the  $\gamma p \rightarrow \pi^0 p$  signal from other reaction mechanisms.

Fits to the missing mass, coplanarity and opening angle of detected and reconstructed protons were performed individually to separate the nuclear background from signal events. The different variables each have distinct shapes, however they should result in similar event yields for signal and background events.

The main source of background was from the bound protons in the Carbon and Oxygen of the Butanol target. Data was taken using a carbon target to model this source of background. For each discriminatory variable the spectra was produced using the carbon data, itself used as a PDF for fitting the data distribution. Monte Carlo was used to generate the signal PDF. The Monte Carlo generated event tracks which came directly from the proton and simulated them in the A2 detector set up using Geant4 (Section 4.9). The weights of the tagged timing spectra were applied to the data and PDFs before performing the secondary fits. The Monte Carlo of the signal events required no timing background subtraction as it simulated the exact reaction of interest.

The events-based PDFs that are used had additional parameters associated with them when fitting the data distributions. These parameters accounted for discrepancies between simulation and data. The flexible parameters are

- Gaussian smearing
- PDF offset
- PDF scaling

where the scaling is the stretching of the PDF in the variable axis, offset is the overall position along the variable axis and the Gaussian smearing accounts for an

additional convoluted resolution. The carbon data did not have any flexibility in the offset or scaling as this was real data and was performed under the same conditions as the butanol data.

#### 6.4.4 Missing Mass fit

Figure 6.3 shows an example fit to the missing mass spectrum, as given by Equation 6.5, using the signal and nuclear background PDFs. The missing mass spectrum for both signal events and carbon background events have distinct shapes which makes the missing mass a good discriminator between the two species of events.

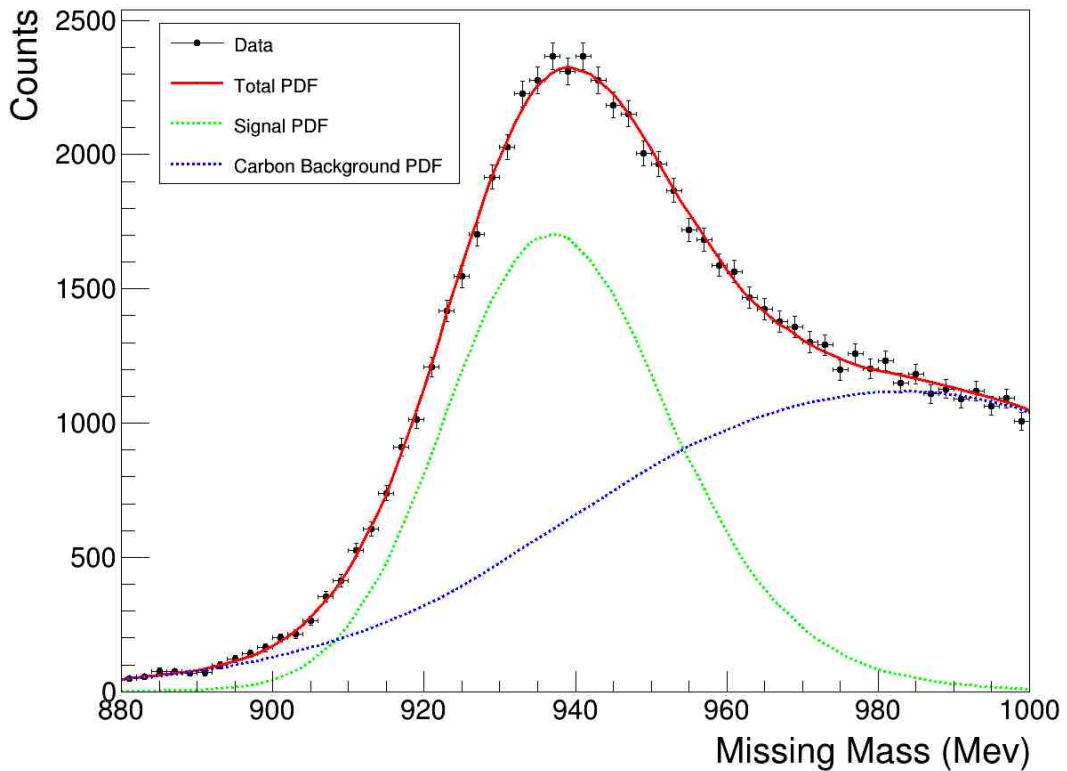


Figure 6.3: Fit to the missing mass spectrum showing a peak around the proton mass. The dashed blue line is the carbon background, dashed green line is signal PDF from Monte Carlo and the solid red line is the total PDF fit to the data points. Fit shown for kinematics  $-0.2 < \cos(\theta) < 0$ ,  $403 < E_\gamma < 436$  MeV.

### 6.4.5 Proton opening angle fit

The opening angle between the reconstructed and detected proton is a good discriminator again due to the distinct shapes of the two PDFs used in the fit. The opening angle was defined as the angular difference in the reconstructed missing particle 4-vector and the detected third cluster hit.

$$\Delta\theta_{open} = \vec{p}_{recon} - \vec{p}_{detected} \quad (6.11)$$

A large peak was seen at low opening angles where the 4-vectors coincide when the correct  $\pi^0$  candidates were selected. The peak at low angles sat on top of a nuclear background which was accounted for by using a PDF from carbon data.

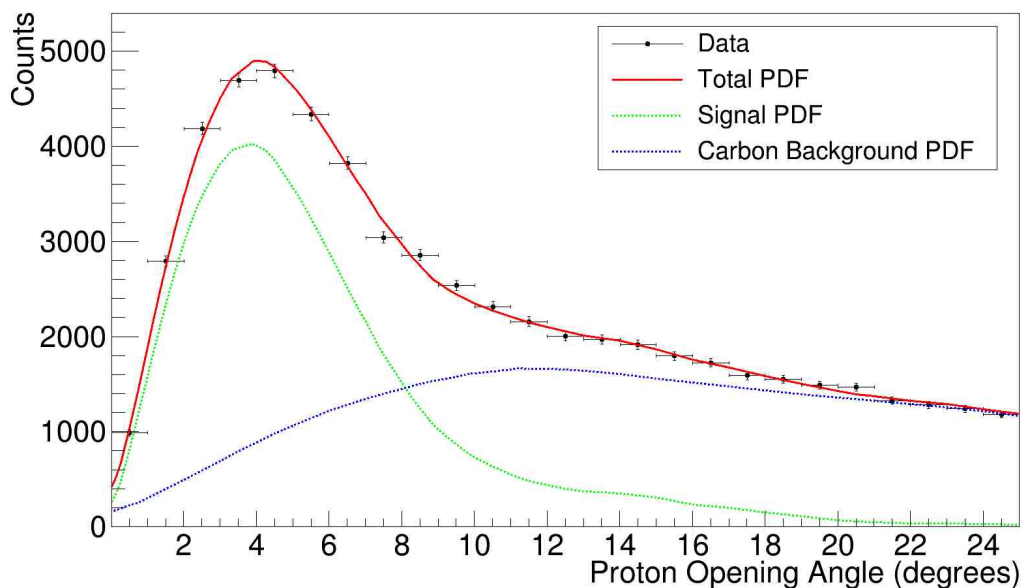


Figure 6.4: Fit to opening angle between detected and reconstructed proton. The dashed blue line is the carbon background, dashed green line is signal PDF from Monte Carlo and the solid red line is the total PDF fit to the data points. Fit shown for kinematics  $-0.2 < \cos(\theta) < 0$ ,  $403 < E_\gamma < 436$  MeV.

### 6.4.6 Coplanarity fit

Due to momentum conservation the proton has to lie on the reaction plane created by the incident tagged photon and the  $\pi^0$  meson provided they both originated from

the  $\gamma p \rightarrow \pi^0 p$  reaction. The condition can be checked by looking at the difference in azimuthal angle between the proton and  $\pi^0$  meson:

$$\Delta\phi = \begin{cases} \phi_{\pi^0} - \phi_p, & \text{if } \Delta\phi \geq 0 \\ 2\pi - |\phi_{\pi^0} - \phi_p|, & \text{if } \Delta\phi \leq 0 \end{cases} \quad (6.12)$$

This condition is independent of the z-direction, and so is unaffected by the Lorentz-boost into the center-of-mass frame.

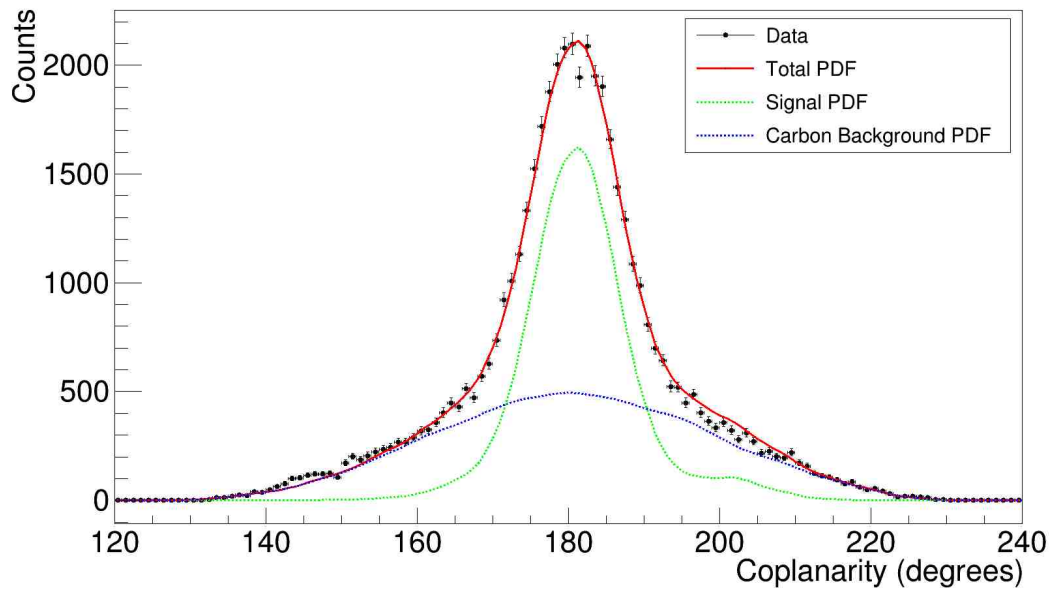


Figure 6.5: Fit to coplanarity between  $\pi^0$  and detected proton. The dashed blue line is the carbon background, dashed green line is signal PDF from Monte Carlo and the solid red line is the total PDF fit to the data points. Fit shown for kinematics  $-0.2 < \cos(\theta) < 0$ ,  $403 < E_\gamma < 436$  MeV.

A consistency check of the weights from fits to the different variables is to plot other distributions with the signal PDF weights applied and compare the distributions, shown in Figure 6.6.

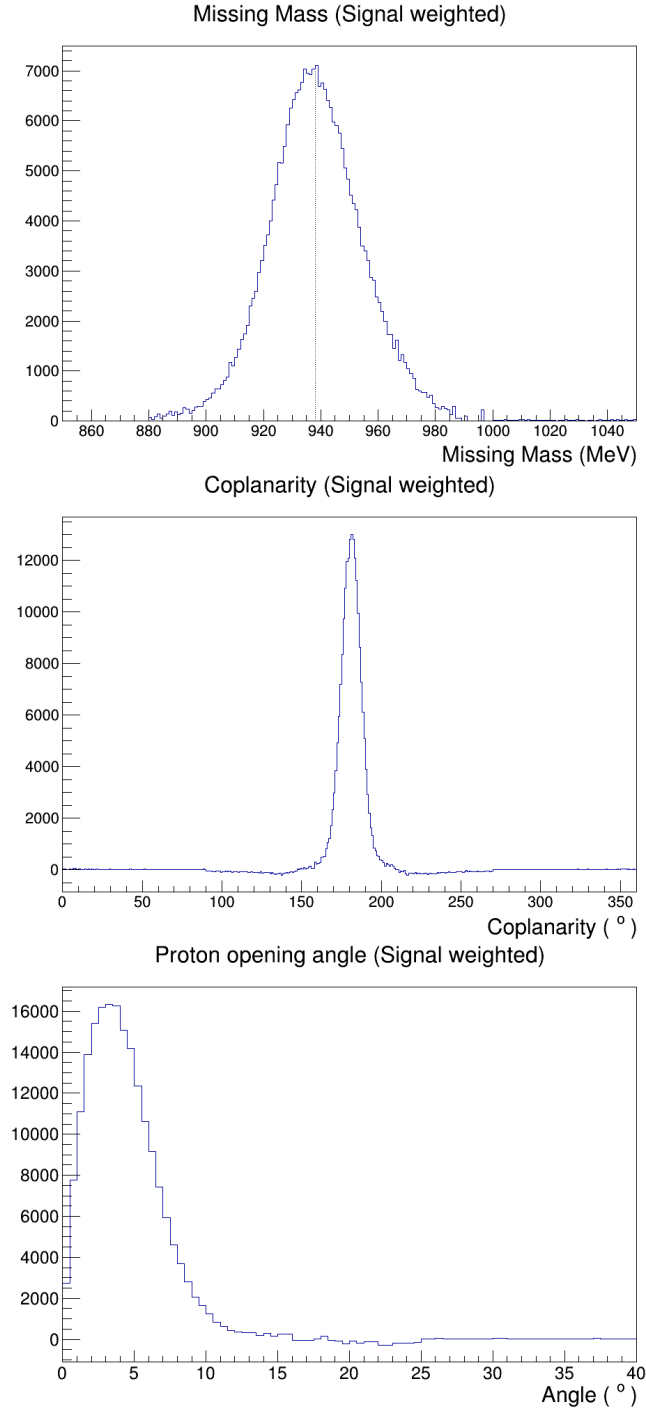


Figure 6.6: Distributions of missing mass (Top), coplanarity (Middle) and proton opening angle (Bottom) having been nuclear background subtracted to leave behind the desired signal events.

Having identified the events of interest, using the  $s\mathcal{P}$ lot technique, the polarisation observables were extracted using fits to azimuthal asymmetry distributions for different target polarisation states. This is discussed further in Chapter 7.

# Chapter 7

## Observable Extraction

This chapter illustrates how the experimental data was analysed to extract the polarisation observables. Further analysis of these observables by Partial Wave Amplitude groups in the future will provide quantitative information on the underlying photoproduction amplitudes and contributing resonant states. The introduction of asymmetries is given in subsection 7.1.1, the development of the function to fit the asymmetries is given in subsection 7.1.2 and an example of the fit to data is given in subsection 7.1.5. Investigations of the reliability of the fit function are detailed in Section 7.1.3. The outline of determining the  $\phi_0$  offset of the asymmetries seen in the data is given in subsection 7.1.4.

### 7.1 Asymmetries

The final part of the data analysis is the extraction of the polarisation observables. This section describes the process by which the observables are extracted having applied the sWeights obtained in the previous chapters to subtract the tagged photon, and nuclear backgrounds from the data.

### 7.1.1 Cross section

From Section 2.2 the azimuthal distribution of  $\pi^0$  produced with a linear polarised photon beam on a longitudinally polarised target is given by:

$$\frac{d\sigma}{d\Omega}(\theta, \phi) = \frac{d\sigma_0}{d\Omega}(1 + P_L \Sigma \cos(2\phi) + P_L P^T G \sin(2\phi)) \quad (7.1)$$

where  $P_L$  is the degree of linear polarisation of the photons,  $P^T$  is the degree of longitudinal polarisation of the target and  $\Sigma$  and  $G$  are the polarisation observables we wish to extract.

The probability of a particle being detected may vary as a function of  $\phi$ , this is known as the detector acceptance and generally this must be accounted for when extracting parameters from angular distributions. However it is possible to eliminate the need for precise acceptance corrections by forming asymmetries in polarisation states of the beam or target.

### 7.1.2 Fit function

As a starting point for creating a function to fit the azimuthal asymmetries, Equation 7.1 coupled with the detector acceptance  $A(\phi)$  is used to write the number of pions detected at  $\phi$  as

$$N(\phi) = A(\phi)N(1 + P_L \Sigma \cos(2\phi + \phi_0) + P_L P^T G \sin(2\phi + \phi_0)) \quad (7.2)$$

where  $N$  is the unpolarised flux,  $P_L$  is the photon beam polarisation and  $P^T$  is the target polarisation. The offset angle,  $\phi_0$ , is aligned with the photon beam electric field vector. There are four distinguishable data sets when photon beam and target are polarised linearly and longitudinally respectively, outline in Table 7.1.

	45°	-45°
Positive	$N_{45^\circ}^+$	$N_{-45^\circ}^+$
Negative	$N_{45^\circ}^-$	$N_{-45^\circ}^-$

Table 7.1: Table outlining the different combinations of incident photon beam and target polarisation settings. Positive and negative refer to the target polarisation direction with respect to the beam momentum, while  $\pm 45$  is the orientation of the beam linear polarisation plane.

Each set may have a different mean values of  $N$ ,  $P_L$  and  $P^T$ . Considering the positive target polarisation setting for the moment and considering the different beam polarisation states we can write Equation 7.2 for each beam polarisation setting as

$$N_{45}(\phi) = A(\phi)N_{45}(1 + P_{45}(\Sigma \cos(2\phi + \phi_0) + P^+G \sin(2\phi + \phi_0))) \quad (7.3)$$

$$N_{-45}(\phi) = A(\phi)N_{45}N_R(1 - P_{45}P_R(\Sigma \cos(2\phi + \phi_0) + P^+G \sin(2\phi + \phi_0))) \quad (7.4)$$

where  $N_R = \frac{N_{-45}}{N_{45}}$  and  $P_R = \frac{P_{-45}}{P_{45}}$ .

The asymmetry between these data sets is defined as

$$Asym(\phi) = \frac{N_{45}(\phi) - N_{-45}(\phi)}{N_{45}(\phi) + N_{-45}(\phi)} \quad (7.5)$$

which clearly cancels the acceptance  $A(\phi)$  and can be written in full and rearranged as

$$Asym(\phi) = \frac{(1 - N_R) + (1 + P_R N_R)(P_{45} \Sigma \cos(2\phi + \phi_0) + P_{45} P^+ G \sin(2\phi + \phi_0))}{(1 + N_R) + (1 - P_R N_R)(P_{45} \Sigma \cos(2\phi + \phi_0) + P_{45} P^+ G \sin(2\phi + \phi_0))} \quad (7.6)$$

Note that in the limit  $N_R$  and  $P_R = 1$ , and  $P_{45} = P_{-45} = P_L$ , this simplifies to

$$Asym(\phi) = P_L \Sigma \cos(2\phi + \phi_0) + P_L P^+ G \sin(2\phi + \phi_0) \quad (7.7)$$

which is approximately the case with the current data. Equation 7.6 is expressed in

terms of fit parameters as

$$Asym(\phi) = \frac{(1 - C_3) + (1 + C_2 C_3)(C_1 \cos(2\phi + \phi_0) + C_0 \sin(2\phi + \phi_0))}{(1 + C_3) + (1 - C_2 C_3)(C_1 \cos(2\phi + \phi_0) + C_0 \sin(2\phi + \phi_0))} \quad (7.8)$$

where  $C_0 = P_{45}P^+G$ ,  $C_1 = P_{45}\Sigma$ ,  $C_2 = P_R$ ,  $C_3 = N_R$ .

By fitting Equation 7.8 the observables  $\Sigma$  and  $G$  were extracted from the measured azimuthal asymmetries for individual target polarisation settings.

### 7.1.3 Fit Function Investigation

Tests using generated data were performed in order to investigate how the different parameters of Equation 7.8 behaved under different conditions and whether this function was suitable to fit the asymmetries.

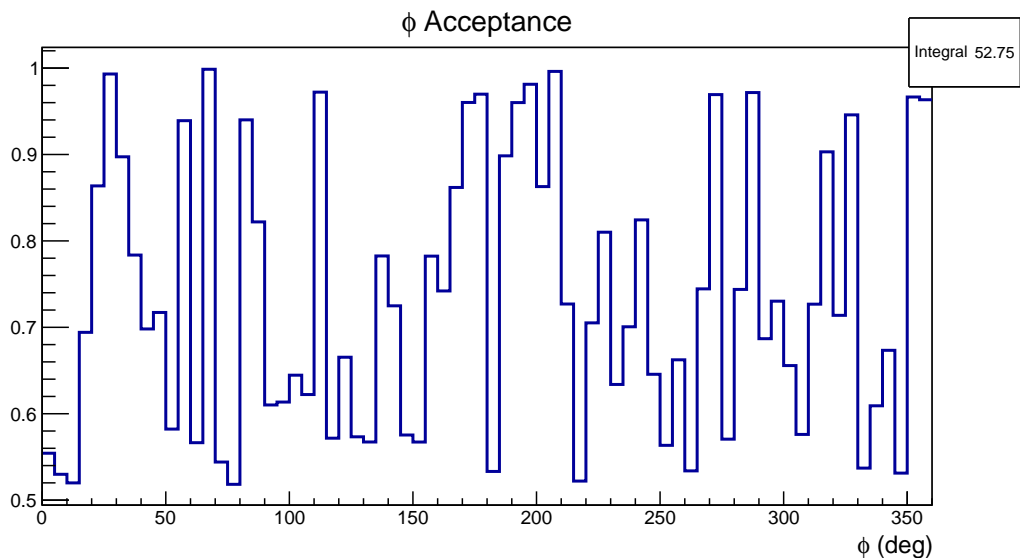


Figure 7.1: Toy detector acceptance applied to generated  $\phi$  distributions. A value of 1 on the scale equates to a detector acceptance of 100%.

$\phi$  distributions were generated using known values for the photon flux, degree of linear and target polarisations, and values for the polarisation observables  $\Sigma$  and  $G$ . This generated a perfect  $\phi$  distribution without any detector acceptance effects. In order to make the test more rigorous, artificial detector acceptance effects were added to the perfect  $\phi$  distributions before performing the fit (Figure 7.1).

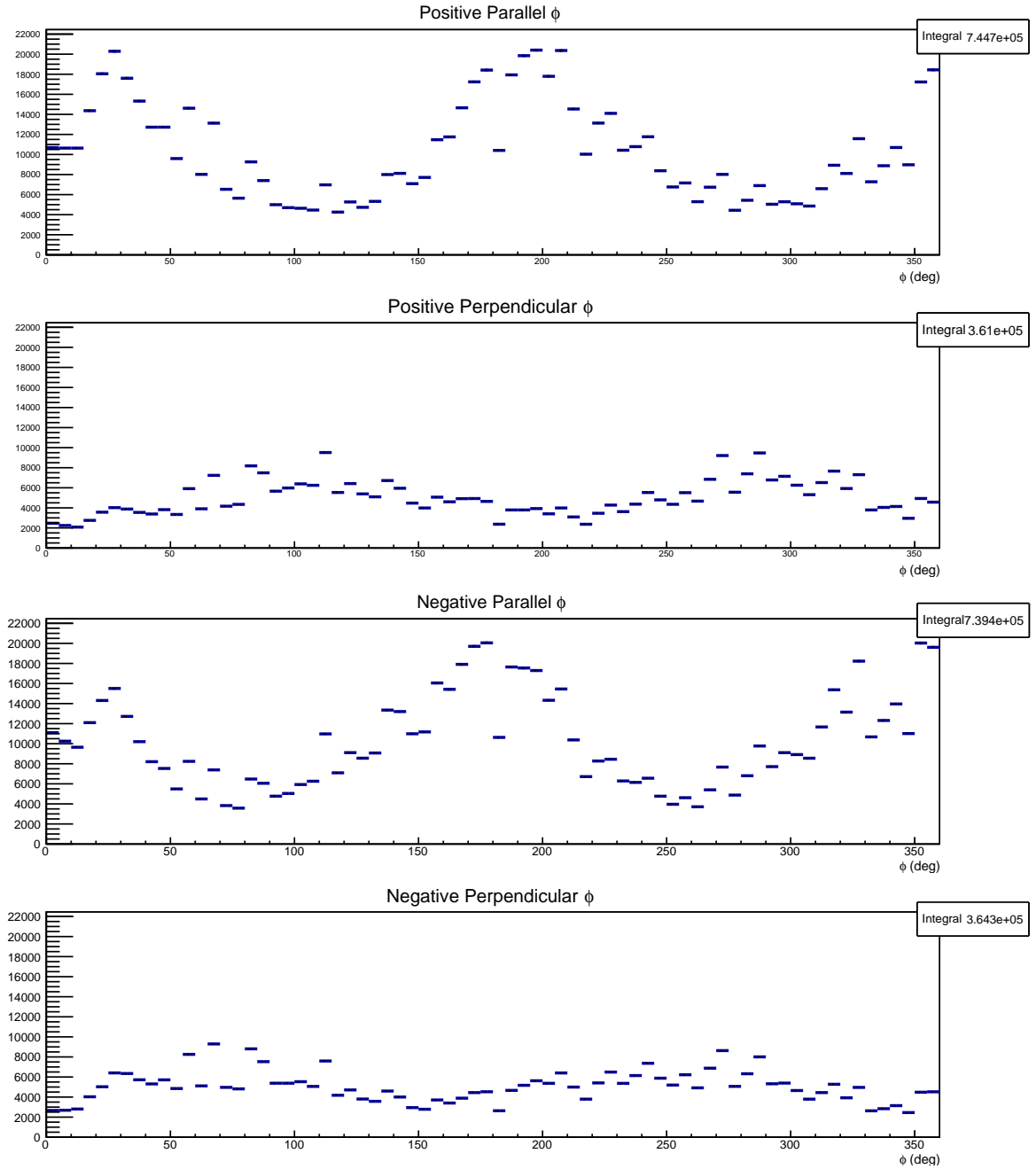


Figure 7.2: Generated  $\phi$  distributions with detector acceptances applied. Counts are shown on the y-axis with angle along the x-axis.

Once acceptance effects were added to the  $\phi$  distributions, asymmetries were created for each target setting as defined in Equation 7.5. The fit was applied and the parameters extracted were compared to the known input values used to generate the test distributions.

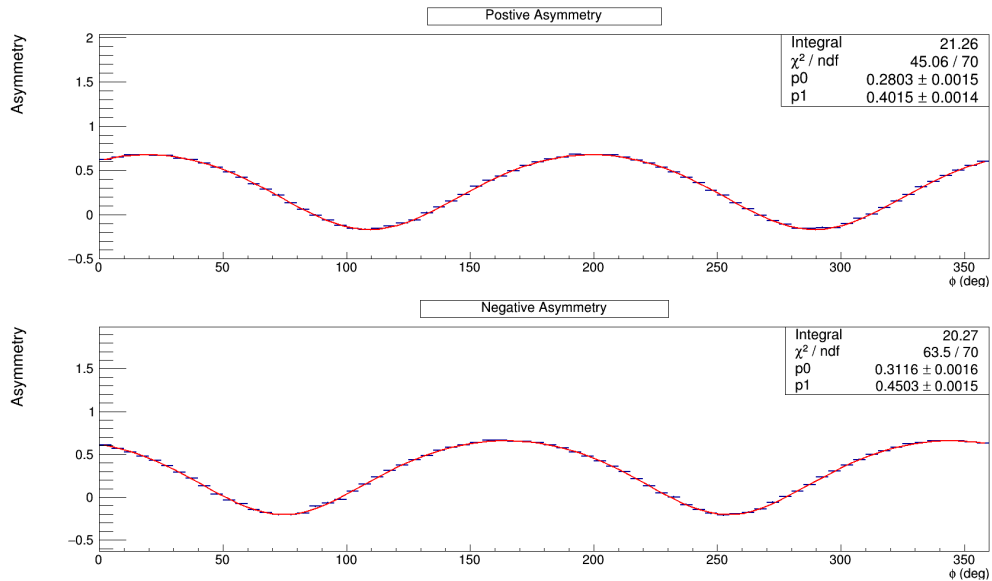


Figure 7.3: Fits to asymmetries using Equation 7.6 for positive and negative target polarisation settings separately. Top: Asymmetry of parallel and perpendicular  $\phi$  distributions with a positive target polarisation. Bottom: Asymmetry of parallel and perpendicular  $\phi$  distributions with a negative target polarisation. The y-axis shows the magnitude of the asymmetries.

The parameters of the function can be left free or fixed to a particular value when the function is fit to the data. For this test the parameters relating to the polarisation observables are left free as these are the unknown parameters to be measured. Parameters  $C_2$  and  $C_3$  can be fixed as these are derived from measured values of photon flux and linear polarisation.

The reliability of the extracted parameters was investigated by comparing the values of the extracted polarisation observables to the values used in generating the initial  $\phi$  distributions. Plots of observable magnitude against parameter  $C_2$  ( $C_3$ ) were made where parameter  $C_3$  ( $C_2$ ) was fixed to its true value as well as for where it was left free. Parameter  $C_2$  ( $C_3$ ) was fixed to a range of values between 0 and 1 (including its input value) to investigate the effect on the extracted observable value (Figures 7.4 and 7.5).

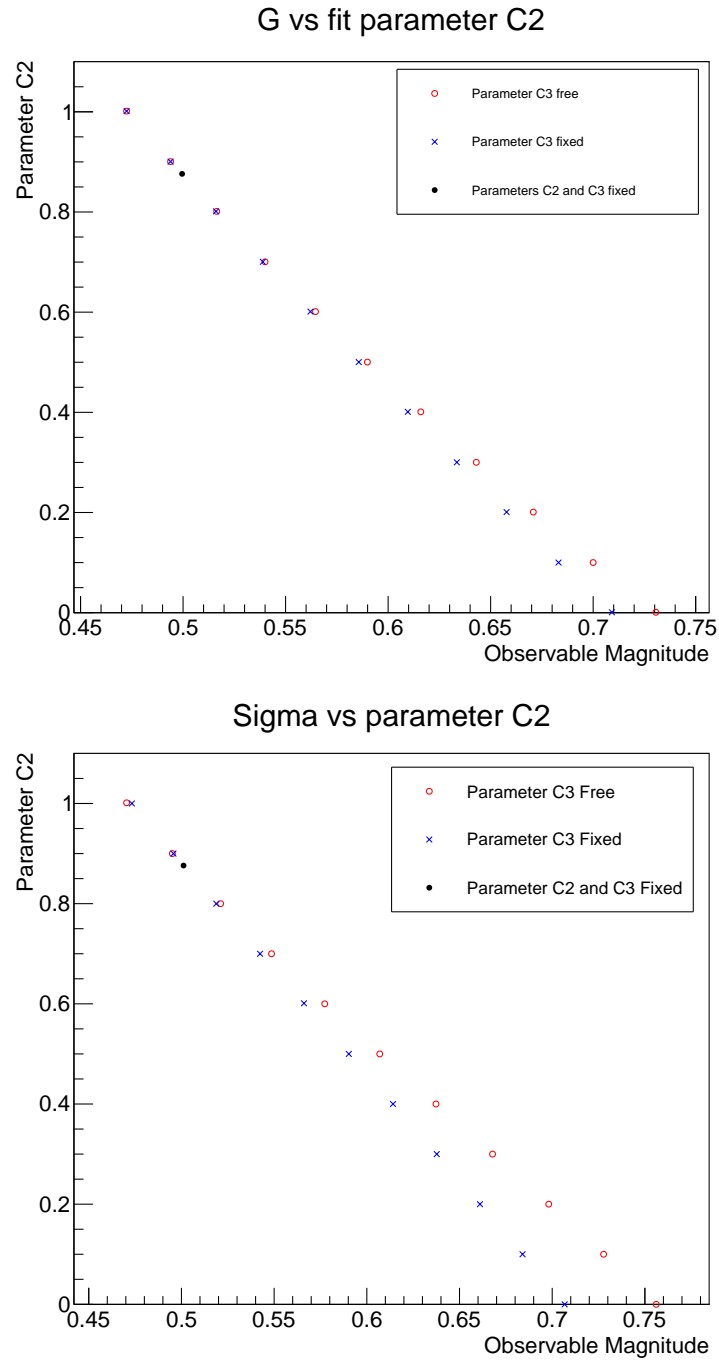


Figure 7.4: Changes of extracted polarisation observable magnitudes by varying parameter  $C_2$ . Blue points are where parameter  $C_3$  is fixed and red points are where parameter  $C_3$  is left free. Observable magnitudes closely match the input values used in generating the toy data when both  $C_2$  and  $C_3$  are fixed to their respective input values (black points).

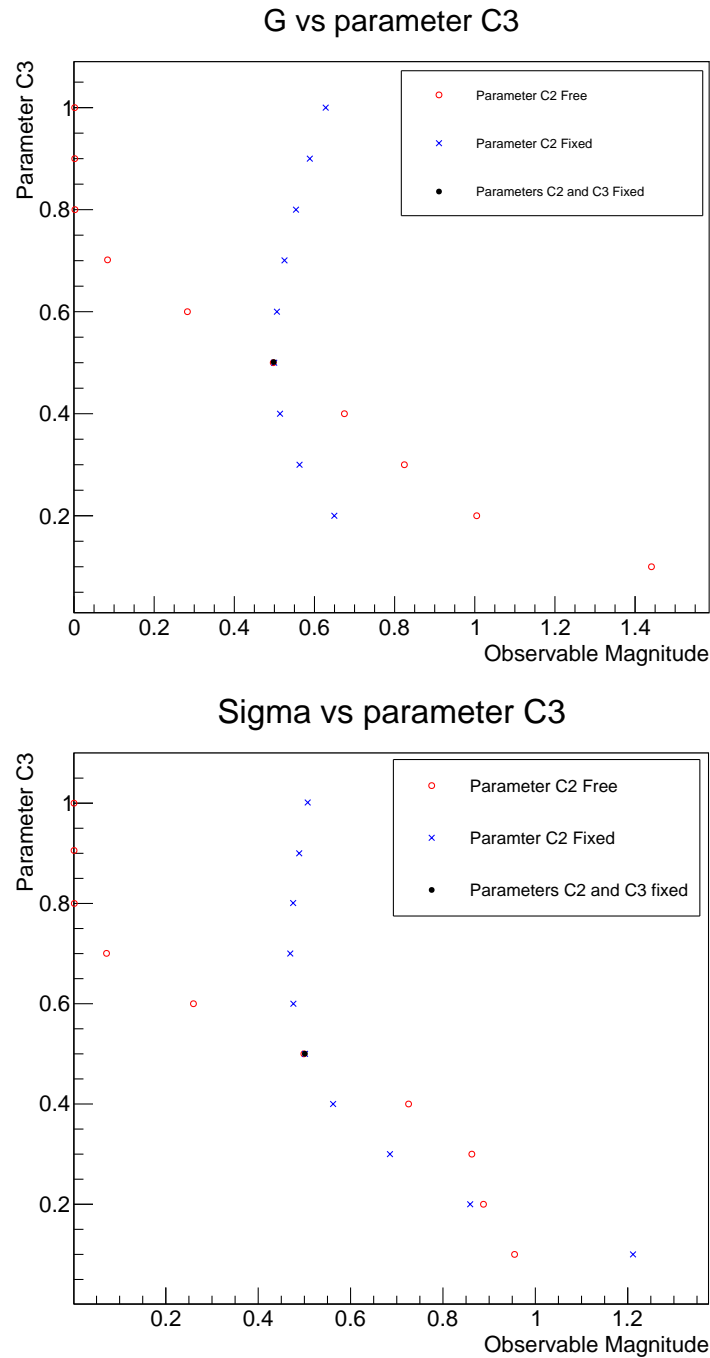


Figure 7.5: Changes of extracted polarisation observable magnitudes by varying parameter  $C_3$ . Blue points are where parameter  $C_2$  is fixed and red points are where parameter  $C_2$  is left free. Observable magnitudes closely match the input values used in generating the toy data when both  $C_2$  and  $C_3$  are fixed to their respective input values (black points).

The fit values of  $\Sigma$  and  $G$  converge on their respective input values as parameters  $C_2$  and  $C_3$  approach their respective input values, as in Figures 7.4 and 7.5. When

the polarisation and flux ratios are fixed to their known values, which are measured independently in data taking, the extracted observable values are closest to their input values. This demonstrates the fit works best when the ratio parameters are fixed. The plots show that the function has greater sensitivity to the linear polarisation ratio ( $C_3$ ) than the ratio of fluxes ( $C_2$ ), as shown by the larger variation of extracted observable values in Figure 7.5. To demonstrate the accuracy of the fit, pull distributions were used to compare output and input values of the polarisation observables.

### Pull distributions

A test of the reliability and measure of the systematics relating to a measurement can be done using a pull distribution [111]. In general a pull distribution can be written as

$$\text{Pull} = \frac{x - \mu}{\sigma} \quad (7.9)$$

where  $x$  is the measured variable,  $\mu$  is the mean of the distribution and  $\sigma$  is the width. This will be a Gaussian distribution with a mean of zero and width of one if there are no systematic effects present. Producing a pull distribution of a measured variable indicates any systematic effects in that measurement, through deviations from the normal pull distribution values. Where the width is less than one the errors on that measurement are overestimated, if greater than one then they are underestimated. A deviation in the mean position from zero indicates the systematic error on the measurement. Extending the above general case to the extraction of polarisation observables using the function in Equation 7.8 a pull distribution equation can be written for the two observables extracted as

$$\Sigma_{diff} = \frac{\Sigma_{Fit} - \Sigma_{Input}}{\Sigma_{FitError}} \quad (7.10)$$

$$G_{diff} = \frac{G_{Fit} - G_{Input}}{G_{FitError}} \quad (7.11)$$

where  $\Sigma_{Input}$  and  $G_{Input}$  are the input values used in generating the initial  $\phi$  distributions. The distributions of these measurements are shown for both positive and negative target polarisation settings, in Figure 7.6.

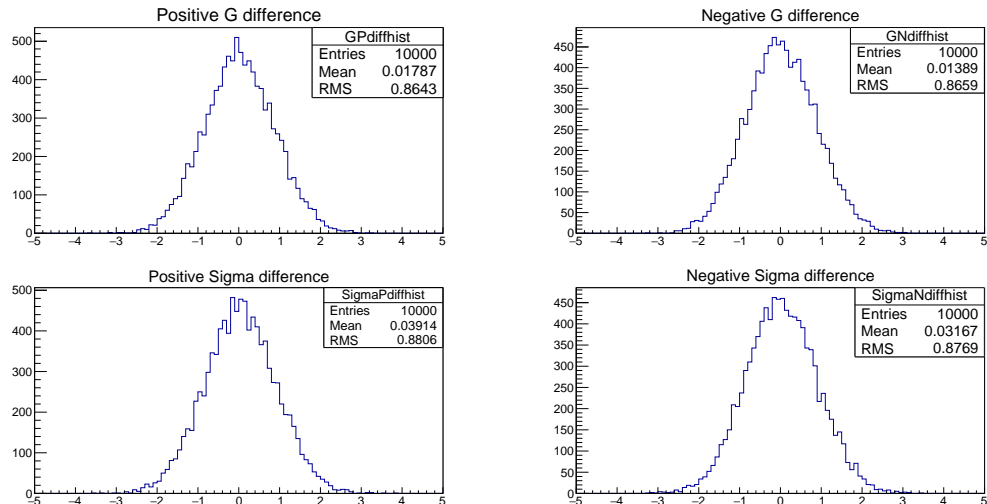


Figure 7.6: Difference between extracted observables and input values used to generate toy azimuthal distributions. Expect mean values of around 0 with values of  $\sigma$  around 1 to show that function works well. Mean values consistently close to 0 with the  $\sigma$  values around 0.9, showing the function consistently extracts the observables accurately but perhaps slightly overestimates the errors.

It can be seen that in the extraction of both  $\Sigma$  and  $G$  there are no major systematic effects from the function itself. The  $\sigma$  values of each distribution indicate that the errors in these measurements are being slightly overestimated, as their values are consistently around 0.9.

#### 7.1.4 $\phi_0$ determination

A phase offset,  $\phi_0$ , in the asymmetries is present due to the diamond orientation having a small angular offset. The small offset results in the nominal photon polarisation planes of  $\pm 45$  not aligning exactly with their stated orientations.

The measurement of the offset is made over all kinematic bins as the orientation is fixed for all energies and polar angles ( $\theta$ ) throughout the experiment. The measurement was made using data from a carbon target which reduces any systematic effects using the polarised Butanol which would require scaling and summing over target

polarisation states. The summing over target states would cancel the effects of the G observable on the asymmetries as it manifests itself as an additional phase shift in the parallel and perpendicular  $\phi$  distributions. Using an unpolarised carbon target requires only a single additional term added to the  $\cos(2\phi)$  fit to the asymmetry as it has no added phase shifts from the G observable.

Using the carbon target and fitting over all kinematic bins the  $\phi_0$  offset angle was determined to be  $44.3^\circ$ . With the offset determined it was included in the fit function as a fixed parameter to fit the binned asymmetries and extract the polarisation observables.

### 7.1.5 Data Asymmetries

The  $\Sigma$  and G observables vary as a function of incident photon energy,  $\pi^0$  centre of mass angle and  $\theta_{CM}$ . Asymmetries were created for kinematic bins and defined by their ranges in these variables. They were then fit to extract a value for  $\Sigma$  and G in each bin. Figure 7.7 shows examples of asymmetry fits over the  $\cos\theta$  range, for photon energy  $403 < E_\gamma < 436$  MeV, from which both  $\Sigma$  and G were extracted. Note that at the forward angles ( $\cos\theta > 0.3$ ) the acceptance decreases due to the proton having insufficient energy to escape the target and be detected in the CB. This results in fewer statistics and poorer asymmetries. The free parameters in the fit, shown in the statistics box, were  $P_L\Sigma$  and  $P_LP^TG$ .

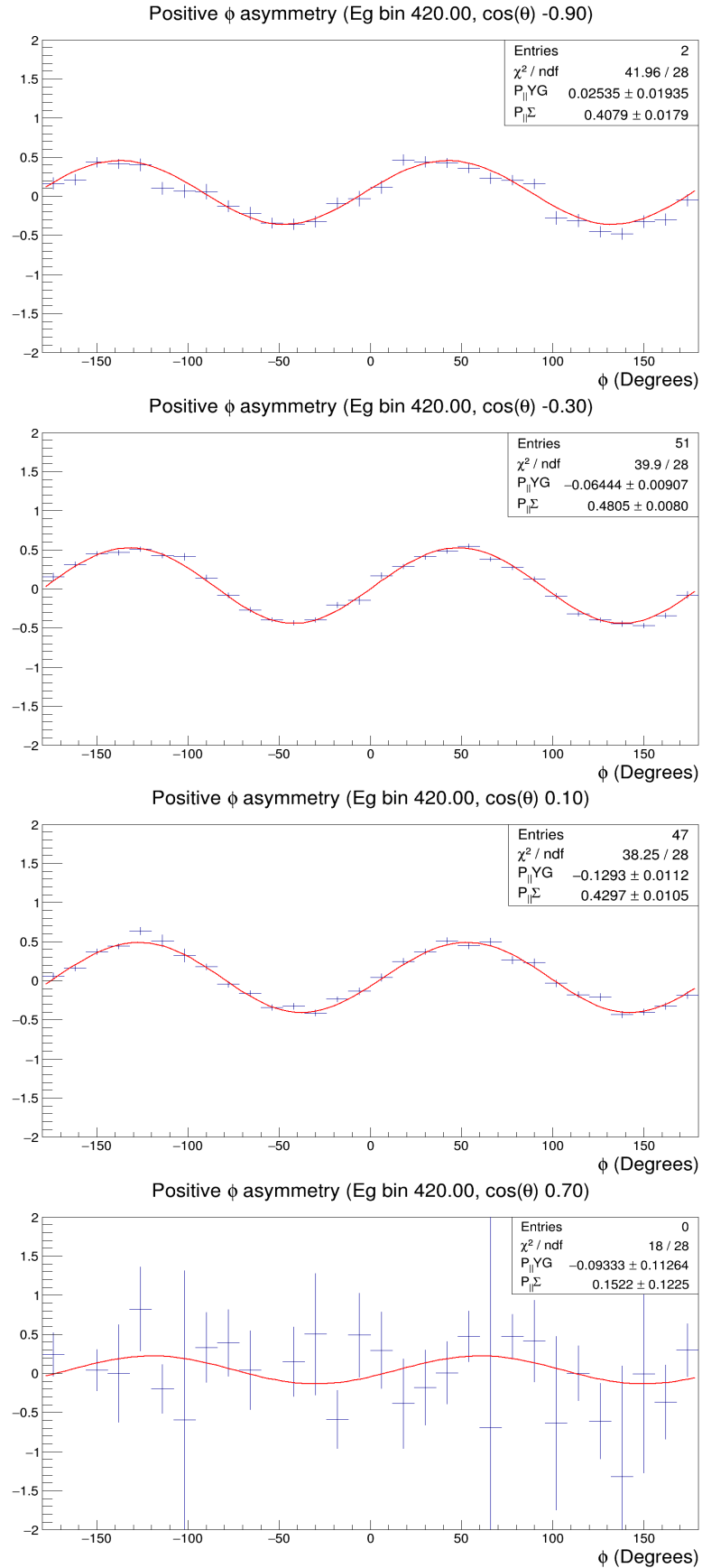


Figure 7.7: Example fits to data asymmetries to extract  $\Sigma$  and  $G$  for positive target polarisation,  $-0.4 > \cos\theta > -0.2$  and  $436 < E_{\gamma} < 469$  MeV.

# Chapter 8

## Results

In this chapter the results for the polarisation observables  $\Sigma$  and  $G$  in the reaction  $\gamma p \rightarrow p \pi^0$  are presented. Predictions from partial wave analysis models, MAID [76], SAID [79] and Bonn-Gatchina [81], are shown alongside the results where deviations from the prediction indicate areas where models may be improved by the new data. The results are presented having used the  $s\mathcal{P}$ lots fitting technique to extract the signal using three separate discriminating variables (Section 6.4). The results from these different fits are compared and give an indication of the systematic uncertainty in the background subtraction procedure.

Section 8.1 presents the  $\Sigma$  observable measurements while the double polarisation observable  $G$  is given in Section 8.3. Discussion of the measurements is given in Section 8.2 for  $\Sigma$  and Section 8.6 for  $G$ , with the systematic uncertainties on these measurements discussed in Section 8.5.

### 8.1 $\Sigma$ Results

The polarisation observable  $\Sigma$  has been measured as a function of photon energy and  $\cos\theta_{CM}$ . The results are binned in 33 MeV photon energy bins and 10 equally spaced  $\cos\theta$  bins between  $-1 < \cos\theta < 1$ . The results have been produced for both target polarisation directions. The  $\Sigma$  measurements with the different  $s\mathcal{P}$ lot methods using

proton opening angle difference, missing mass and coplanarity of the  $\pi^0$  and proton have been plotted together in Figures 8.1 and 8.2 for positive and negative target states respectively. Figure 8.3 shows the positive and negative target polarisation values for  $\Sigma$ . The average of the target polarisations for  $\Sigma$  is shown in Figure 8.4.

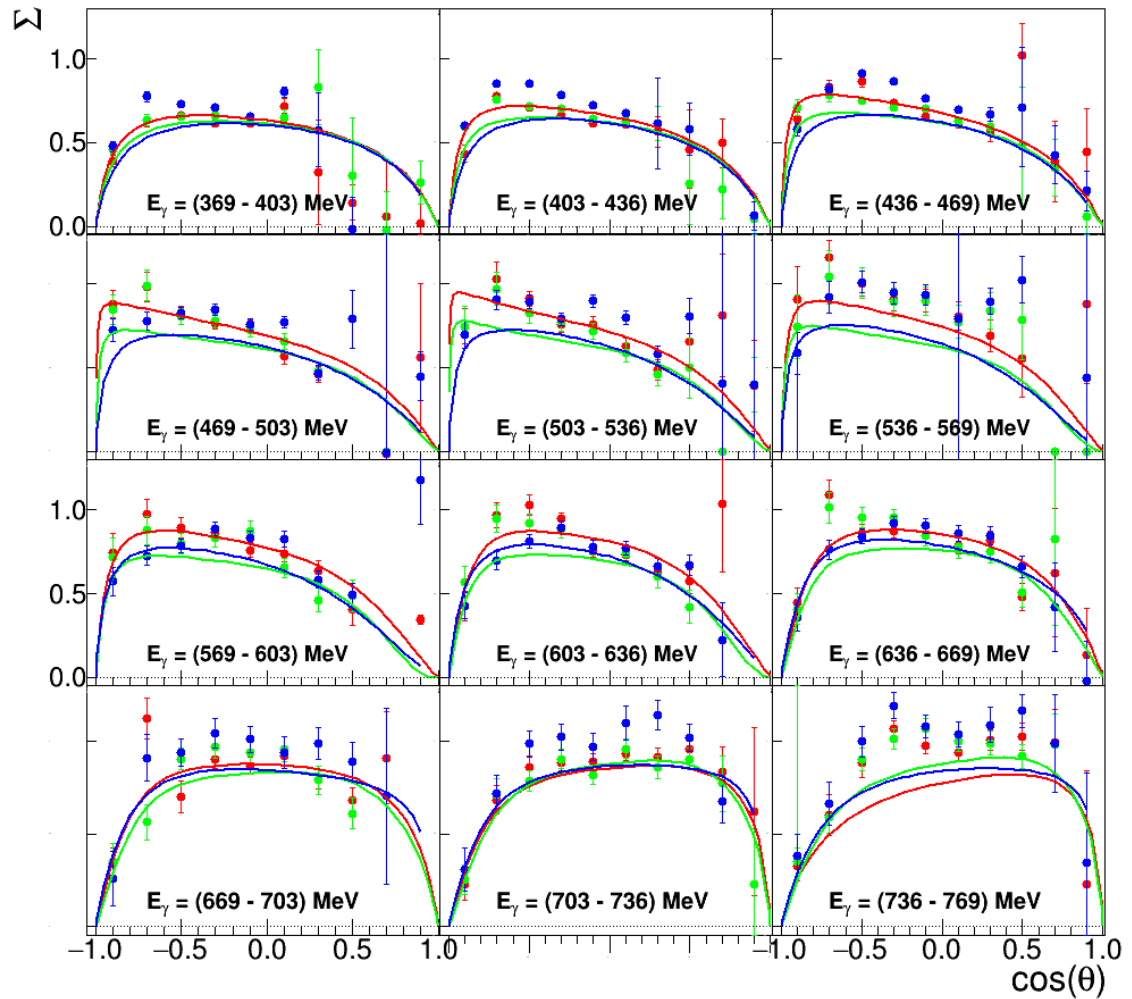


Figure 8.1: Photon asymmetry  $\Sigma$  as a function of  $\cos\theta$ . The results are presented for data using a positive target polarisation. The results from each  $s\mathcal{P}$ lot method are shown with proton opening angle results (red), coplanarity (green) and missing mass (blue). The photon energy range of each plot is shown in the center at the bottom. The PWA predictions are shown as coloured lines: MAID [71] (red), SAID [72] (green) and Bonn-Gatchina [73] (blue).

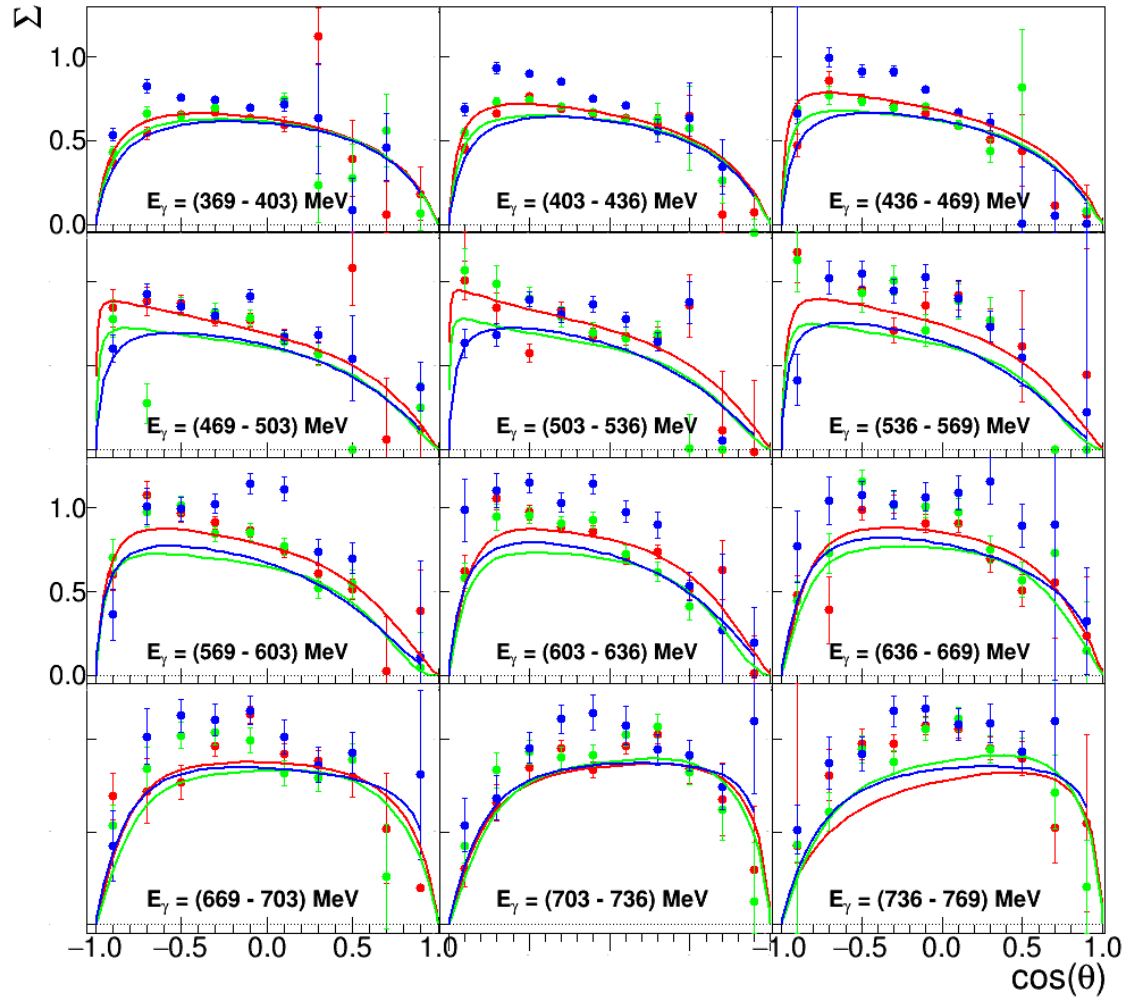


Figure 8.2: Photon asymmetry  $\Sigma$  as a function of  $\cos\theta$ . The results are presented for data using a negative target polarisation. The results from each  $s\mathcal{P}$ lot method are shown with proton opening angle results (red), coplanarity (green) and missing mass (blue). The photon energy range of each plot is shown in the center at the bottom. The PWA predictions are shown as coloured lines: MAID [71] (red), SAID [72] (green) and Bonn-Gatchina [73] (blue).

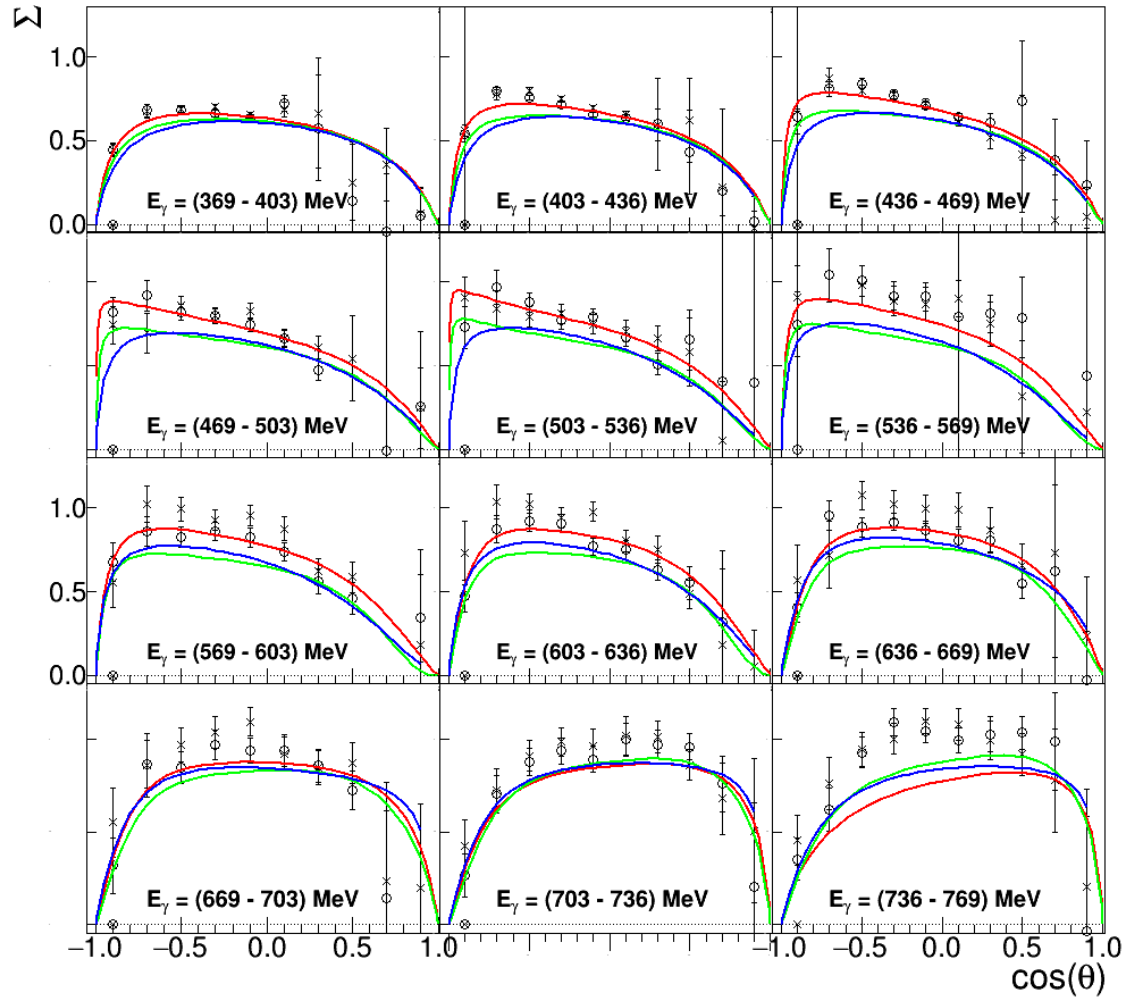


Figure 8.3: Polarisation observable  $\Sigma$  as a function of  $\cos\theta$ . The results are presented for the coplanarity  $s\mathcal{P}$ Plot subtraction method, with positive (Open circles) and negative (Crosses) target polarisation states. The photon energy range of each plot is shown in the center at the bottom. The PWA predictions are shown as coloured lines: MAID [71] (red), SAID [72] (green) and Bonn-Gatchina [73] (blue).

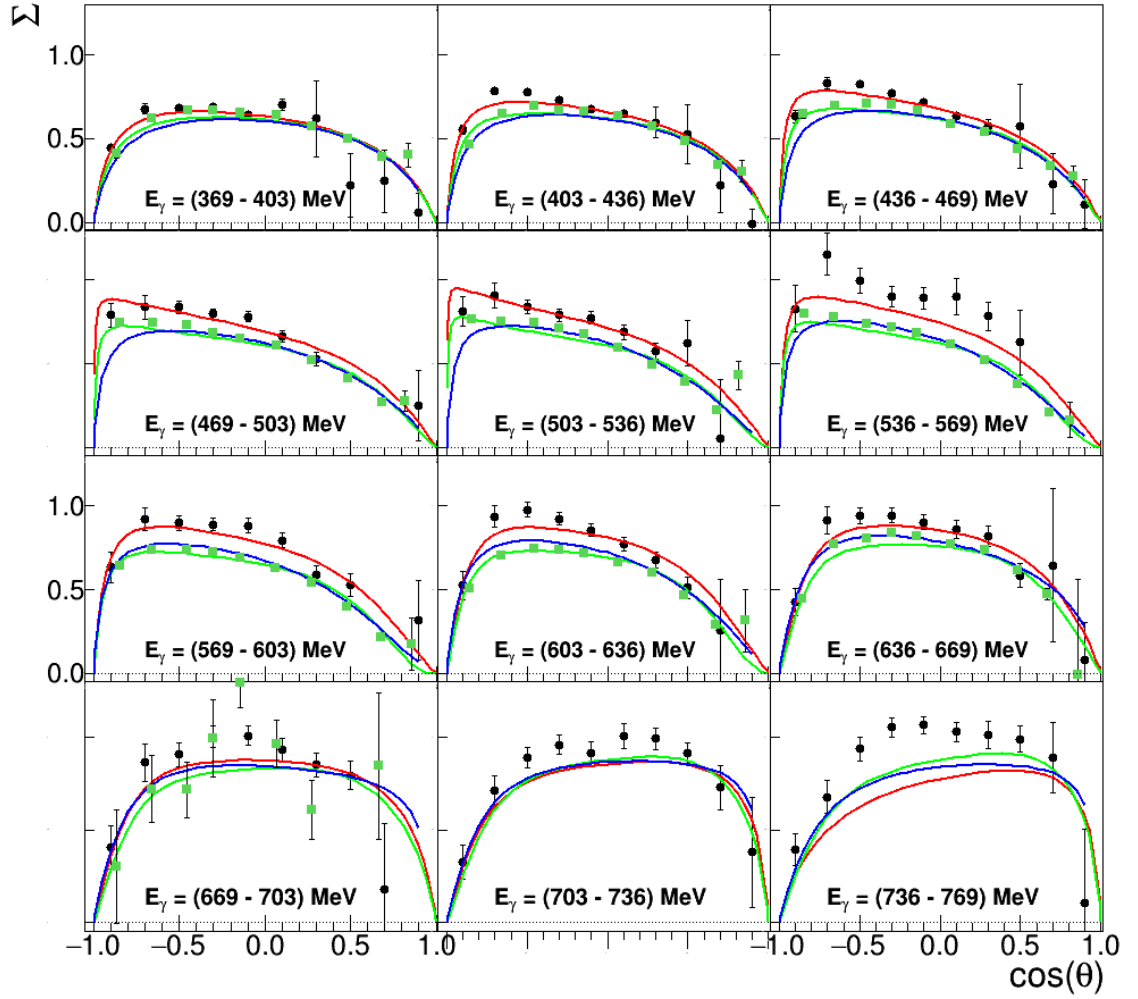


Figure 8.4: Photon asymmetry  $\Sigma$  as a function of  $\cos\theta$ . The results averaged over the target polarisations, having used the coplanarity  $s\mathcal{P}$ Plot subtraction method, are shown and compared to the latest published  $\Sigma$  measurements by Gardner et al. [70]. The photon energy range of each plot is shown in the center at the bottom. The PWA predictions are shown as coloured lines: MAID [71] (red), SAID [72] (green) and Bonn-Gatchina [73] (blue).

## 8.2 $\Sigma$ Results Discussion

The  $\Sigma$  results are in general agreement with previous measurements at lower energy bins and follow the trend of the PWA predictions, appearing to favour the MAID PWA generally. The results from different  $s\mathcal{P}$ Plot fits are consistent with one another, demonstrating the consistency of the technique in extraction of the signal. There is a systematic positive shift in the results which appears to increase as the energy

increases. As the  $\Sigma$  observable is a secondary observable measurement, and as it has been measured precisely in the energy region of this work, it can be used as a polarimeter to correct the measurements for this systematic shift.

Further analysis and systematic study (Section 8.5) will consolidate the measurements of the  $\Sigma$  polarisation observable and determine any discrepancies between the different extracted results and previous measurements.

The final results for  $\Sigma$  shown in Figure 8.4 combine the data from both target states from the coplanarity  $s\mathcal{P}$ lot subtraction method. The results from this method were chosen due to their better agreement with previous measurements compared to the other subtraction methods. The different target settings are two different data sets, so to combine them a weighted mean is calculated using Equation 8.1, with errors calculated using Equation 8.2.

$$\bar{x} = \frac{\sum_{i=1}^n (x_i \sigma_i^{-2})}{\sum_{i=1}^n \sigma_i^{-2}} \quad (8.1)$$

$$\sigma_{\bar{x}} = \sqrt{\frac{1}{\sum_{i=1}^n \sigma_i^{-2}}} \quad (8.2)$$

where  $\bar{x}$  is the weighted mean value of the different target states and  $\sigma_{\bar{x}}$  is the error associated with this value. A systematic positive shift in results can be seen, particularly for higher energy bins. The comparison to the most recent, and most precise, measurements of  $\Sigma$  by Gardner et al. [70] allows a correction factor to be calculated in order to account for the systematic shift in  $\Sigma$  (Section 8.4). The systematic shift suggests that the linear polarisation is being systematically underestimated, increasing with energy. It also suggests that there may be effects of background reaction channels present which are not currently accounted for. This is discussed further in Section 8.5.

Compared to the previous measurements the current extraction of  $\Sigma$  includes a greater background dilution due to the carbon/oxygen background from the polarised target, and so it is important to have a reliable subtraction method. As the

systematics of the subtraction methods are the same for  $\Sigma$  as for G that implies the subtraction is also working at a satisfactory level for the G observable. Due to the same systematic effects on both polarisation observables a correction factor calculated from  $\Sigma$  measurements also applies to the G observable measurements.

### 8.3 G Results

The double polarisation observable G has been measured as a function of photon energy and  $\cos\theta_{CM}$ . The results are binned in 33 MeV photon energy bins and 10 equally spaced  $\cos\theta$  bins:  $-1 < \cos\theta < 1$ . The results have been produced using different target polarisation directions. Figures 8.5 and 8.6 show the G results for positive and negative target states respectively. The results from fits to proton opening angle difference, missing mass and coplanarity of the  $\pi^0$  and proton have been overlaid showing general consistency between background subtraction methods. Figure 8.7 shows the positive and negative target polarisation values for G. Figure 8.8 shows the average of the two target states for G over the full kinematic range.

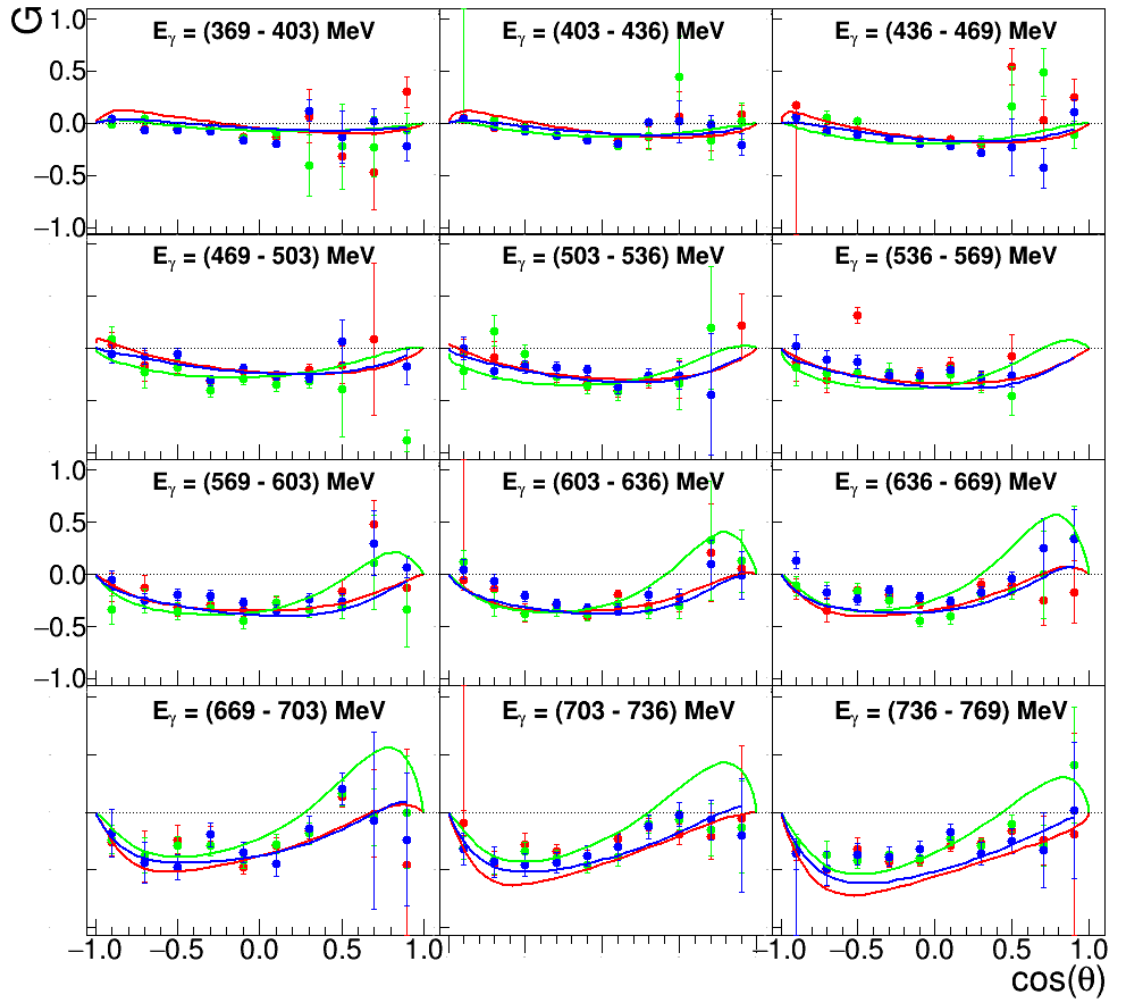


Figure 8.5: Polarisation observable  $G$  as a function of  $\cos\theta$ . The results are presented for data using a positive target polarisation. The results from each  $sP$ Plot method are shown with proton opening angle results (red), coplanarity (green) and missing mass (blue). The photon energy range of each plot is shown in the center at the top. The PWA predictions are shown as coloured lines: MAID [71] (red), SAID [72] (green) and Bonn-Gatchina [73] (blue).

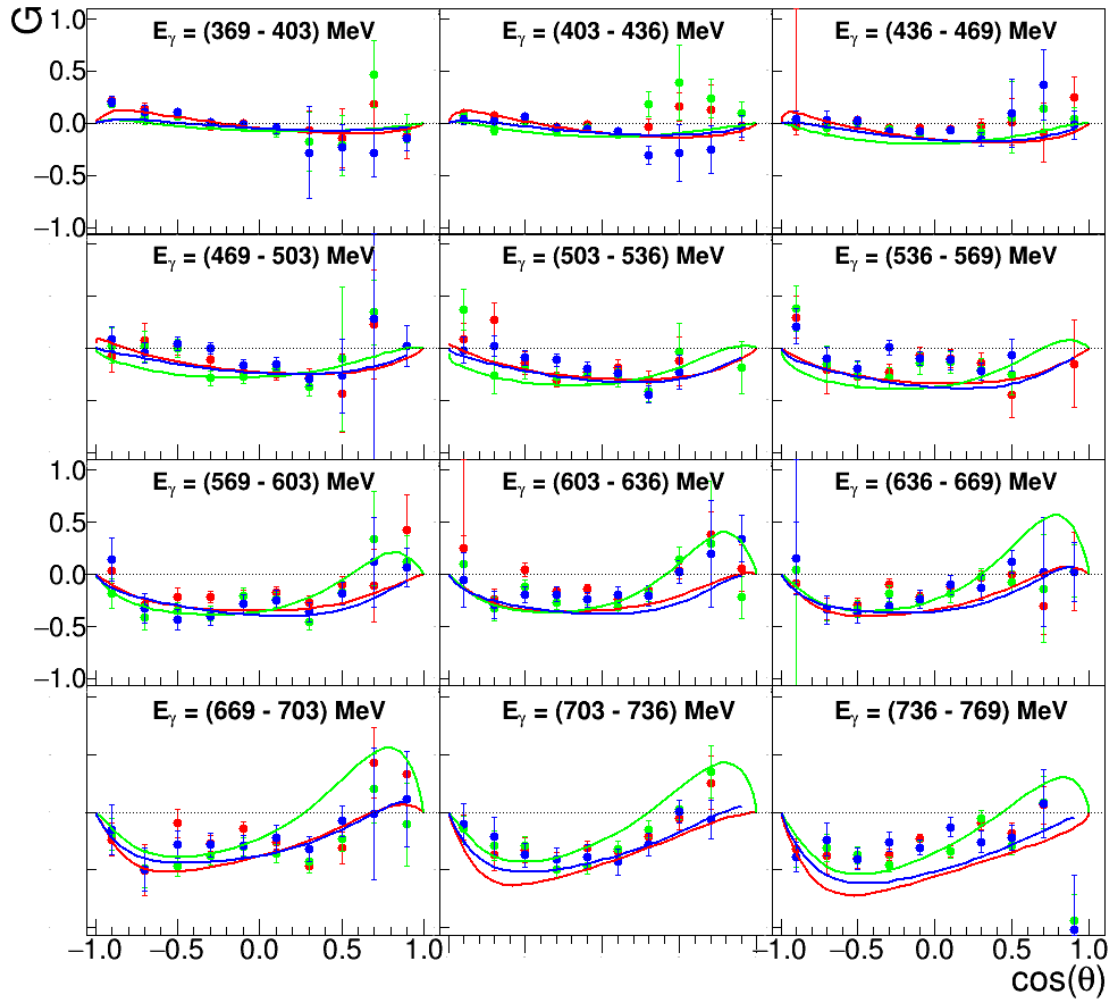


Figure 8.6: Polarisation observable  $G$  as a function of  $\cos\theta$ . The results are presented for data using a negative target polarisation. The results from each  $sP$ lot method are shown with proton opening angle results (red), coplanarity (green) and missing mass (blue). The photon energy range of each plot is shown in the center at the top. The PWA predictions are shown as coloured lines: MAID [71] (red), SAID [72] (green) and Bonn-Gatchina [73] (blue).

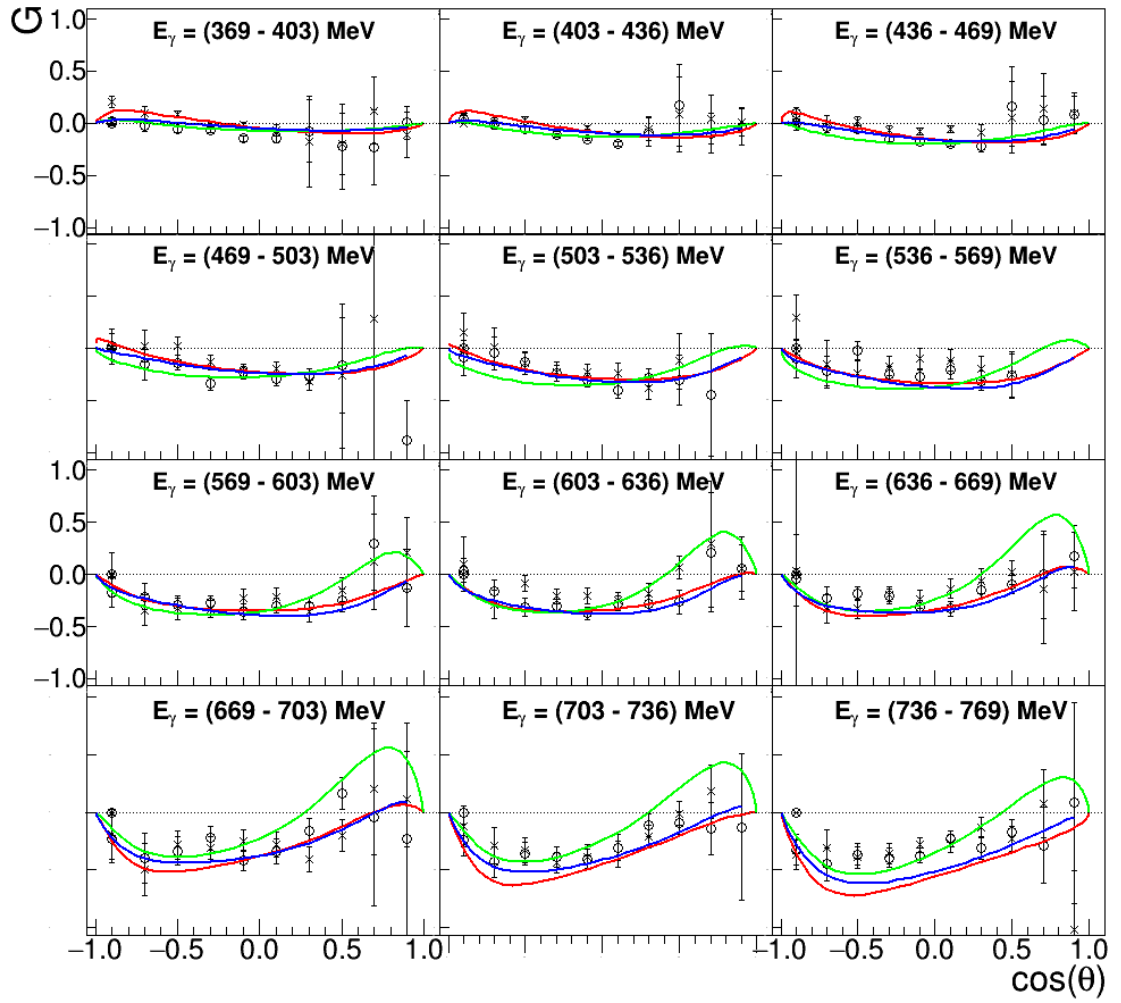


Figure 8.7: Polarisation observable  $G$  as a function of  $\cos\theta$ . The results are presented for the coplanarity  $s\mathcal{P}$ Plot subtraction method, with positive (Open circles) and negative (Crosses) target polarisation states. The photon energy range of each plot is shown in the center at the top. The PWA predictions are shown as coloured lines: MAID [71] (red), SAID [72] (green) and Bonn-Gatchina [73] (blue).

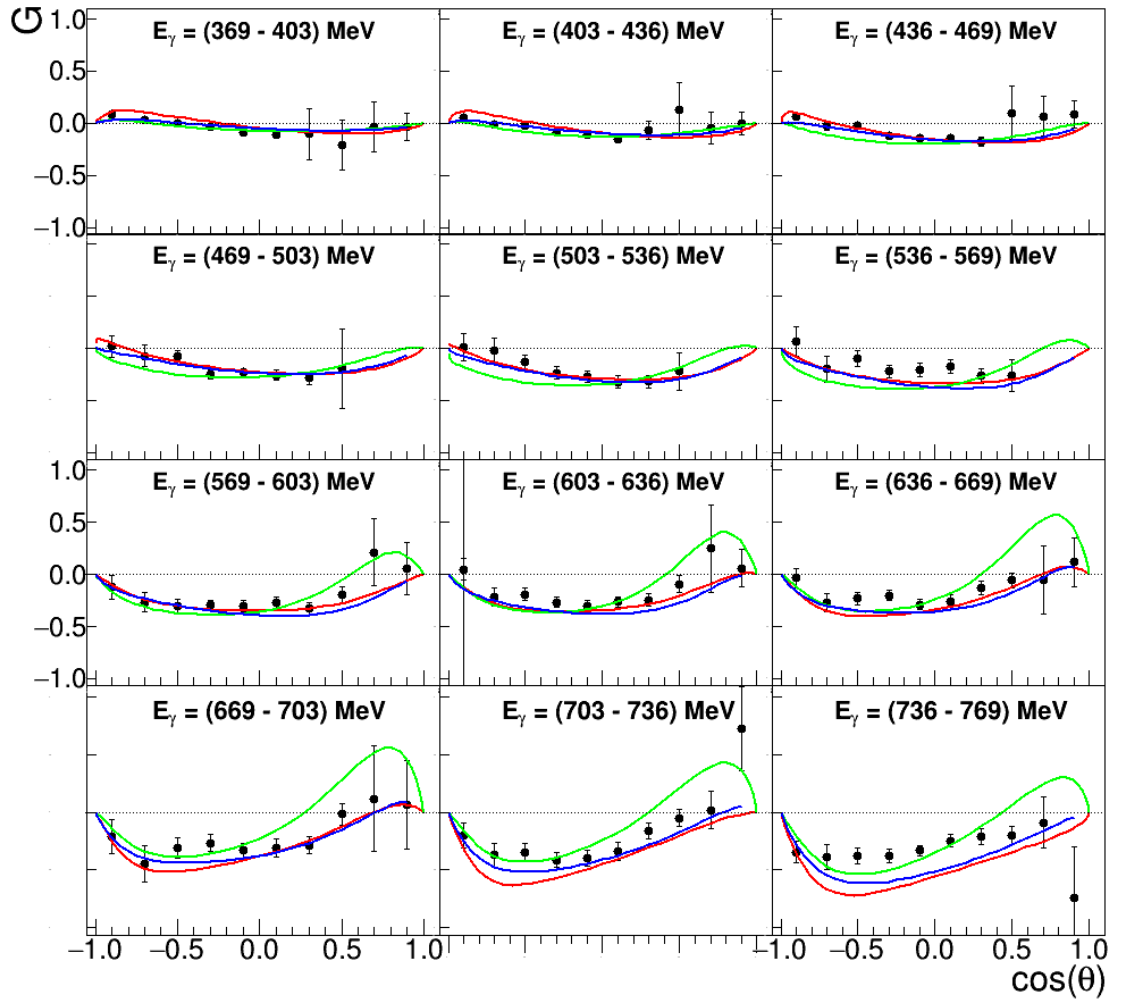


Figure 8.8: Polarisation observable  $G$  as a function of  $\cos\theta$ . The results are presented for a data set which combines the data from positive and negative target polarisations. The  $s\mathcal{P}$ Plot method was used to fit the coplanarity distribution, apply the relevant weights to the data, and extract the signal. The photon energy range of each plot is shown in the center at the top. The PWA predictions are shown as coloured lines: MAID [71] (red), SAID [72] (green) and Bonn-Gatchina [73] (blue).

## 8.4 Correction Factor

The systematic shift in the  $\Sigma$  measurements were corrected by using the most recent measurements and the SAID partial wave curve as a polarimeter. A correction factor was calculated, shown in Figure 8.9, for each energy bin by taking the weighted average of the ratios between the  $\Sigma$  results of this work and the previous measurements shown in Figure 8.4. The ratios are weighted by the size of the error bars on the measurement.

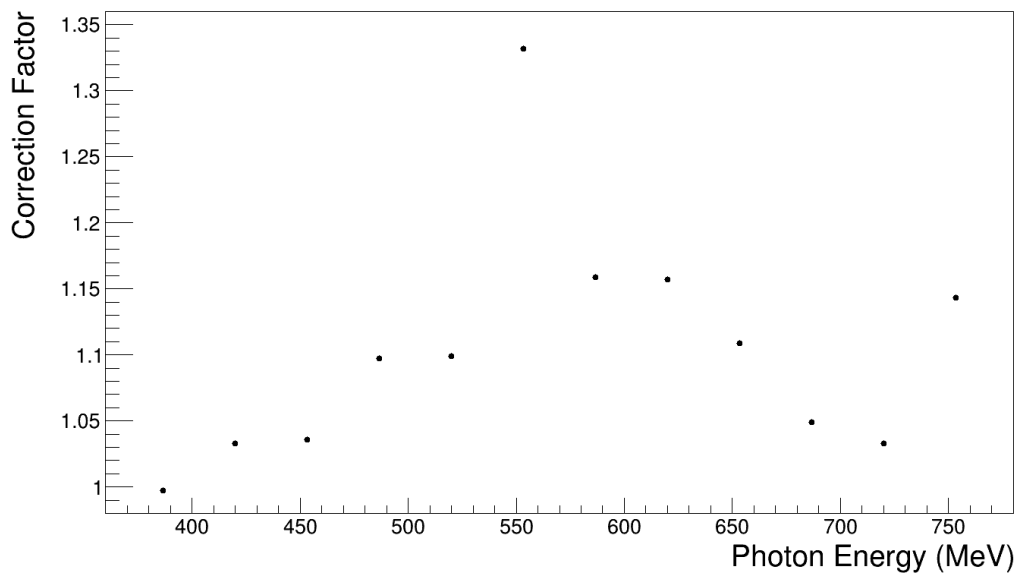


Figure 8.9: Correction factor as a function of energy. The correction factor was calculated using the previous measurements by Gardner et al. [1] and the SAID partial wave curve as a polarimeter.

The correction factor normalises the  $\Sigma$  measurements to correct for the systematic shift seen in Figure 8.4. These results now show excellent agreement with the previous measurements and the PWA curves, appearing to favour the SAID and Bonn-Gatchina curves. The correction factor shows there is a systematic error associated with the linear polarisation and with effects due to other reaction channels passing threshold. At 550 MeV and 750 MeV the correction factors are larger because they are calculated for energy bins across the coherent edge region. These coherent edges also correspond to the energy regions around the  $\eta$  and double  $\pi$  thresholds and

where their cross sections become significant (Figure 2.2). The coherent edge has larger systematic uncertainties, which can be seen in Figure 8.4. The systematics of the linear polarisation have been investigated and have been shown to be 8% (Section 8.5). However, these systematic effects do not fully explain the source of the systematic error. The experimental collaboration is continuing investigations into understanding why the discrepancy between the results of this work and previous measurements is so large.

The correction factor is also applied to the G results in Figure 8.8 as the systematics are the same for both polarisation observables. The correction factor normalises the G results for the systematic shift seen in the  $\Sigma$  results. The G results show good agreement with the PWA curves throughout the kinematic range, particularly with the MAID and SAID curves at lower energies and backward angles.

Figures 8.10 and 8.11 show the corrected  $\Sigma$  and G results respectively. The systematics on these results are discussed further in Section 8.5.

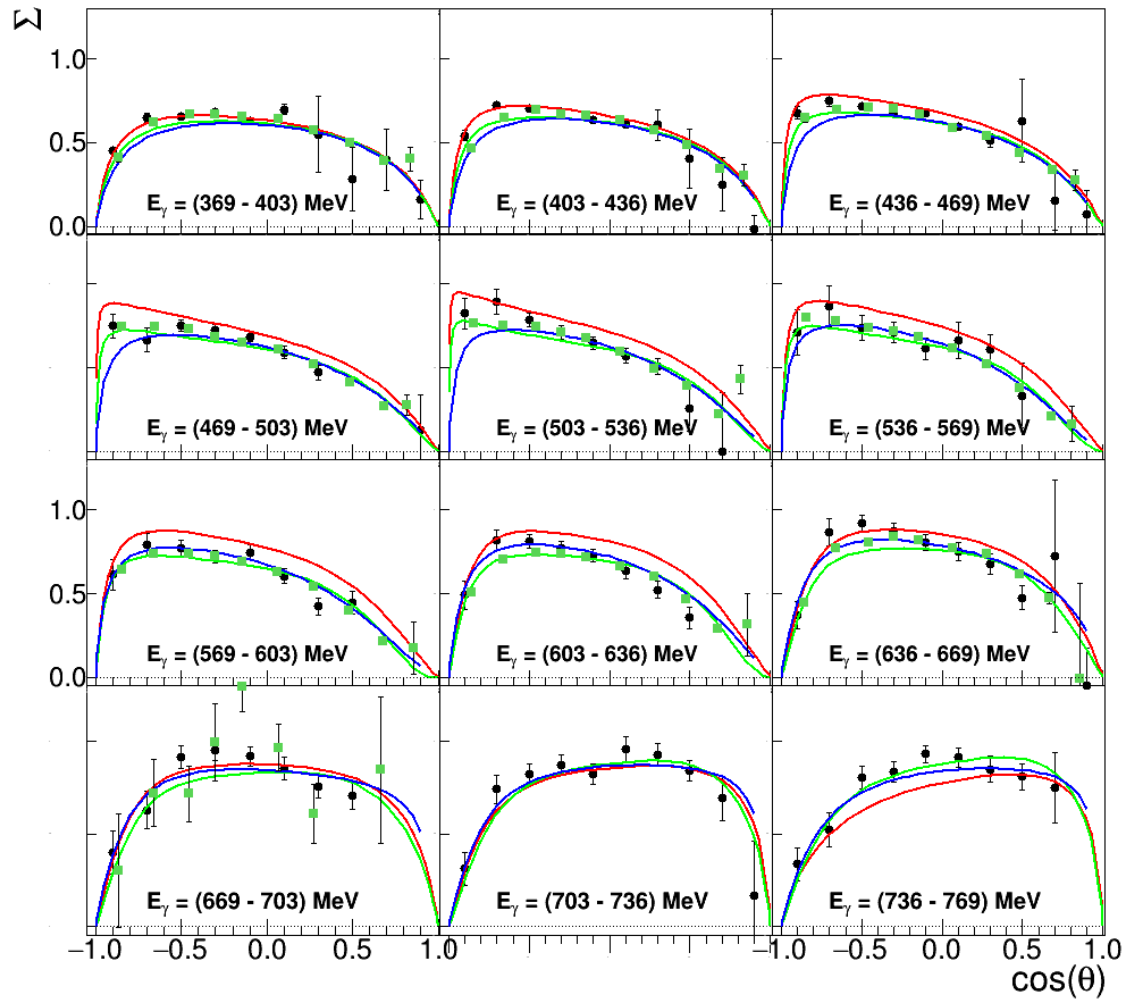


Figure 8.10: Polarisation observable  $G$  as a function of  $\cos\theta$ . The results are presented for a data set which combines the data from positive and negative target polarisations. The  $sPlots$  method was used to fit the opening angle of reconstructed and detected proton, apply the relevant weights to the data, and extract the signal. The photon energy range of each plot is shown in the center at the bottom. The PWA predictions are shown as coloured lines: MAID [71] (red), SAID [72] (green) and Bonn-Gatchina [73] (blue).

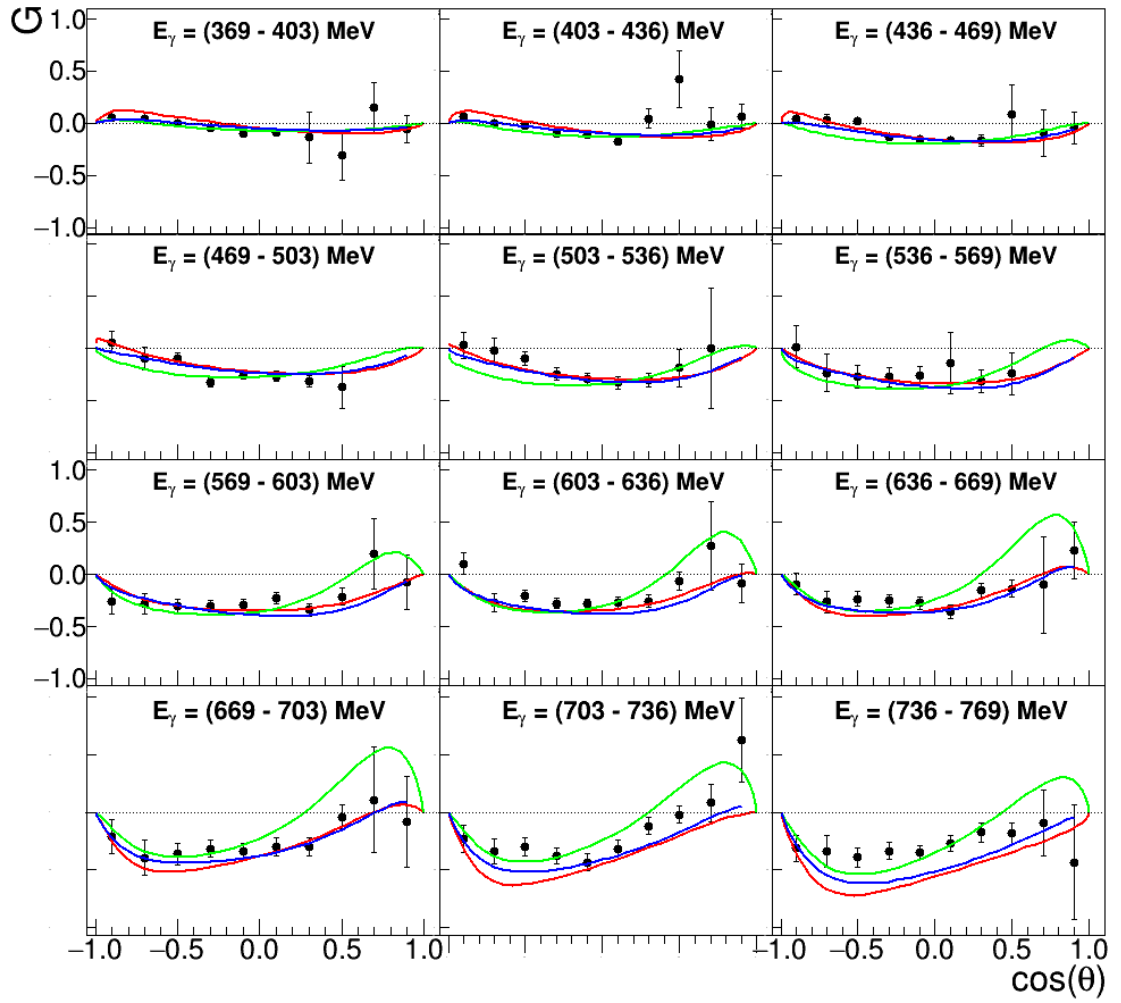


Figure 8.11: Polarisation observable  $G$  as a function of  $\cos\theta$ . The results are presented for a data set which combines the data from positive and negative target polarisations. The  $s\mathcal{P}$ lots method was used to fit the opening angle of reconstructed and detected proton, apply the relevant weights to the data, and extract the signal. The photon energy range of each plot is shown in the center at the bottom. The PWA predictions are shown as coloured lines: MAID [71] (red), SAID [72] (green) and Bonn-Gatchina [73] (blue).

## 8.5 Systematic Uncertainty

The total systematic uncertainty on the measurements presented in this thesis result from three main sources. These are the degree of linear polarisation, the subtraction of the background from the polarised target, and background reaction channels.

The calculated degree of polarisation is dependent on the enhancement spectra produced by dividing a bremsstrahlung spectrum from a diamond radiator with one from an amorphous radiator (Section 5.3). A baseline was chosen with which to normalise the spectrum before fitting. The choice in baseline is sensitive to the degree of linear polarisation extracted from the fit to the enhancement. In order to investigate the systematic effect of where this baseline is set it was manually fixed at  $\pm 10\%$  of the actual value and the degree of polarisation extracted for each baseline. The resulting polarisations are shown in Figure 8.12.

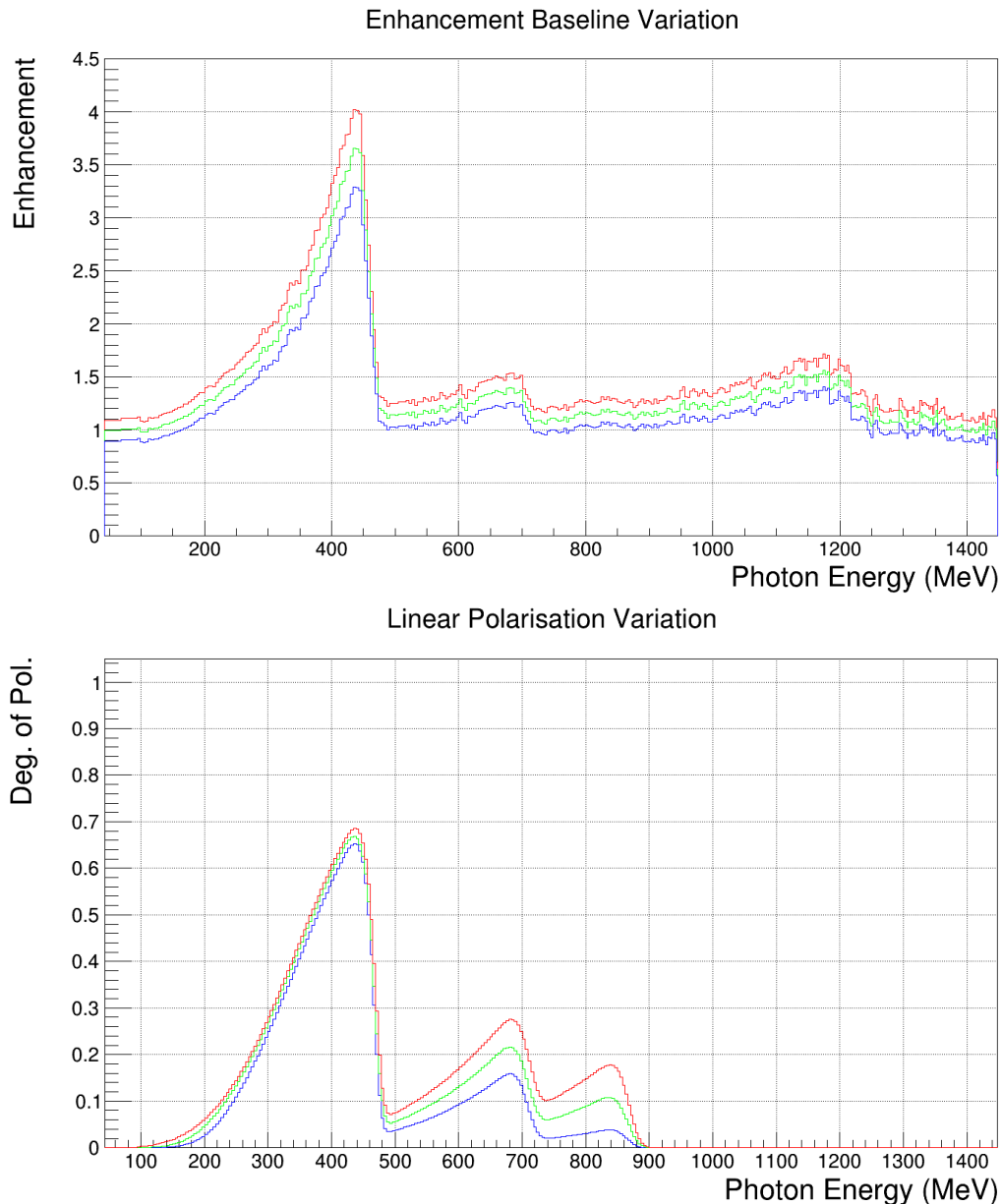


Figure 8.12: Top: The change in enhancement when altering the baseline by  $\pm 10\%$  from the original baseline. Bottom: The change in degree of polarisation when manually altering the baseline by  $\pm 10\%$  from the original baseline. The enhancement and degree of polarisation used in this work is shown in green, with the red curve showing an increase of 10% of the chosen baseline and the blue curve showing an decrease of 10%. A change of  $\pm 3\%$  in the degree of polarisation can be seen at the main peak (450 MeV), giving a 4% systematic uncertainty from the percentage difference.

At the peak position at 450 MeV the change in the degree of polarisation is  $\pm 3\%$  with a  $\pm 10\%$  change in baseline. The degree of uncertainty due to the choice in baseline is derived from the percentage change in the degree of polarisation. When

the coherent edge is at 450 MeV and the peak polarisation is 68% (Figure 8.12), the change of  $\pm 3\%$  in the degree of polarisation results in a percentage change of 4% at the peak.

As the fit to the enhancement calculates the relative degree of polarisation the change in baseline has a more pronounced effect in the degree of linear polarisation where the degree of polarisation is smaller. This can be seen in the secondary and tertiary peaks of the degree of linear polarisation in Figure 8.12, as well as in Figure 8.13.

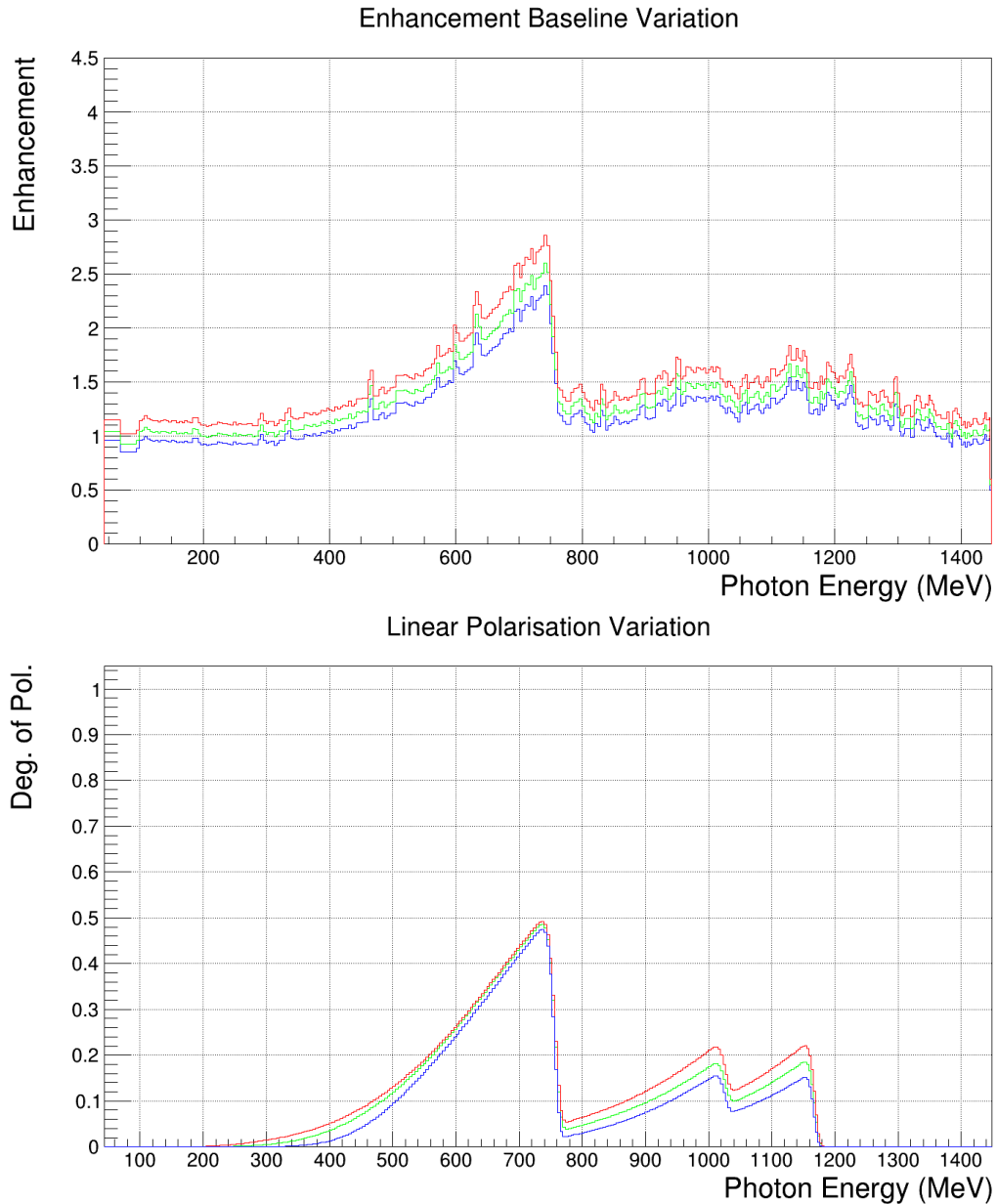


Figure 8.13: Top: The change in enhancement when altering the baseline by  $\pm 10\%$  from the original baseline. Bottom: The change in degree of polarisation when manually altering the baseline by  $\pm 10\%$  from the original baseline. The enhancement and degree of polarisation used in this work is shown in green, with the red curve showing an increase of 10% of the chosen baseline and the blue curve showing a decrease of 10%. A change of  $\pm 2\%$  in the degree of polarisation can be seen at the main peak (750 MeV), giving a 5% systematic uncertainty from the percentage difference.

The degree of linear polarisation generally decreases as the edge position increases in energy. This translates into a higher degree of systematic uncertainty in the linear polarisation at higher photon energies due to the choice of baseline. This

is clear from Figure 8.13 which shows a percentage change in the degree of linear polarisation of 5%, despite the variation in the degree of polarisation of only 2%. It is also clear from the results of this work to previous measurements and PWA curves in Figure 8.4. Using the previous  $\Sigma$  measurements, and Bonn-Gatchina PWA curve, as a polarimeter a correction factor has been calculated for each energy bin to correct for the systematic uncertainty in the linear polarisation (Section 8.4).

The changes in baseline were chosen as a reasonable degree of error in baseline choice, with a systematic error due to the choice of baseline in extracting the degree of linear polarisation taken in quadrature as 6.5%.

Another source of uncertainty relating to the degree of linear polarisation is the goodness of fit to the enhancement. An estimate of 3% is assigned to this based on the fits to the enhancements. The majority of enhancements are fit exceedingly well, with goodness of fit values generally less than 1.5, however there are a few where the peak is overestimated while the tail from the peak is underestimated (Figure 8.14).

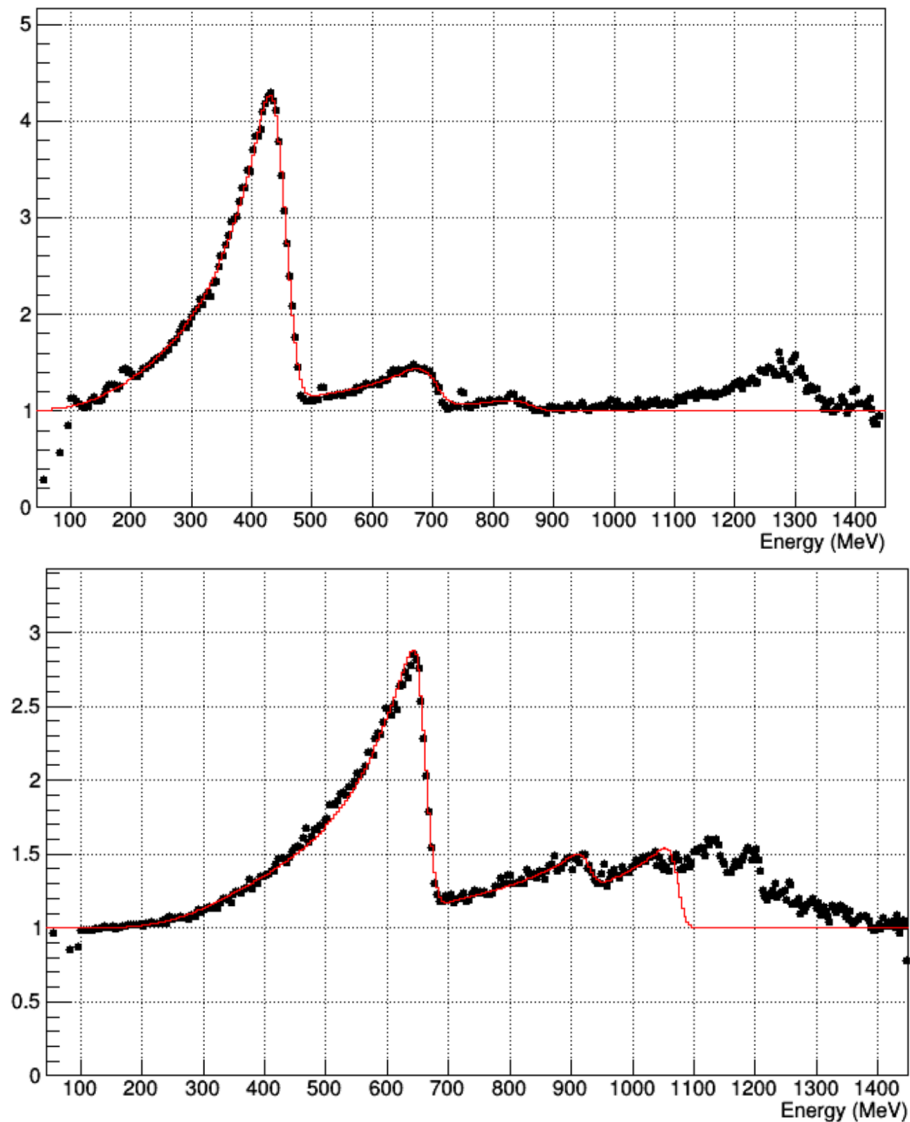


Figure 8.14: Examples of phenomenological fits to enhancement data. A systematic error associated with the goodness of fit is quoted at 3% based on the fits. The fit to the 650 MeV (bottom) coherent edge exhibits an overestimation in the degree of linear polarisation at the peak, and an underestimation half way down the tail to the left of the peak. The 450 MeV (top) fits the data well across the length of the main peak and tail.

Collaborators at the University of Bonn performed systematic checks of the linear polarisation [112] by varying the position of the measured coherent peak in the enhancement fits by  $\pm 1$  tagger channel, shown in Figure 8.15. This variation corresponds to a shift in tagged energy of around 4 MeV. A shift of 2 MeV is expected during normal experimental operation. The collaborators quote a systematic uncertainty of  $\sim 5\%$ .

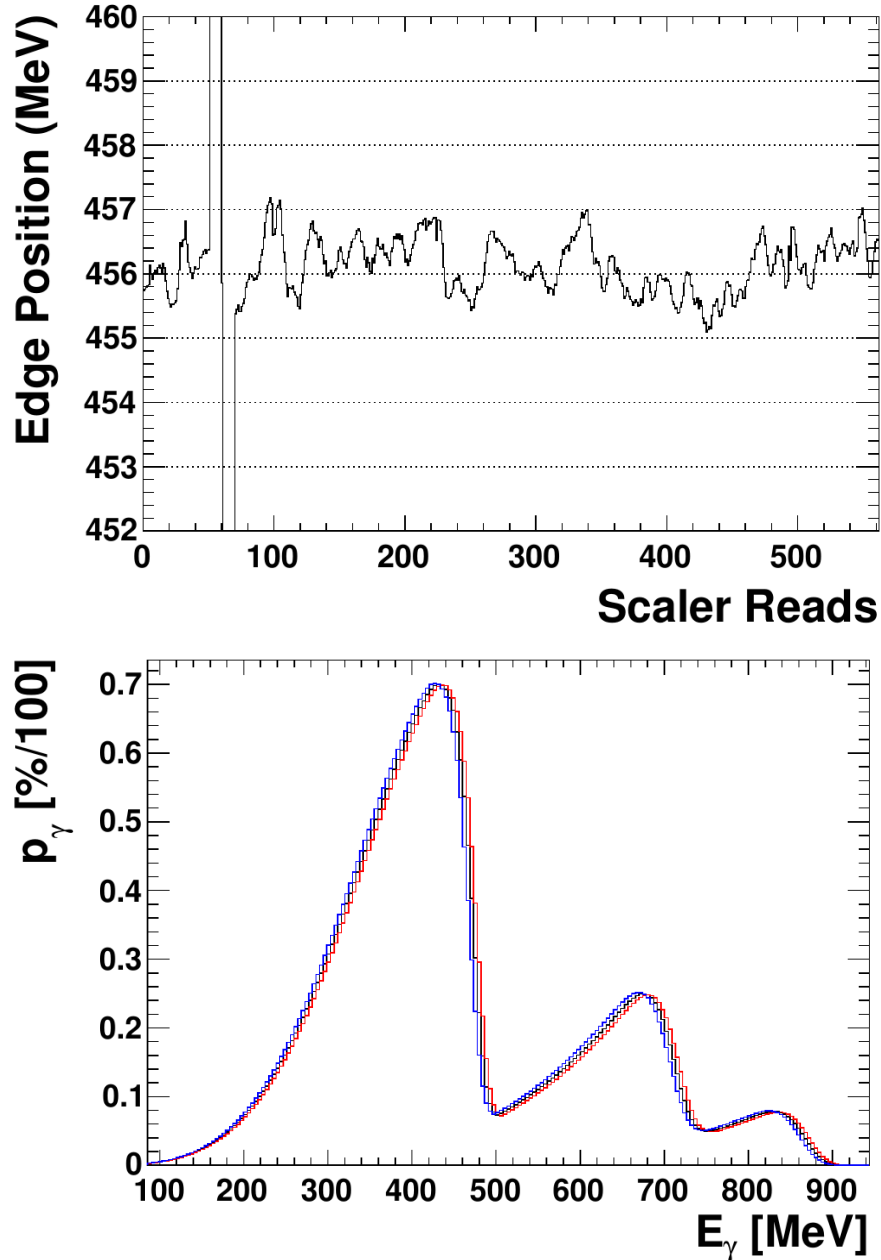


Figure 8.15: Systematic checks of linear polarisation degree performed by collaborators at Bonn by varying the measured coherent edge of the enhancement  $\pm 4$  MeV. Top: typical variation of the coherent edge over a singular experimental run. Bottom: Enhancements varying by  $-4$  MeV (blue),  $+4$  MeV (red) and original (black).

The spread in the edge position shown in Figure 8.15 is due to successive fits to the enhancement peak during the experiment. As the usual shift in the edge position is around 2 MeV the systematic error associated with the spread of the edge position is quoted as 2.5%.

Combining the different sources of error in the degree of linear polarisation in quadrature gives an estimated systematic uncertainty in the degree of linear polarisation of 8%.

### 8.5.1 Pull distributions

Pull distributions give indications on the systematic uncertainties and the consistency of a measurement. The formalism of pull distributions is covered in Section 7.1.3. This analysis considers the following as sources of systematic uncertainty:

1. Measurements of  $\Sigma$  and  $G$  between two different target polarisation states.
2. Measurements of  $\Sigma$  and  $G$  using different  $s\mathcal{P}$ lot variables to weight the data.

The pull distributions are constructed by comparing results for these different data sets over the full energy and  $\cos\theta$  range of measurements.

Figures 8.16 and 8.17 show the pull distributions for the different target polarisation settings for  $\Sigma$  and  $G$  respectively. The pull distributions for different target polarisation states are calculated using values obtained for one target setting compared to the average value between target polarisation states for each bin. Figures 8.18 - 8.20 show the pull distributions for the different  $s\mathcal{P}$ lot variables used when measuring  $\Sigma$ . Figures 8.21 - 8.23 show the pull distributions for the different  $s\mathcal{P}$ lot variables used when measuring  $G$ . In the case of the  $s\mathcal{P}$ lot pull distributions, the values obtained for  $\Sigma$  and  $G$  from each  $s\mathcal{P}$ lot method are compared to the average of the three individual measurements for each bin.

It is important to note that type 1, involves statistically independent datasets hence if there are no systematic deviations between the different target polarisation settings, the resulting pull distributions should be centred on zero with width one. On the other hand type 2 involves extracting observables from the same data. If the three subtraction methods were all perfect the pull distribution would be centred on zero with width zero. Deviations from zero width illustrate the systematic uncer-

tainty in the subtraction procedure. If the distribution is still centred on zero then that demonstrates the systematic uncertainties are unbiased or random. If the width is around one then that demonstrates the magnitude of the systematic uncertainty is of the same order as the statistical uncertainty.

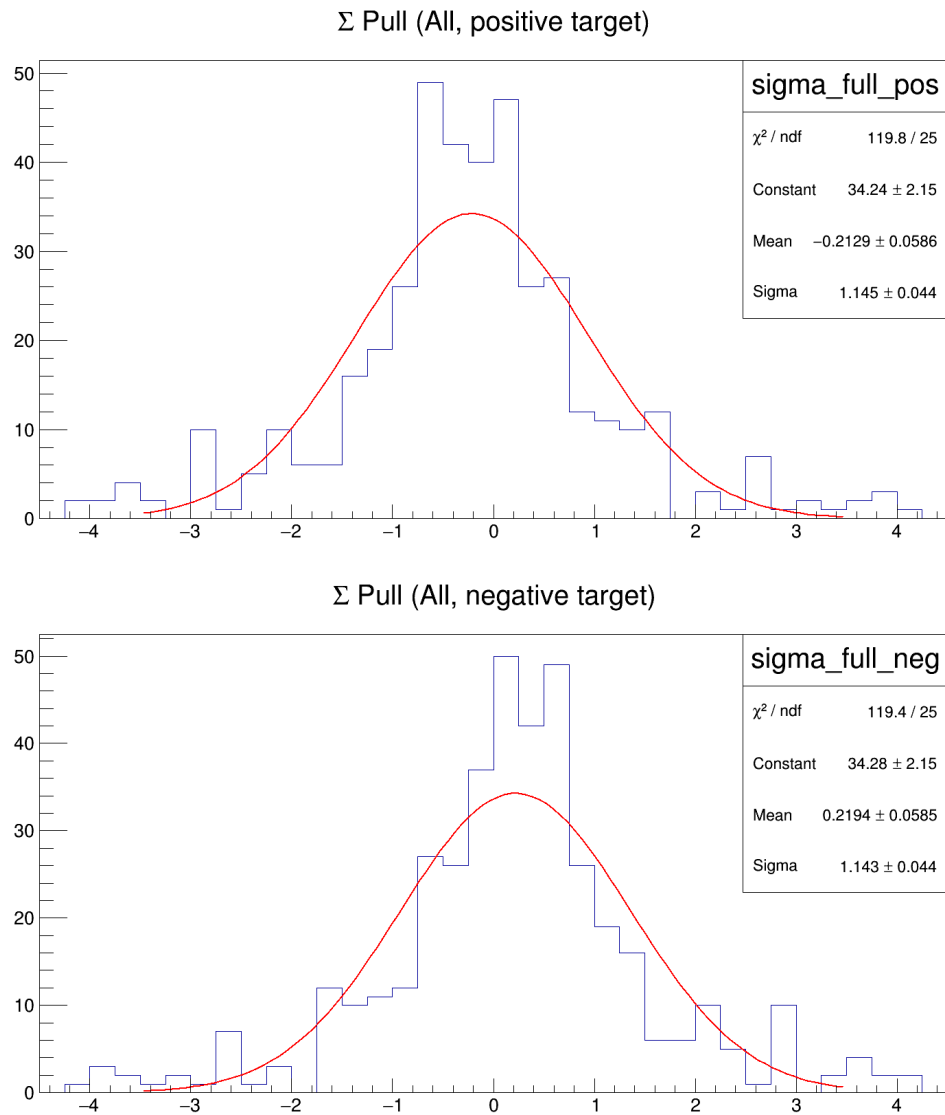


Figure 8.16:  $\Sigma$  pull distributions for two different target states. Positive and negative target states pull distributions are shown on the top and bottom respectively.

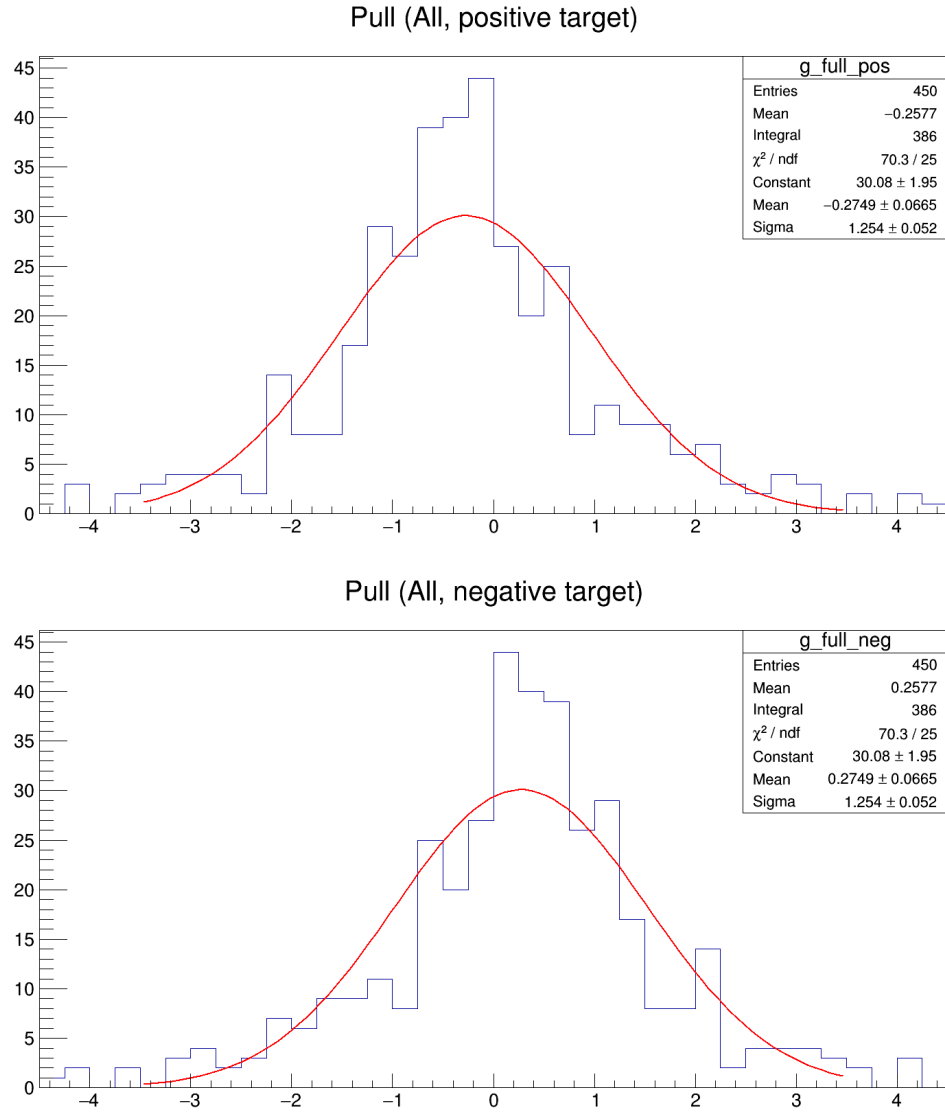


Figure 8.17: G pull distributions for two different target states. Positive and negative target states pull distributions are shown on the top and bottom respectively.

The pull distributions between different target states suggest that there is a systematic effect to consider. The mean values of the  $\Sigma$  measurements for each target state is  $\sim \pm 0.23$ , and is  $\pm 0.275$  for the target state measurements of G. These offsets in the mean suggest there is a systematic shift of around a quarter of the statistical uncertainty. The systematic uncertainty in the degree of polarisation in the target is quoted at 1.5% [113].

These systematic effects may be due to changes in the set up occurring during target polarisation changes. The target cell required complete removal from the CB and

took several hours to polarise.

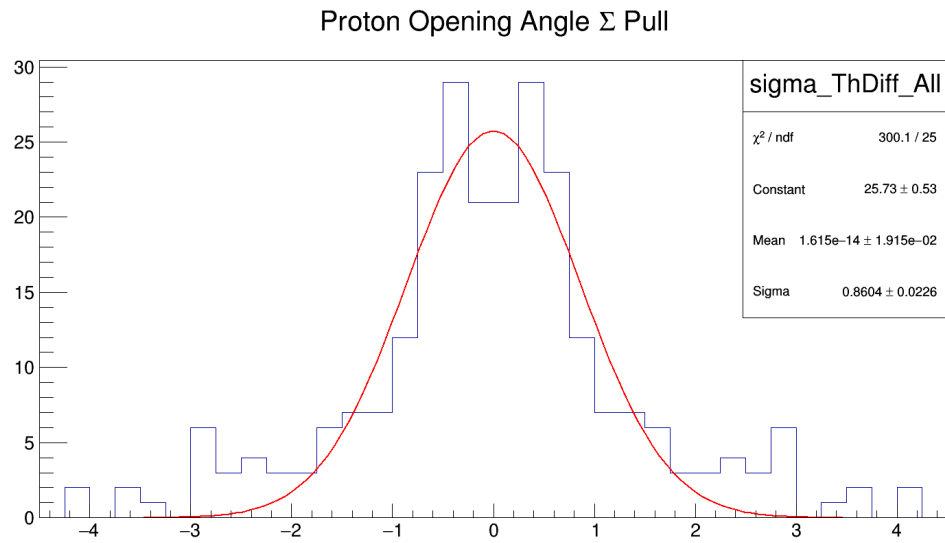


Figure 8.18: Pull distribution of results for  $\Sigma$  using the opening angle of detected and reconstructed proton as an  $s\mathcal{P}$ lot variable.

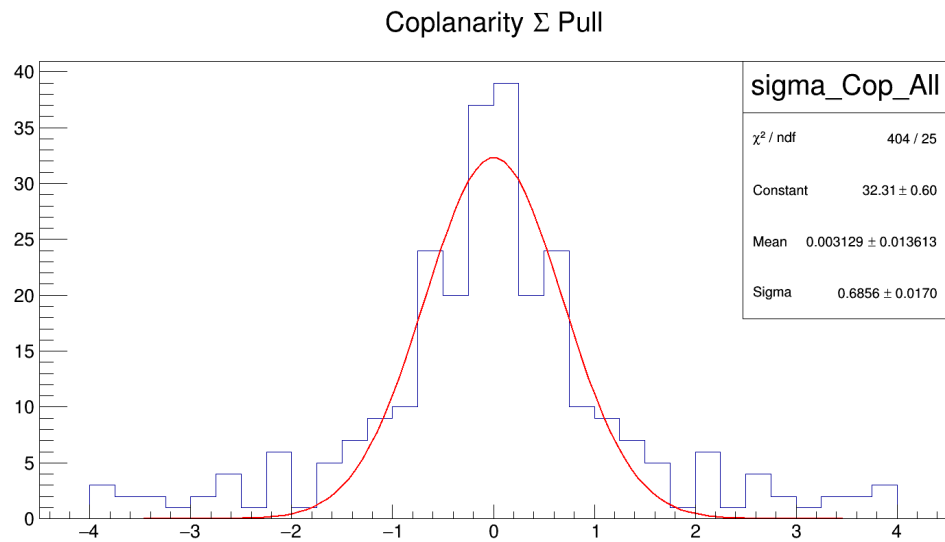


Figure 8.19: Pull distribution of results for  $\Sigma$  using the coplanarity as an  $s\mathcal{P}$ lot variable.

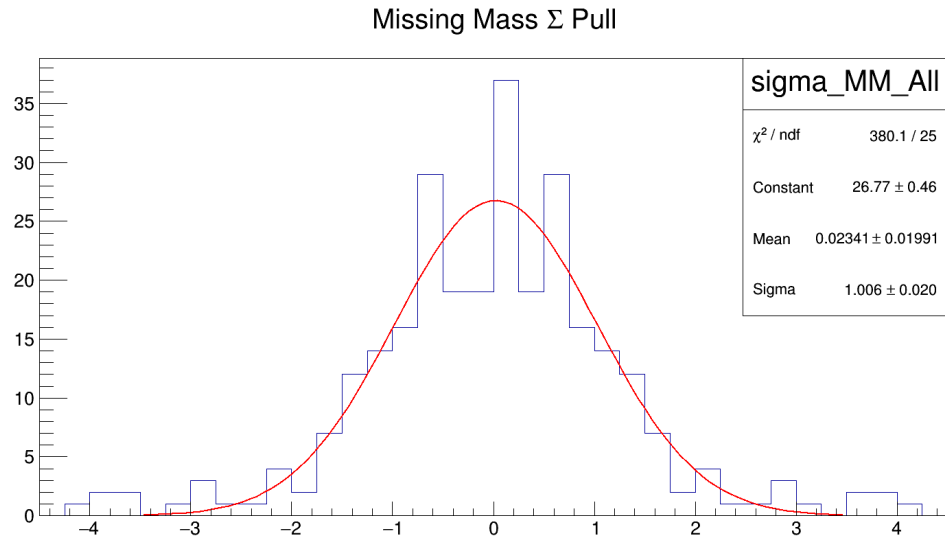


Figure 8.20: Pull distribution of results for  $\Sigma$  using the missing mass as an  $s\mathcal{P}$ lot variable.

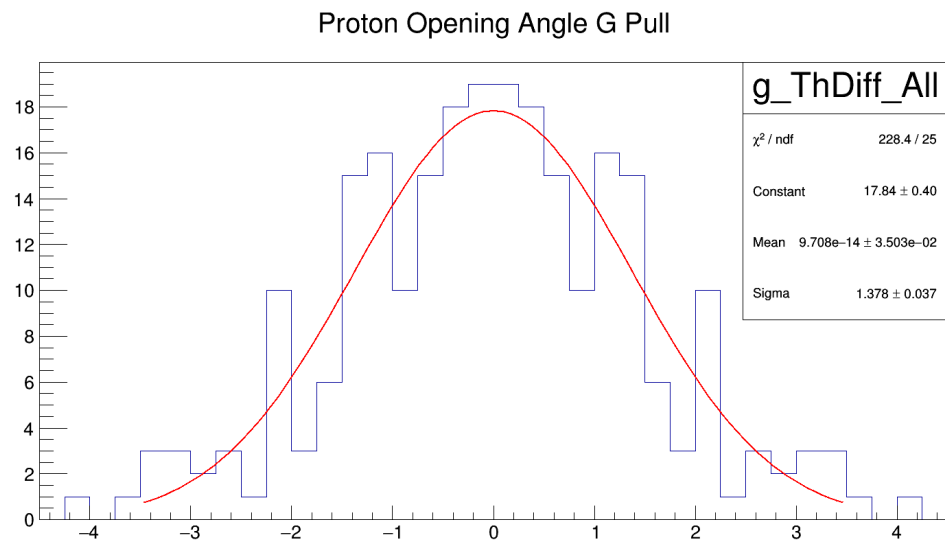
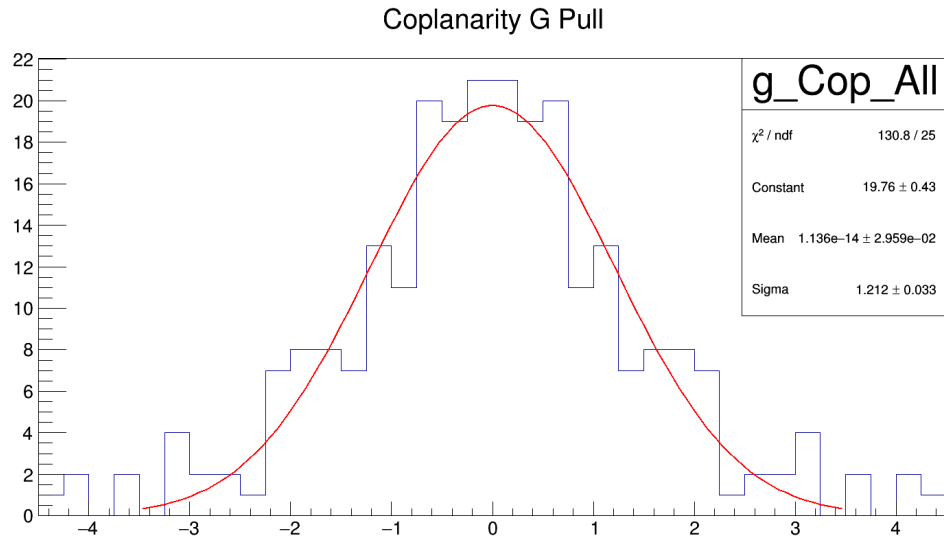
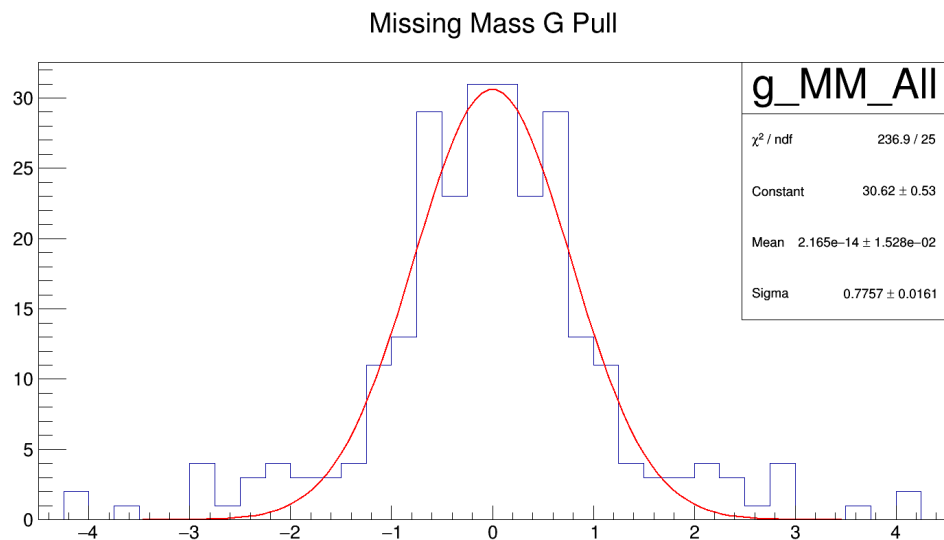


Figure 8.21: Pull distribution of results for G using the opening angle of detected and reconstructed proton as an  $s\mathcal{P}$ lot variable.

Figure 8.22: Pull distribution of results for G using the coplanarity as an  $s\mathcal{P}$ lot variable.Figure 8.23: Pull distribution of results for G using the missing mass as an  $s\mathcal{P}$ lot variable.

$s\mathcal{P}$ lot variable	Mean	Sigma
ThDiff	$0.00 \pm 0.01$	$0.86 \pm 0.02$
Coplanarity	$0.00 \pm 0.01$	$0.69 \pm 0.02$
Missing Mass	$0.02 \pm 0.02$	$1.00 \pm 0.02$

Table 8.1: Mean and sigma values of the  $s\mathcal{P}$ lot pull distributions for  $\Sigma$  measurements.

$s\mathcal{P}$ lot variable	Mean	Sigma
ThDiff	$0.00 \pm 0.04$	$1.38 \pm 0.04$
Coplanarity	$0.00 \pm 0.03$	$1.21 \pm 0.03$
Missing Mass	$0.00 \pm 0.02$	$0.78 \pm 0.02$

Table 8.2: Mean and sigma values of the  $s\mathcal{P}$ lot pull distributions for G measurements.

The mean and sigma values of the pull distributions from different subtraction methods have been tabulated in Tables 8.1 and 8.2 for  $\Sigma$  and G respectively. There are no significant systematic effects associated with the background subtraction method choice as each method's pull distribution has a mean of around zero.

The systematic effects evaluated are smaller than the statistical uncertainties observed in the data. There are no significant systematic effects from the choice of background subtraction and the uncertainty associated with target polarisation is of the order of a quarter that of the statistical uncertainty. The degree of linear polarisation presents the dominant systematic error of 8% due to a combination of the choice in normalisation baseline, measured coherent edge fluctuations and the goodness of fit to the enhancements.

The width of the G pulls suggest there is a significant uncertainty induced from the subtraction procedure. This may indicate a significant contribution from the statistical uncertainty in the yield fit which is not being propagated. There is no systematic bias though as the means are very close to zero.

## 8.6 G Results Discussion

These results present the first measurement of G in the energy range  $369 < E_\gamma < 603$  MeV in the reaction  $\gamma p \rightarrow p \pi^0$ . Previous work by Thiel et al. [75] (Section 3.1.2) is in general agreement with the work of this thesis. The PWA predictions are also in general agreement with the results presented here (Figure 8.8). At higher energies the results appear to favour the MAID and Bonn-Gatchina partial waves, with the exception of the highest energy bin measured at  $736 < E_\gamma < 769$  MeV

where the SAID solution appears to be favoured. In general the new data seem to prefer the SAID solution at backward angles ( $\cos\theta < 0$ ) while being closer to MAID and Bonn-Gatchina solutions at more forward angles.

The G observable has been measured using the *sPlot* method which, in this case, used three separate variables to provide weights to extract the signal from the data. The variables used were the missing mass, the coplanarity of  $\pi^0$  and proton, and the opening angle of reconstructed and detected proton. As can be seen the results extracted separately using the weights of the three variables are in good agreement with each other (Figures 8.5 and 8.6) with a negligible systematic effect on the choice of background subtraction. The small differences in G between different target states suggests a small systematic error relating to the degree of target polarisation (covered in Section 8.5.1).

As with the  $\Sigma$  results in Figure 8.4, the G results in Figure 8.8 are combined from positive and negative target settings using Equations 8.1 and 8.2. The coplanarity *sPlot* subtraction method has been used to calculate the final results in Figures 8.7 and 8.8. A correction factor calculated by using previous  $\Sigma$  measurements, and Bonn-Gatchina PWA curve, as a polarimeter accounts for systematic effects due to the linear polarisation seen in Figure 8.4. Section 8.4 discusses and shows the results having applied the correction factor.

Further analysis on these measurements will allow the partial wave solutions to be constrained, particularly in kinematic regions where there is large deviation in the curves. Where the partial waves start to deviate overlaps with the energy range of the Roper resonance [114]. Measurement of G in this region is of particular interest as it will allow the  $M_{1-}$  multipole to be determined (Section 2.1.5), which relates to the Roper resonance.

## 8.7 Conclusions

This work presents the results of the photon beam asymmetry  $\Sigma$  and beam-target G polarisation observables from pseudoscalar meson photoproduction off a frozen

spin Butanol target. The reaction channel  $\gamma p \rightarrow p\pi^0$  was reconstructed and used to extract the results. The measurements of the photon asymmetry  $\Sigma$  are in general agreement with previous measurements at lower energies, however show a positive systematic shift in magnitude which increases with energy. The comparison of the results with previous measurements can be used as a check of reliability as the  $\Sigma$  observable has been well measured in the energy ranges presented.

A correction factor, calculated from the comparison of the  $\Sigma$  measurements from this work to previous data by Gardner et al. [70], corrects for the systematic shift seen in Figure 8.4. The systematic shift is due to the linear polarisation and the effects of other final states in the reaction, in particular the  $\eta$  and double  $\pi$  final states. An investigation into the systematic shift is ongoing within the collaboration.

The results of the polarisation observable  $G$  show general agreement with the trends of the PWA curves, appearing to favour the MAID and Bonn-Gatchina curves. The  $G$  results are consistent through weighting from fits to different  $s\mathcal{P}$  variables and show discrepancies with PWA curves, particularly in the energy range  $E_\gamma = 603 - 769$  MeV. The results appear to favour the MAID and Bonn-Gatchina curves at higher energy bins, however the size of error bars at forward pion angles, associated with acceptance, makes it difficult to determine in these kinematic regions. Further work is necessary in order to investigate the discrepancies between the  $G$  results for different target states, including the results for the combined datasets. The correction factor from  $\Sigma$  is also applied to the  $G$  results as the systematic uncertainties are the same for both observables.

The  $s\mathcal{P}$  technique has been implemented successfully in separating background contributions from the Butanol target. This can be seen through the consistencies between the results where different distributions were used to extract the signal, in Figures 8.5 and 8.6. The systematic uncertainties associated with the choice of background subtraction method are extremely small, around zero, shown in the mean values of the pull distributions. The systematic uncertainty in the results due to the target polarisation state is around a quarter of the statistical uncertainty (Figures 8.17 and 8.16). The linear polarisation is the dominant systematic with a

systematic uncertainty of 8%.

Inclusion of systematic effects and further analysis will allow accurate determination and constraint of the  $M_{1-}$  partial wave, which has a particular sensitivity to the  $P_{11}(1440)$  Roper-resonance. The Roper resonance is the first radial excitation of the nucleon and is an  $N^*(J^P = \frac{1}{2}^+)$  state. Quark models based on  $SU(6)$  symmetry expect the first excitation of the nucleon to be an  $N^*(J^P = \frac{1}{2}^-)$  state and for the  $\frac{1}{2}^+$  state to be the second. Measurement of the Roper resonance's properties, which are still poorly understood [16, 115, 116], may shed light on the reason why the Roper resonance is the first  $N^*$  state observed. To this end, an accurate measurement of the  $G$  observable will allow the  $M_{1-}$  partial wave to be determined, and in turn allow the properties of the Roper resonance to be better understood and constrained.

Continued analysis of the systematics of the  $s\mathcal{P}$ lot method and dominant systematic uncertainty from the linear polarisation will improve the reliability and consistency of the  $G$  measurements, with a view towards publishing results to be included in the world dataset.

# Appendix A

## Tabulated Results

### A.1 $\Sigma$ Results

$\cos(\theta)$	Energy (MeV)	$\Sigma$	$\sigma$
-1.0 - -0.8	386.67	0.45	0.03
-0.8 - -0.6	386.67	0.65	0.03
-0.6 - -0.4	386.67	0.66	0.01
-0.4 - -0.2	386.67	0.69	0.01
-0.2 - 0.0	386.67	0.63	0.01
0.0 - 0.2	386.67	0.70	0.03
0.2 - 0.4	386.67	0.55	0.23
0.4 - 0.6	386.67	0.29	0.19
0.6 - 0.8	386.67	0.40	0.18
0.8 - 1.0	386.67	0.16	0.11
-1.0 - -0.8	420.00	0.54	0.03
-0.8 - -0.6	420.00	0.72	0.02
-0.6 - -0.4	420.00	0.71	0.01
-0.4 - -0.2	420.00	0.68	0.01
-0.2 - 0.0	420.00	0.64	0.01

0.0 - 0.2	420.00	0.61	0.01
0.2 - 0.4	420.00	0.61	0.09
0.4 - 0.6	420.00	0.40	0.18
0.6 - 0.8	420.00	0.25	0.16
0.8 - 1.0	420.00	-0.02	0.09
-1.0 - -0.8	453.33	0.68	0.04
-0.8 - -0.6	453.33	0.75	0.03
-0.6 - -0.4	453.33	0.72	0.02
-0.4 - -0.2	453.33	0.68	0.02
-0.2 - 0.0	453.33	0.68	0.02
0.0 - 0.2	453.33	0.59	0.02
0.2 - 0.4	453.33	0.51	0.04
0.4 - 0.6	453.33	0.63	0.25
0.6 - 0.8	453.33	0.16	0.18
0.8 - 1.0	453.33	0.07	0.15
-1.0 - -0.8	486.67	0.75	0.07
-0.8 - -0.6	486.67	0.67	0.07
-0.6 - -0.4	486.67	0.75	0.04
-0.4 - -0.2	486.67	0.73	0.03
-0.2 - 0.0	486.67	0.69	0.03
0.0 - 0.2	486.67	0.59	0.04
0.2 - 0.4	486.67	0.47	0.04
0.4 - 0.6	486.67		
0.6 - 0.8	486.67		
0.8 - 1.0	486.67	0.13	0.21
-1.0 - -0.8	520.00	0.82	0.09
-0.8 - -0.6	520.00	0.89	0.07
-0.6 - -0.4	520.00	0.78	0.04

-0.4 - -0.2	520.00	0.71	0.04
-0.2 - 0.0	520.00	0.65	0.04
0.0 - 0.2	520.00	0.57	0.04
0.2 - 0.4	520.00	0.51	0.05
0.4 - 0.6	520.00	0.25	0.13
0.6 - 0.8	520.00	0.00	0.35
0.8 - 1.0	520.00		
-1.0 - -0.8	553.33	0.71	0.14
-0.8 - -0.6	553.33	0.87	0.12
-0.6 - -0.4	553.33	0.74	0.07
-0.4 - -0.2	553.33	0.71	0.06
-0.2 - 0.0	553.33	0.61	0.06
0.0 - 0.2	553.33	0.66	0.11
0.2 - 0.4	553.33	0.61	0.08
0.4 - 0.6	553.33	0.33	0.19
0.6 - 0.8	553.33		
0.8 - 1.0	553.33		
-1.0 - -0.8	586.67	0.61	0.09
-0.8 - -0.6	586.67	0.79	0.07
-0.6 - -0.4	586.67	0.77	0.05
-0.4 - -0.2	586.67	0.72	0.04
-0.2 - 0.0	586.67	0.75	0.04
0.0 - 0.2	586.67	0.60	0.04
0.2 - 0.4	586.67	0.42	0.05
0.4 - 0.6	586.67	0.45	0.07
0.6 - 0.8	586.67	-0.12	0.29
0.8 - 1.0	586.67	-0.34	0.24
-1.0 - -0.8	620.00	0.49	0.08

-0.8 - -0.6	620.00	0.82	0.06
-0.6 - -0.4	620.00	0.81	0.04
-0.4 - -0.2	620.00	0.77	0.04
-0.2 - 0.0	620.00	0.73	0.04
0.0 - 0.2	620.00	0.63	0.04
0.2 - 0.4	620.00	0.52	0.05
0.4 - 0.6	620.00	0.36	0.06
0.6 - 0.8	620.00	-0.28	0.31
0.8 - 1.0	620.00	-0.19	0.17
-1.0 - -0.8	653.33	0.37	0.08
-0.8 - -0.6	653.33	0.87	0.08
-0.6 - -0.4	653.33	0.92	0.05
-0.4 - -0.2	653.33	0.87	0.04
-0.2 - 0.0	653.33	0.80	0.05
0.0 - 0.2	653.33	0.75	0.05
0.2 - 0.4	653.33	0.68	0.06
0.4 - 0.6	653.33	0.48	0.07
0.6 - 0.8	653.33	0.73	0.46
0.8 - 1.0	653.33	-0.05	0.23
-1.0 - -0.8	686.67	0.38	0.12
-0.8 - -0.6	686.67	0.60	0.10
-0.6 - -0.4	686.67	0.87	0.06
-0.4 - -0.2	686.67	0.90	0.06
-0.2 - 0.0	686.67	0.87	0.05
0.0 - 0.2	686.67	0.81	0.06
0.2 - 0.4	686.67	0.71	0.06
0.4 - 0.6	686.67	0.67	0.08
0.6 - 0.8	686.67	-0.50	0.36

---

0.8 - 1.0	686.67	-0.29	0.32
-1.0 - -0.8	720.00	0.29	0.09
-0.8 - -0.6	720.00	0.68	0.08
-0.6 - -0.4	720.00	0.76	0.05
-0.4 - -0.2	720.00	0.80	0.05
-0.2 - 0.0	720.00	0.76	0.06
0.0 - 0.2	720.00	0.88	0.07
0.2 - 0.4	720.00	0.85	0.06
0.4 - 0.6	720.00	0.78	0.05
0.6 - 0.8	720.00	0.64	0.12
0.8 - 1.0	720.00	0.15	0.30
-1.0 - -0.8	753.33	0.30	0.09
-0.8 - -0.6	753.33	0.46	0.09
-0.6 - -0.4	753.33	0.71	0.06
-0.4 - -0.2	753.33	0.74	0.05
-0.2 - 0.0	753.33	0.82	0.05
0.0 - 0.2	753.33	0.81	0.05
0.2 - 0.4	753.33	0.75	0.07
0.4 - 0.6	753.33	0.71	0.07
0.6 - 0.8	753.33	0.66	0.19
0.8 - 1.0	753.33	-0.13	0.40

## A.2 Tabulated G Results

$\cos(\theta)$	Energy (MeV)	G	$\sigma$
-1.0 - -0.8	386.67	0.06	0.03
-0.8 - -0.6	386.67	0.05	0.04
-0.6 - -0.4	386.67	-0.00	0.02
-0.4 - -0.2	386.67	-0.04	0.02
-0.2 - 0.0	386.67	-0.10	0.02
0.0 - 0.2	386.67	-0.09	0.04
0.2 - 0.4	386.67	-0.13	0.24
0.4 - 0.6	386.67	-0.31	0.24
0.6 - 0.8	386.67	0.15	0.24
0.8 - 1.0	386.67	-0.06	0.13
-1.0 - -0.8	420.00	0.06	0.04
-0.8 - -0.6	420.00	-0.00	0.03
-0.6 - -0.4	420.00	-0.02	0.02
-0.4 - -0.2	420.00	-0.10	0.01
-0.2 - 0.0	420.00	-0.10	0.01
0.0 - 0.2	420.00	-0.18	0.02
0.2 - 0.4	420.00	0.05	0.09
0.4 - 0.6	420.00	0.42	0.28
0.6 - 0.8	420.00	-0.01	0.15
0.8 - 1.0	420.00	0.07	0.11
-1.0 - -0.8	453.33	0.05	0.05
-0.8 - -0.6	453.33	0.03	0.05
-0.6 - -0.4	453.33	0.02	0.03
-0.4 - -0.2	453.33	-0.13	0.02
-0.2 - 0.0	453.33	-0.15	0.02

0.0 - 0.2	453.33	-0.16	0.02
0.2 - 0.4	453.33	-0.16	0.05
0.4 - 0.6	453.33	0.09	0.28
0.6 - 0.8	453.33	-0.09	0.22
0.8 - 1.0	453.33	-0.04	0.15
-1.0 - -0.8	486.67	0.06	0.10
-0.8 - -0.6	486.67	-0.10	0.11
-0.6 - -0.4	486.67	-0.10	0.06
-0.4 - -0.2	486.67	-0.33	0.05
-0.2 - 0.0	486.67	-0.26	0.04
0.0 - 0.2	486.67	-0.27	0.05
0.2 - 0.4	486.67	-0.31	0.06
0.4 - 0.6	486.67	-0.37	0.20
0.6 - 0.8	486.67		
0.8 - 1.0	486.67		
-1.0 - -0.8	520.00	0.03	0.13
-0.8 - -0.6	520.00	-0.02	0.12
-0.6 - -0.4	520.00	-0.10	0.07
-0.4 - -0.2	520.00	-0.25	0.06
-0.2 - 0.0	520.00	-0.29	0.05
0.0 - 0.2	520.00	-0.33	0.06
0.2 - 0.4	520.00	-0.30	0.06
0.4 - 0.6	520.00	-0.19	0.18
0.6 - 0.8	520.00	0.00	0.58
0.8 - 1.0	520.00		
-1.0 - -0.8	553.33	0.02	0.20
-0.8 - -0.6	553.33	-0.23	0.18
-0.6 - -0.4	553.33	-0.27	0.11

-0.4 - -0.2	553.33	-0.28	0.09
-0.2 - 0.0	553.33	-0.26	0.09
0.0 - 0.2	553.33	-0.14	0.30
0.2 - 0.4	553.33	-0.32	0.11
0.4 - 0.6	553.33	-0.24	0.20
0.6 - 0.8	553.33		
0.8 - 1.0	553.33		
-1.0 - -0.8	586.67	-0.26	0.12
-0.8 - -0.6	586.67	-0.29	0.10
-0.6 - -0.4	586.67	-0.31	0.07
-0.4 - -0.2	586.67	-0.30	0.05
-0.2 - 0.0	586.67	-0.29	0.06
0.0 - 0.2	586.67	-0.23	0.05
0.2 - 0.4	586.67	-0.34	0.06
0.4 - 0.6	586.67	-0.21	0.08
0.6 - 0.8	586.67	0.19	0.34
0.8 - 1.0	586.67	-0.08	0.26
-1.0 - -0.8	620.00	0.10	0.11
-0.8 - -0.6	620.00	-0.27	0.09
-0.6 - -0.4	620.00	-0.21	0.06
-0.4 - -0.2	620.00	-0.28	0.05
-0.2 - 0.0	620.00	-0.28	0.05
0.0 - 0.2	620.00	-0.27	0.05
0.2 - 0.4	620.00	-0.26	0.06
0.4 - 0.6	620.00	-0.06	0.08
0.6 - 0.8	620.00	0.27	0.43
0.8 - 1.0	620.00	-0.08	0.19
-1.0 - -0.8	653.33	-0.09	0.10

-0.8 - -0.6	653.33	-0.27	0.10
-0.6 - -0.4	653.33	-0.24	0.07
-0.4 - -0.2	653.33	-0.25	0.06
-0.2 - 0.0	653.33	-0.27	0.06
0.0 - 0.2	653.33	-0.36	0.07
0.2 - 0.4	653.33	-0.16	0.08
0.4 - 0.6	653.33	-0.14	0.08
0.6 - 0.8	653.33	-0.10	0.46
0.8 - 1.0	653.33	0.23	0.27
-1.0 - -0.8	686.67	-0.21	0.15
-0.8 - -0.6	686.67	-0.39	0.16
-0.6 - -0.4	686.67	-0.36	0.09
-0.4 - -0.2	686.67	-0.31	0.08
-0.2 - 0.0	686.67	-0.34	0.07
0.0 - 0.2	686.67	-0.30	0.08
0.2 - 0.4	686.67	-0.30	0.08
0.4 - 0.6	686.67	-0.04	0.10
0.6 - 0.8	686.67	0.11	0.46
0.8 - 1.0	686.67	-0.08	0.39
-1.0 - -0.8	720.00	-0.23	0.11
-0.8 - -0.6	720.00	-0.34	0.11
-0.6 - -0.4	720.00	-0.30	0.08
-0.4 - -0.2	720.00	-0.38	0.07
-0.2 - 0.0	720.00	-0.43	0.07
0.0 - 0.2	720.00	-0.32	0.08
0.2 - 0.4	720.00	-0.12	0.08
0.4 - 0.6	720.00	-0.02	0.08
0.6 - 0.8	720.00	0.08	0.16

---

0.8 - 1.0	720.00	0.63	0.37
-1.0 - -0.8	753.33	-0.31	0.12
-0.8 - -0.6	753.33	-0.34	0.14
-0.6 - -0.4	753.33	-0.39	0.08
-0.4 - -0.2	753.33	-0.33	0.07
-0.2 - 0.0	753.33	-0.35	0.06
0.0 - 0.2	753.33	-0.27	0.07
0.2 - 0.4	753.33	-0.17	0.08
0.4 - 0.6	753.33	-0.19	0.10
0.6 - 0.8	753.33	-0.09	0.29
0.8 - 1.0	753.33	-0.43	0.50

# Bibliography

- [1] E. Rutherford. “Collision of  $\alpha$  particles with light atoms. IV. An anomalous effect in nitrogen”. In: *Philosophical Magazine* 90.sup1 (2010), pp. 31–37. arXiv: arXiv:1011.1669v3. DOI: 10.1080/14786431003659230.
- [2] J. Chadwick. “Possible Existence of a Neutron”. In: *Nature* 129 (1932), p. 312. DOI: 10.1038/129312a0.
- [3] Henley E. A. and Garcia. *Subatomic Physics*. Vol. 53. 9. World Scientific Publishing Co. Pte. Ltd., 2013, pp. 1689–1699. arXiv: arXiv:1011.1669v3. DOI: 10.1017/CB09781107415324.004.
- [4] Nakano T. and Nishijima K. “Charge Independence for V-particles”. In: *Progress of Theoretical Physics* 10.5 (1953), pp. 581–582. eprint: /oup/backfile/content\_public/journal/ptp/10/5/10.1143/ptp.10.581/2/10-5-581.pdf. DOI: 10.1143/PTP.10.581.
- [5] M. Gell-Mann. “Isotopic spin and new unstable particles”. In: *Physical Review* 92.3 (1953), pp. 833–834. DOI: 10.1103/PhysRev.92.833.
- [6] M. Gell-Mann. “A schematic model of baryons and mesons”. In: *Physics Letters* 8.3 (1964). URL: [http://tuvalu.santafe.edu/~7B~%7Dmgm/Site/Publications%7B%5C\\_%7Dfiles/MGM%2047.pdf](http://tuvalu.santafe.edu/~7B~%7Dmgm/Site/Publications%7B%5C_%7Dfiles/MGM%2047.pdf).
- [7] M. Gell-Mann Y. and Ne’eman. “The eightfold way”. In: *Nuclear Physics* 79.2 (1966), pp. 477–478. DOI: 10.1016/0029-5582(66)90165-9.
- [8] Gell-Mann M. and Zachariasen F. “Form Factors and Vector Mesons”. In: *Phys. Rev.* 124 (1961), pp. 953–964. DOI: 10.1103/PhysRev.124.953.

- [9] G. Zweig. “An SU(3) model for strong interaction symmetry and its breaking. Version 2”. In: (Feb. 1964), pp. 22–101.
- [10] O. W. Greenberg. “Spin and unitary-spin independence in a paraquark model of baryons and mesons”. In: *Physical Review Letters* 13.20 (1964), pp. 598–602. DOI: 10.1103/PhysRevLett.13.598.
- [11] O. W. Greenberg and M. Resnikoff. “Symmetric quark model of baryon resonances”. In: *Physical Review* 163.5 (1967), pp. 1844–1851. DOI: 10.1103/PhysRev.163.1844.
- [12] David Faiman and Archibald W. Hendry. “Harmonic-oscillator model for baryons”. In: *Physical Review* 180.5 (1969), pp. 1609–1610. DOI: 10.1103/PhysRev.180.1609.
- [13] DB Lichtenberg. “Baryon Supermultiplets of SU(6) x O(3) in a Quark-Diquark Model”. In: *Physical Review* 178 (1969), p. 2197. URL: <http://journals.aps.org/pr/abstract/10.1103/PhysRev.178.2197>.
- [14] J. Carroll, D. Lichtenberg, and J Franklin. “Electromagnetic Properties of Baryons in a Quark-Diquark Model with Broken SU(6)”. In: *Physical Review* 174.5 (1968), pp. 1681–1688. URL: <https://journals.aps.org/pr/pdf/10.1103/PhysRev.174.1681>.
- [15] E. Santopinto. “Interacting quark-diquark model of baryons”. In: *Physical Review C - Nuclear Physics* 72.2 (2005), pp. 1–5. arXiv: 0412319 [hep-ph]. DOI: 10.1103/PhysRevC.72.022201.
- [16] S. Capstick and W. Roberts. “Quark Models of Baryon Masses and Decays”. In: *Progress in Particle and Nuclear Physics* 45.00 (2000), S241–S331. arXiv: 0011082 [nucl-th]. DOI: 10.1016/S0146-6410(00)00109-5.
- [17] C. Patrignani et al. “Review of Particle Physics”. In: *Chinese Physics C* 40 (2016), p. 100001. arXiv: 0601168 [astro-ph]. DOI: 10.1103/PhysRevD.86.010001.

- [18] C. Amsler et al. “Review of Particle Physics”. In: *Physics Letters B: Nuclear, Elementary Particle and High-Energy Physics*, 667.1-5 (2014), pp. 1–6. arXiv: 0104147. DOI: 10.1016/j.physletb.2008.07.018.
- [19] Bricman C. Barxyre P. and G. Villkt. “Phase-Shift Analysis of Pion-Nucleon Elastic Scattering below 1.6 Gev”. In: *Physical Review* 165.5 (1968). URL: <https://journals.aps.org/pr/abstract/10.1103/PhysRev.165.1730>.
- [20] Donnachie A. Auvil P. Lovelace C. and LEA A. T. “Pion-Nucleon phase shifts and resonances”. In: *Physics Letters* 12.I (1964), pp. 5–9. URL: <http://www.sciencedirect.com/science/article/pii/0031916364911849>.
- [21] B. H. Bransden P. J. O’Donnell and R. G. Moorehouse. “Pion-Nucleon Scattering Amplitudes in the Range 300-200 Mev”. In: *Physical Review* 1.6 (1965). URL: <https://journals.aps.org/pr/abstract/10.1103/PhysRev.139.B1566>.
- [22] P. J. Brandsen B. H. O’Donnell and R. G. Moorhouse. “Pion-Nucleon scattering and resonant states near 900 MeV”. In: *Physics Letters* 19.5 (1965). URL: <http://www.sciencedirect.com/science/article/pii/003191636590925X>.
- [23] Kenneth M. Watson. “Some general relations between the photoproduction and scattering of  $\pi$  mesons”. In: *Physical Review* 95.1 (1954), pp. 228–236. DOI: 10.1103/PhysRev.95.228.
- [24] S. D. Drell, H. M. Friedman, and F. Zachariasen. “Theory of S-Wave Pion Scattering and Photoproduction at Low Energies”. In: *Physical Review* 104.1 (1956). URL: <https://journals.aps.org/pr/abstract/10.1103/PhysRev.104.236>.
- [25] M Maccormick et al. “Total photoabsorption cross sections for 1H, 2H, and 3He from 200 to 800 MeV”. In: *Physical Review C* 53.1 (1996), pp. 41–49.
- [26] Lewis G. M. Armstrong T. A. Hogg W. R. and Robertson A. W. “The total photon-proton cross section for hadron production”. In: *Physics Letters* 34.6 (1971), pp. 535–538.

- [27] N. Bianchi et al. “Absolute total photoabsorption cross sections on nuclei in the nucleon resonance region”. In: *Physics Letters B* 325.3-4 (1994), pp. 333–336. DOI: 10.1016/0370-2693(94)90021-3.
- [28] D Dreschsel and L Tiator. *Threshold pion photoproduction on nucleons*. 1992. DOI: 10.1088/0954-3899/18/3/004.
- [29] V. Crede et al. “Photoproduction of  $\eta$  mesons off protons for  $0.75 \text{ GeV} < E_\gamma < 3 \text{ GeV}$ ”. In: *Physical Review Letters* 94.1 (2005), pp. 1–5. arXiv: 0311045 [arXiv:hep-ex]. DOI: 10.1103/PhysRevLett.94.012004.
- [30] T. Mart et al. “Kaon photoproduction on the nucleon: overview of some applications”. In: *Nuclear Physics A* (2001), pp. 502–504.
- [31] B. Dey et al. “Differential cross sections and recoil polarizations for the reaction  $\gamma p \rightarrow K + \Sigma^0$ ”. In: (2010), pp. 1–23. arXiv: 1006.0374. DOI: 10.1103/PhysRevC.82.025202.
- [32] Skoupil D. and Bydžovský P. “Photoproduction of  $K\Lambda$  on the proton”. In: *Physical Review C - Nuclear Physics* 93.2 (2016), pp. 1–20. arXiv: arXiv: 1601.03840v1. DOI: 10.1103/PhysRevC.93.025204.
- [33] E. Gutz et al. “High statistics study of the reaction  $\gamma p \rightarrow p\pi^0\eta$ ”. In: *The European Physical Journal A* 50.4 (Apr. 2014), p. 74. DOI: 10.1140/epja/i2014-14074-1.
- [34] Y Assafiri et al. “Double  $\pi^0$  Photoproduction on the Proton at GRAAL”. In: *Phys Rev Lett* 90.22 (2003), p. 222001. DOI: 10.1103/PhysRevLett.90.222001.
- [35] J. Ajaka et al. “Simultaneous photoproduction of  $\eta$  and  $\pi^0$  mesons on the proton”. In: *Physical Review Letters* 100.5 (2008), pp. 1–5. DOI: 10.1103/PhysRevLett.100.052003.
- [36] I. Horn and for the CB-ELSA Collaboration. “Study of the reaction  $\gamma p \rightarrow p\pi^0$ ”. In: 186 (2008), pp. 173–186. arXiv: 0806.4251. DOI: 10.1140/epja/i2008-10657-7.

- [37] E. Oset et al. “Two pion photoproduction on nucleons and nuclei in the rho and sigma regions”. In: (2001), pp. 1–20. URL: <http://arxiv.org/abs/nucl-th/0112033>. arXiv: 0112033 [nucl-th].
- [38] Hiromi Kaneko et al. “Photoproduction of the rho meson and its magnetic moments”. In: *American Institute of Physics* 254 (2011), pp. 254–256. DOI: 10.1063/1.3647384.
- [39] A. Wilson et al. “Photoproduction of  $\omega$  mesons off the proton”. In: *Physics Letters, Section B: Nuclear, Elementary Particle and High-Energy Physics* 749 (2015), pp. 407–413. arXiv: arXiv:0909.1248v2. DOI: 10.1016/j.physletb.2015.08.011.
- [40] Alvin Kiswandhi, Shin Nan Yang, and Yu Bing Dong. “Near-threshold incoherent  $\phi$  photoproduction on the deuteron: Searching for traces of a resonance”. In: *Physical Review C* 015202.94 (2016), pp. 1–18. arXiv: 1604.01555. DOI: 10.1103/PhysRevC.94.015202.
- [41] Mark Sikora. “Recoil Polarimetry in Meson Photoproduction Reactions”. PhD thesis. 2011.
- [42] Ron Workman. “Update on Partial-Wave Analysis”. In: (2001), pp. 1–6. URL: <http://arxiv.org/abs/nucl-th/0104028>. arXiv: 0104028 [nucl-th].
- [43] F. Berends, A. Donnachie, and D. Weaver. “Photoproduction and Electroproduction of Pions (I) Dispersion Relation Theory”. In: *Nuclear Physics B* 4 (1967), pp. 1–53. URL: <http://www.sciencedirect.com/science/article/pii/0550321367901964?via%7B%7D3Dihub>.
- [44] Tanabe H. and Ohta K. “Dynamical model for pion photoproduction in the Delta region”. In: *Physical Review C* 31.5 (1985). URL: <https://journals.aps.org/prc/pdf/10.1103/PhysRevC.31.1876>.
- [45] G. F. Chew et al. “Relativistic dispersion relation approach to photomeson production”. In: *Physical Review* 106.6 (1957), pp. 1345–1355. DOI: 10.1103/PhysRev.106.1345.

- [46] Donnachie A. Barker I. S. and Storrow J. K. “Analysis of  $\pi^0$  Photoproduction at Intermediate and High Energies”. In: *Nuclear Physics B* 79 (Feb. 1974), pp. 431–460. DOI: 10.1088/0957-0233/3/2/018.
- [47] I. S. Barker, A. Donnachie, and J. K. Storrow. “Complete experiments in pseudoscalar photoproduction”. In: *Nuclear Physics, Section B* 95.2 (1975), pp. 347–356. DOI: 10.1016/0550-3213(75)90049-8.
- [48] B. Adelseck, A. R. and Saghai. “Kaon photoproduction: Data consistency, coupling constants, and polarization observables”. In: *Physical Review C* 42.1 (1990), pp. 108–127. URL: <https://journals.aps.org/prc/abstract/10.1103/PhysRevC.42.108>.
- [49] A. M. Sandorfi et al. “The determination of pseudoscalar meson photoproduction amplitudes from complete experiments”. In: *AIP Conference Proceedings* 1388 (2011), pp. 99–105. arXiv: 1010.4555. DOI: 10.1063/1.3647357.
- [50] Wen-Tai Chiang and Frank Tabakin. “Completeness rules for spin observables in pseudoscalar meson photoproduction”. In: *Physical Review C* 55.4 (Apr. 1997), pp. 2054–2066. arXiv: 9611053 [nucl-th]. DOI: 10.1103/PhysRevC.55.2054.
- [51] Greg Keaton and Ron Workman. “Amplitude ambiguities in pseudoscalar meson photoproduction”. In: *Physical Review C - Nuclear Physics* 53.3 (1996), pp. 1434–1435. DOI: 10.1103/PhysRevC.53.1434.
- [52] Tom Vranex et al. “The incompleteness of complete pseudoscalar-meson photoproduction”. In: *Phys. Rev. C* 87 (2013). arXiv: 1303.2936. DOI: 10.1103/PhysRevC.87.055205.
- [53] Simon Gardner. “Polarisation Observables in Neutral Pion Photoproduction with MAMI”. PhD thesis. Sept. 2016.
- [54] W Panovsky, J. Steinberger, and J Steller. “Further Results on the Production of Neutral Mesons by Photons”. In: *Physical Review* 86.2 (1952). URL: <https://journals.aps.org/pr/abstract/10.1103/PhysRev.86.180>.

- [55] Drickey F. and Mozley J. “Neutral Meson Production with Polarized X Rays”. In: 136.2 (1964), pp. 1–803.
- [56] Bussey J., Rutherglen P. “Measurements of the double polarisation parameters G and H in neutral pion photoproduction”. In: *Nuclear Physics B* 159.3 (1979), pp. 383–396. DOI: [https://doi.org/10.1016/0550-3213\(79\)90341-9](https://doi.org/10.1016/0550-3213(79)90341-9).
- [57] G Blanpied et al. “N  $\rightarrow$   $\Delta$  Transition from Simultaneous Measurements of  $p(\bar{\gamma},\pi)$  and  $p(\bar{\gamma},\gamma)$ ”. In: *Physical Review Letters* 79 (1997), pp. 4337–4340. DOI: <https://doi.org/10.1103/PhysRevLett.79.4337>.
- [58] G Blanpied et al. “Polarized Compton Scattering from the Proton”. In: *Physical Review Letters* 76 (1996), pp. 1023–1026.
- [59] F. V. Adamian et al. “Measurement of the cross section asymmetry of the reaction  $\gamma p \rightarrow \pi^0 p$  in the resonance energy region  $E_\gamma = 0.5 - 1.1$  GeV”. In: *Physical Review C* 63.5 (2001), p. 054606. DOI: [10.1103/PhysRevC.63.054606](https://doi.org/10.1103/PhysRevC.63.054606).
- [60] O. Bartalini et al. “Measurement of  $\pi^0$  photoproduction on the proton from 550 to 1500 MeV at GRAAL”. In: *European Physical Journal A* 26.3 (2005), pp. 399–419. DOI: [10.1140/epja/i2005-10191-2](https://doi.org/10.1140/epja/i2005-10191-2).
- [61] D. Elsner et al. “Linearly polarised photon beams at ELSA and measurement of the beam asymmetry in  $\pi^0$  photoproduction off the proton”. In: *European Physical Journal A* 39.3 (2009), pp. 373–381. DOI: [10.1140/epja/i2008-10708-1](https://doi.org/10.1140/epja/i2008-10708-1).
- [62] N. Sparks et al. “Measurement of the Beam Asymmetry  $\Sigma$  in the Forward Direction for  $\pi^0$  Photoproduction”. In: *Physical Review C - Nuclear Physics* 81.6 (Mar. 2010), pp. 1–10. arXiv: 1003.1346. DOI: [10.1103/PhysRevC.81.065210](https://doi.org/10.1103/PhysRevC.81.065210).
- [63] R Beck et al. “Measurement of the E2/M1 Ratio in the N $\rightarrow$ D Transition using the reaction  $p(\bar{\gamma},p)\pi^0$ ”. In: *Physical Review Letters* 78 (1997), p. 606.

- [64] G. Audit et al. “DAPHNE: a large-acceptance tracking detector for the study of photoreactions at intermediate energies”. In: *Nuclear Inst. and Methods in Physics Research, A* 301.3 (1991), pp. 473–481. DOI: 10.1016/0168-9002(91)90013-G.
- [65] R Crawford et al. “Two-body photodisintegration of the deuteron from 100 to 800 MeV”. In: *Nuclear Physics A* 603.96 (1996), pp. 303–325.
- [66] Roman Leukel. “Photoproduktion neutraler Pionen am Proton mit linear polarisierten Photonen im Bereich der (1232) Resonanz”. PhD thesis. 2001.
- [67] R. Beck. “Experiments with polarized  $^3\text{He}$  at MAMI”. In: *European Physical Journal A* 28.SUPPL. 1 (2006), pp. 29–38. DOI: 10.1140/epja/i2006-09-004-7.
- [68] D. Drechsel et al. “A unitary isobar model for pion photo- and electroproduction on the proton up to 1 GeV”. In: *Nuclear Physics A* 645.1 (1999), pp. 145–174. arXiv: 9807001v2 [arXiv:nucl-th]. DOI: 10.1016/S0375-9474(98)00572-7.
- [69] D. Hornidge et al. “Accurate test of chiral dynamics in the  $\bar{\gamma}p \rightarrow \pi^0p$  reaction”. In: *Physical Review Letters* 111.6 (2013), pp. 1–5. arXiv: arXiv:1211.5495v2. DOI: 10.1103/PhysRevLett.111.062004.
- [70] S. Gardner et al. “Photon asymmetry measurements of  $\bar{\gamma}p \rightarrow \pi^0p$  for  $E_\gamma = 320$ –650 MeV”. In: 1520 (2016), pp. 1–11. arXiv: 1606.07930. DOI: 10.1140/epja/i2016-16333-5.
- [71] S. S. Kamalov et al. “Recent results from the MAID and Dubna-Mainz-Taipei PWA analysis”. In: *NSTAR 2007: Proceedings of The 11th Workshop on The Physics of Excited Nucleons, 5–8 September 2007, Bonn, Germany*. Ed. by Hans-Werner Hammer et al. Berlin, Heidelberg: Springer Berlin Heidelberg, 2008, pp. 115–120. DOI: 10.1007/978-3-540-85144-8\_21.
- [72] R.A. Arndt, I.I. Strakovsky, and R.L. Workman. “The Said PWA Program”. In: *International Journal of Modern Physics A* 18.3 (2003), pp. 449–456.

- [73] A. V. Anisovich et al. “Photoproduction of pions and properties of baryon resonances from a Bonn-Gatchina partial-wave analysis”. In: *European Physical Journal A* 44.2 (2010), pp. 203–220. arXiv: 0911.5277. DOI: 10.1140/epja/i2010-10950-x.
- [74] J. Ahrens et al. “Measurement of the G asymmetry for the  $\gamma p \rightarrow N\pi$  channels in the  $\Delta(1232)$  resonance region”. In: *European Physical Journal A* 26.1 (2005), pp. 135–140. DOI: 10.1140/epja/i2005-10158-3.
- [75] A. Thiel et al. “Double-polarization observable G in neutral-pion photoproduction off the proton”. In: *The European Physical Journal A* 53.1 (2017), p. 8. DOI: 10.1140/epja/i2017-12194-8.
- [76] D. Drechsel, S.S. Kamalov, and L. Tiator. “Unitary Isobar Model - MAID2007”. In: *Eur.Phys.J.* A34 (2007), pp. 69–97. arXiv: 0710.0306 [nucl-th]. DOI: 10.1140/epja/i2007-10490-6.
- [77] D. Drechsel et al. “A unitary isobar model for pion photo- and electroproduction on the proton up to 1 GeV”. In: *Nuclear Physics A* 645.1 (1999), pp. 145–174. arXiv: 9807001v2 [arXiv:nucl-th]. DOI: 10.1016/S0375-9474(98)00572-7.
- [78] Ron L. Workman et al. “Unified Chew-Mandelstam SAID analysis of pion photoproduction data”. In: *Phys. Rev. C* 86 (1 July 2012), p. 015202. DOI: 10.1103/PhysRevC.86.015202.
- [79] Igor Strakovsky et al. “SAID Analysis of Meson Photoproduction : Determination of Neutron and Proton EM Couplings”. In: (Jan. 2014). arXiv: 1401.3027 [hep-ph].
- [80] P. Adlarson et al. “Measurement of  $\pi^0$  photoproduction on the proton at MAMI C”. In: *Physical Review C - Nuclear Physics* 92.2 (June 2015). arXiv: 1506.08849. DOI: 10.1103/PhysRevC.92.024617.
- [81] A. V. Anisovich et al. “Properties of baryon resonances from a multichannel partial wave analysis”. In: *European Physical Journal A* 48.2 (2012), pp. 1–13. arXiv: arXiv:1112.4937v1. DOI: 10.1140/epja/i2012-12015-8.

- [82] J. R M Annand et al. “T and F asymmetries in  $\pi^0$  photoproduction on the proton”. In: *Physical Review C - Nuclear Physics* 93.5 (2016), pp. 1–10. DOI: 10.1103/PhysRevC.93.055209.
- [83] M.H. Sikora et al. “Measurement of the  $^1\text{H}(\bar{\gamma}, \bar{p})\pi^0$  reaction using a novel nucleon spin polarimeter”. In: *Physical Review Letters* 112.2 (2014), p. 022501. arXiv: 1309.7897. DOI: 10.1103/PhysRevLett.112.022501.
- [84] D. Lohmann et al. “Linearly polarized photons at MAMI (Mainz)”. In: *Nuclear Inst. and Methods in Physics Research, A* 343.2-3 (1994), pp. 494–507. DOI: 10.1016/0168-9002(94)90230-5.
- [85] Kenneth Livingston. *Polarization from Coherent Bremsstrahlung Enhancement*. University of Glasgow. 2011.
- [86] V. F. Sears and S. A. Shelley. “Debye–Waller factor for elemental crystals”. In: *Acta Crystallographica Section A* 47.4 (July 1991), pp. 441–446. DOI: 10.1107/S0108767391002970.
- [87] Ken Livingston. “The Stonehenge technique. A method for aligning coherent bremsstrahlung radiators”. In: *Nuclear Instruments and Methods in Physics Research, Section A: Accelerators, Spectrometers, Detectors and Associated Equipment* 603.3 (2009), pp. 205–213. DOI: 10.1016/j.nima.2009.02.010.
- [88] D P Watts. *The Crystal Ball programme at MAMI*.
- [89] Cristina Collicott. “Probing Proton Structure through Single Polarisation Observables of Compton Scattering and  $\pi^0$  Photoproduction within the  $\Delta$  (1232) region.” PhD thesis. Apr. 2015.
- [90] R. Beck et al. *Proposal for an Experiment: Measurement of the G asymmetry in  $\gamma p \rightarrow p\pi^0$  and  $\gamma p \rightarrow n\pi^+$* . Mainz Microtron MAMI.
- [91] A. Thomas et al. “The new frozen spin target at MAMI”. English. In: *Physics of Particles and Nuclei* 44.6 (2013), pp. 964–967. DOI: 10.1134/S1063779613060221.
- [92] E. F McNicoll et al. “Experimental study of the  $\gamma p \rightarrow \eta p$  reaction with the Crystal Ball detector at the Mainz Microtron (MAMI-C)”. In: *Phys. Rev. C* 82 (3 Sept. 2010), p. 035208. DOI: 10.1103/PhysRevC.82.035208.

- [93] A. Thomas. “Physics at MAMI”. English. In: *NSTAR 2007*. Ed. by Hans-Werner Hammer et al. Springer Berlin Heidelberg, 2008, pp. 99–103. DOI: 10.1007/978-3-540-85144-8\_18.
- [94] A. Thomas. “Polarised targets for  $4\pi$  detectors at MAMI”. English. In: *The European Physical Journal Special Topics* 198.1 (2011), pp. 171–180. DOI: 10.1140/epjst/e2011-01489-8.
- [95] A. Thomas. *Numbers of Nucleons and Nuclei in Butanol Target*. Tech. rep. A2 MAMI, 2010.
- [96] D.I. Glazier. “A Geant4 simulation for the CrystalBall@MAMI Setup”. In: (2012). URL: <http://www2.ph.ed.ac.uk/nuclear/G4/G4A2CBSimulation-06-12.pdf>.
- [97] S. Agostinelli et al. “GEANT4 - A simulation toolkit”. In: *Nuclear Instruments and Methods in Physics Research, Section A: Accelerators, Spectrometers, Detectors and Associated Equipment* 506.3 (2003), pp. 250–303. arXiv: 1005.0727v1. DOI: 10.1016/S0168-9002(03)01368-8.
- [98] J. Allison et al. “Geant4 Developments and Applications”. In: *IEEE Transactions on Nuclear Science* 53.1 (2006), pp. 270–278. DOI: 10.1109/TNS.2006.869826.
- [99] J.R.M. Annand. *Data analysis within an AcquRoot Framework*. 2005. URL: <http://www.nuclear.gla.ac.uk/~acqusys/doc/AcquRoot.11.08.pdf>.
- [100] J C McGeorge et al. “Upgrade of the Glasgow photon tagging spectrometer for Mainz”. In: (2008). arXiv: arXiv:0711.3443v3. DOI: 10.1140/epja/i2007-10606-0.
- [101] Joseph Mancell. “A study of Eta Photoproduction on the Proton at MAMI”. PhD thesis. University of Glasgow, 2012.
- [102] Dominik Werthmuller. “Experimental study of nucleon resonance contributions to  $\eta$ -photoproduction on the neutron”. PhD thesis. University of Basel, Switzerland, 2014.

- [103] Thomas Jude. “Strangeness Photoproduction off the Proton at Threshold Energies”. PhD thesis. Feb. 2010.
- [104] Philippe Paul Martel. “Measuring Proton Spin Polarizabilities With Polarized Compton Scattering”. PhD thesis. Feb. 2013.
- [105] Farah Afzal. Personal communication. Sept. 2014.
- [106] Farah Afzal. Personal communication. Mar. 2015.
- [107] K. Livingston. *Polarization from Coherent Bremsstrahlung Enhancement*. 2011. URL: <http://nuclear.gla.ac.uk/~clasg8/CbremJlab/enhFitting.html>.
- [108] Ken Livingston. “Polarization from Coherent Bremsstrahlung Enhancement”. In: (2011). URL: <http://nuclear.gla.ac.uk/%7B~%7Dk1/mainz/cbrem/FittingCoherentBrem.pdf>.
- [109] Rene Brun and Fons Rademakers. “ROOT - An object oriented data analysis framework”. In: *Nuclear Instruments and Methods in Physics Research Section A: Accelerators, Spectrometers, Detectors and Associated Equipment* 389.1 (1997), pp. 81–86. DOI: [http://dx.doi.org/10.1016/S0168-9002\(97\)00048-X](http://dx.doi.org/10.1016/S0168-9002(97)00048-X).
- [110] Muriel Pivk. “sPlot: A Quick Introduction”. In: *arXiv* (Feb. 2006), p. 5. arXiv: 0602023 [physics]. DOI: 10.1142/9781860948985\_0036.
- [111] Luc Demortier and Louis Lyons. “Everything you always wanted to know about pulls”. In: *CDF Note* 5776 (2002), pp. 1–26. URL: [papers2://publication/uuid/2B2C6B40-711E-430A-8873-8212C493B763](https://publication/uuid/2B2C6B40-711E-430A-8873-8212C493B763).
- [112] Karsten Spieker. Personal communication. Mar. 2017.
- [113] S. Schumann et al. “Threshold  $\pi^0$  photoproduction on transverse polarised protons at MAMI”. In: *Physics Letters, Section B: Nuclear, Elementary Particle and High-Energy Physics* 750 (2015), pp. 252–258. DOI: 10.1016/j.physletb.2015.09.015.

- 
- [114] David L. Roper. “Evidence for a  $P_{11}$  Pion-Nucleon Resonance at 556 MeV”. In: *Physical Review Letters* 12.12 (1964), pp. 1962–1964. URL: <https://journals.aps.org/prl/abstract/10.1103/PhysRevLett.12.340>.
- [115] S. Eidelman et al. “Review of Particle Physics”. In: *Physics Letters B* 592 (2004), pp. 1+. URL: <http://pdg.lbl.gov>.
- [116] L. Alvarez-Ruso. “On the nature of the Roper resonance.” In: 14 (2010), pp. 1–8. URL: <https://arxiv.org/abs/1011.0609>. arXiv: arXiv:1011.0609v1.